©2014

Kimberly Yuri Scott

ALL RIGHTS RESERVED

THE UTILIZATION OF MENISCUS BRUSH PLATING ELECTRODEPOSITION FOR THE FABRICATION OF FREESTANDING HETEROGENEOUS COPPER-TIN FILMS FOR LITHIUM ALLOYING NEGATIVE ELECTRODES IN LITHIUM ION BATTERIES

by

KIMBERLY YURI SCOTT

A Dissertation submitted to the

Graduate School-New Brunswick

Rutgers, The State University of New Jersey

In partial fulfillment of the requirements

For the degree of

Doctor of Philosophy

Graduate Program in Materials Science and Engineering

Written under the direction of

Glenn G. Amatucci

And approved by

_____

_____

_____

_____

New Brunswick, New Jersey

October 2014

ABSTRACT OF THE DISSERTATION

The Utilization Of Meniscus Brush Plating Electrodeposition For The Fabrication Of Freestanding Heterogeneous Copper-Tin Films For Lithium Ion Batteries

By KIMBERLY YURI SCOTT

Dissertation Director:

Glenn G. Amatucci

Lithium-ion batteries are valuable energy storage devices that are presently utilized in most high-tech portable electronic devices and have the potential to be incorporated into large-scale storage for the grid with joint use of renewable energy sources and/or for wider use of electric vehicles. Current chosen commercial electrode materials have restricted the further advancement of these batteries due to their low achieved theoretical capacities. Lithium alloys have been highly researched as potential replacement negative electrodes for graphite due to their superior volumetric and areal high capacities, which would greatly expand the application options for these batteries. Intrinsic properties of these materials unfortunately have presented barriers to use due to extreme volumetric expansion and continual summation of irreversible loss during cycling, causing poor capacity retention after initial lithiation.

The research of this thesis focuses on the manipulation of the lithium alloying material, tin, by the choice fabrication process, electrodeposition and incorporation of supporting inactive material, copper. Processing plays a very important role in the morphology of a material. Therefore the advantageous properties of electrodeposition such as control of particle size and surface morphology, plethora of solution options, and ease of procedure make this technique a prime candidate to address the impeding issues of lithium alloys. Of particular interest, is a described first of its kind mechanical pulse deposition setup with meniscus flow during brush plating to create freestanding electrode films.

Copper-tin intermetallic phases are detailed in this project due to several previous findings' promising results of improvements in capacity retention and lower irreversible losses. Optimal diffusion for the electrodeposited films is examined through heat treatment studies with variations in film thickness and architectural film designs. Through these investigations, composite lithium alloying negative electrodes have been fabricated with both early competitive volumetric and areal capacities and low irreversible loss in comparison to today's leading electrode.

ACKNOWLEDGEMENT

I would like to take this time to thank my thesis advisor, Dr. Glenn G. Amatucci, who has provided the opportunity to explore and expand upon my interest in renewable energy research for the past 7.5 years, through the early stages of undergraduate research to my extensive graduate thesis project. I appreciate his patience and understanding through my time of balancing school, research and my duties as a division one athlete. Also, for his unwavering belief in my potential even when I, myself, was overwhelmed by the challenges of grad school. He has devoted countless hours to each of his students and has made every effort to always be available to each of us individually. The structure of our research group has prepared me well beyond other groups in our department for the next level of research in the workforce and for that experience, I welcome the next step in my journey.

I would also like to show my appreciation to my committee members: Prof. Lisa C. Klein (Graduate Director, Dept. Materials Science & Engineering), Prof. Eric L. Garfunkel (Co-Principal Investigator Nanotechnology for Clean Energy IGERT), and Prof. John T. Wenzel (Undergraduate Director, Dept. Materials Science & Engineering). They have each added different aspects to my graduate research experiences over the years. Collectively they have guided and shaped my educational experiences to culminate into the next level of researcher.

I would also like to acknowledge Prof. Manisha Chhowalla and Dr. Johanna Bernstein who provided the opportunity to participate and grow through the NSF Nanotechnology for Clean Energy IGERT Program. The experiences and activities I

have been afforded through this program have changed my outlook and perspective of renewable energy. It has intensified my passion and drive for providing early knowledge in all forms of renewable energy in hopes that nationally and globally we can change the awareness for the need of these energy sources. And the program has diversified my experience that I otherwise would not have had. Special thanks also to Dr. Bernstein, who has also provided valuable support and advice through my growing experience in graduate school.

I would like to acknowledge my financial support from DARPA N66001-10-C-2013 and National Science Foundation Grant No. 0903661 "Nanotechnology for Clean Energy IGERT." My graduate research and experiences would not have been possible without them.

I would like to also acknowledge the research staff and students of Energy Storage Research Group (ESRG) past and present, who have become family over the years. Dr. Nathalie Pereira has provided helpful advice and guidance through my growth as a doctorate level researcher. On countless times, she has taken time out of her busy schedule to assist with my research questions, papers, resumes, and presentations. Thank you to some of my former mentors during the early stages of my research as an undergrad when I was first introduced to energy storage: Prof Aurelien Du Pasquier; postdocs: Dr. Nader Hagh and Dr. Nicholas Hudak; graduate students: Dr. Prabeer Barpanda, Mr. Lawrence Weinstein, and Mr. James Kantor. A special thank you to former graduate students: Dr. Wei Tong, Dr. William Yourey, Dr. Andrew Gmitter, Dr. Matthew Parkinson; current staff members: Mr. Barry Vanning (who made my entire project and concept possible with his alterations to my plating

setup), Mr. John Gural, Ms. Fadwa Badway, Ms. Irene Plitz, Ms. Linda Sung, Ms. Anna Halajko; current graduate students: Mr. Jonathan Ko, Mr. Anthony Ferrer, Mr. Joshua Kim, Mr. Nicholas Faenza; undergraduate students: Greg, Sheel, Matt; and former students: Vera, Adam, Stacey, Mike R., Mike W. and Charlie. Each person has made my time working in ESRG memorable and worthwhile and having great co-workers has made doing research that much easier.

I would also like to recognize and thank my fellow trainees in the IGERT program: Dr. Tiffany Tong, Dr. Elizabeth Zeitler, Dr. Eric Gauthier, Dr. Zach Detweiler, Dr. Jesse Kohl, Dr. William McClain, Mr. Ryan Thorpe, Ms. Rut Rivera-Beltran, Mr. Chris Petoukhoff, Mr. Billy Mozet, Ms. Aleksandra Biedron, Mr. John Cannarella, Mr. Josh Spechler, Mr. Sahishnu Patel, Mr. Shoham Bhadra, Ms. Anna Hiszpanski, and Mr. Ben Agyei-Tuffour. As trainees, we have shared once in a lifetime experiences abroad in Africa, challenged and enhanced each other's perspectives on renewable energy, and grown into future leaders in our energy research specialties.

Finally I'd like to thank my brother and grandmother for their support over the years and my extensive field hockey family (especially Nigel, Melanie, Eryn, Michelle, Pattie, Brianna) who have been patient during this journey and provided outlets for stressful times and constant words of encouragement as I have worked towards my degree. My sanity has been tested on numerous occasions over the years but field hockey has always brought me back to level ground because of my teammates, coaches and life-long friends.

DEDICATION

I dedicate this thesis to my loving mother, Sandy, who is my teacher, my best friend, my rock. I am forever indebted to her for the many sacrifices she has made as a single mother to give my brother and I every possible opportunity for a full and meaningful life. Through the many hardships of raising us on her own and challenges life has thrown her, she has taught me to be grateful for every minute of life and to always follow my dreams no matter how big or small. Because of this amazing woman I am instilled with solid work ethics, never-ending determination, a passion and curiosity for science, and aspirations to leave a positive mark in this world. I hope I have made and continue to make her proud each and every day.

Table of Contents

ABSTRACT OF THE DISSERTATION ii

ACKNOWLEDGEMENT iv

DEDICATION vii

Table of Contents viii

List of Tables xi

Table of Figures xv

1 Introduction 1

1.1 General Energy Storage Device Background 1

1.2 Batteries: Primary & Secondary 6

1.3 LIB Components 12

1.4 Electrolyte 14

1.5 Positive Electrode 19

1.6 Negative Electrode 22

1.7 Lithium Alloys 25

1.7.1 General Description 25

1.7.2 History 26

1.7.3 Reaction Mechanism 27

1.7.4 Potential & Capacity Determination 27

1.7.5 Detrimental Issues For Lithium Alloys 30

1.7.6 Addressing Issues/ Improvements 32

1.7.7 Macro-scale Solutions 33

1.7.8 Micro-scale Solutions 40

1.7.9 Amorphous Research 41

1.7.10 Tin Research 42

1.7.11 History 44

1.8 Solid Electrolyte Interface (SEI) 55

1.9 Fabrication Process: Electrodeposition 62

1.10 Our Research 66

1.11 References 69

2 Experimental 71

2.1 Materials Fabrication 71

2.1.1 Brush Plating Setup 71

2.1.2 Plating Conditions For Copper & Tin Layers 74

2.1.3 Heat Treatment of Single Bilayer Copper-Tin Films 75

2.1.4 Triple Stacked Bilayer Copper-Tin Film Heat Treatment 75

2.1.5 Post Anneal Surface Coatings: LiPON & Alumina 75

2.2 Physical Characterization 77

2.2.1 FTIR Analysis of Insulating Pad 77

2.2.2 Profilometer Analysis 77

2.2.3 XRD Analysis 78

2.2.4 DSC Analysis 80

2.2.5 Pycnometer Density Analysis 81

2.2.6 FESEM/Cross Ion Polished Analysis 81

2.3 Electrochemical Characterization 82

2.3.1 Standard Half Cells with Galvanostatic Protocols 82

2.3.2 Standard Full Cell vs LCO (3mA/g) 84

2.4 References 84

3 Results & Discussions 85

3.1 Brush Plating Deposition: Optimization 85

3.1.1 Optimization of Plating Parameters for Copper Films 86

3.1.2 Plating Optimization For Tin Films 90

3.1.3 Substrate Optimization 91

3.1.4 Insulating Pad Optimization 95

3.1.5 Pulse Plating Deposition 103

3.1.6 Multilayer Deposition 109

3.1.7 Mixed Plating Solutions For Codeposition 110

3.1.8 Conclusions 113

3.2 Heat Treatment Optimization 114

3.2.1 Conclusions 118

3.3 Single Cu-Sn Bilayer Thickness Optimization 119

3.3.1 Thin Bilayer Copper-Tin Films: 5.68micron Tin Layer 119

3.3.2 Thick Bilayer Copper-Tin Films: 17μm & 8μm Tin Layers 122

3.3.3 Conclusions *128*
3.4 Triple Stack Thin Copper-Tin Films 129
3.4.1 Structure Analysis of Triple Stacked Bilayer Films *129*
3.4.2 225°C 4h Thermal Anneal of Triple Stacked Bilayer Film *129*
3.4.3 Cross Section Analysis *135*
3.4.4 Electrochemical Investigations For Triple Stacked Bilayer Films *137*
3.4.5 Conclusions *143*
3.5 Surface Coatings For Electrochemical Enhancement 143
3.5.1 ALD coatings *143*
3.5.2 LiPON coatings *145*
3.5.3 Conclusions *147*
3.6 Electrochemical Modifications with Electrolyte Additives 148
3.6.1 FEC & VC Additives *148*
3.6.2 EMC Electrolyte Modification *151*
3.6.3 Conclusions *153*
3.7 Overall Electrochemical Analysis of Cu-Sn Films 154
3.7.1 Lithium Uptake & Capacity Analysis For Cu-Sn Films *154*
3.7.2 Cycling Rates *157*
3.7.3 Cu-Sn Films Incorporated Into Li-Ion Cells *160*
3.7.4 Conclusions *162*
3.7.5 References *162*

4 Future Work 164
4.1 Hardware Alterations For the Meniscus Plating System 164
4.2 Ternary System: Cu-Sn-Sb 165
4.3 Additional Surface Coatings via ALD 168
4.4 References 170

5 Summary 171

6 Publication Acknowledgement 173

List of Tables

Table 1-1 Description of primary batteries and their typical applications..... 8

Table 1-2 Identification of some common rechargeable batteries' properties and their applications.....12

Table 1-3 Conductivity values for different types of electrolytes under ambient conditions.. .16

Table 1-4 Common lithium conducting molten salts with their operating temperatures 17

Table 1-5 Typical solid electrolytes for lithium ion cells 17

Table 1-6 Electrolyte organic solvents and salts commonly used in lithium ion cells 18

Table 1-7 Comparison of the electrochemical properties of common positive electrode materials for lithium ion batteries 21

Table 1-8 Comparison of the theoretical capacity potentials for various lithium alloying materials and current commercial negative electrode graphite. *Some values have been adapted from Zhang [28].....26

Table 1-9 Theoretical capacities for the oxide phases of tin. The SnO phase has a lower irreversible loss due to the single O atom compared to the dioxide phase 47

Table 1-10 Comparison of some researched lithium-tin alloying compositions.....55

Table 1-11 Typical SEI components found for lithium ion batteries listed with their most common electrolyte sources. Adapted from Verma et al & Agubra et al. [51,52]. 56

Table 2-1 Described plating conditions and film thicknesses for fabricated electrodeposited copper-tin films. 74

Table 2-2 Heat treatment protocols for copper-tin bilayer films. 75

Table 2-3 Electrochemically tested electrolyte combinations for the Cu-Sn half-cells 83

Table 2-4 Cycling protocols utilized for the Cu-Sn film half-cells. 83

Table 2-5 Protocol modifications used for further electrochemical analysis for the Cu-Sn film half-cells 84

Table 3-1. Technical guidelines for the electrodeposition of copper films. 86

Table 3-2 Optimized plating conditions for copper film deposition. 88

Table 3-3. Technical guidelines for the electrodeposition of tin films. 90

Table 3-4. Deposition conditions for good tin-plating deposition. 90

Table 3-5 Profilometer measurements of the average roughness affected by additional pretreatment. 93

Table 3-6 Comparison of insulating pad materials for electrodeposition optimization. 98

Table 3-7. Pulsed deposition trials including pulsed potential and pulsed current. 103

Table 3-8. XRD analysis for the pulsed films with varying anneal temperatures. 104

Table 3-9. Electrochemical analysis of pulsed deposition films. The difference of 1st lithiation and delithiation is described by the irreversible loss. 105

Table 3-10 Description of plating solution components..... 110

Table 3-11. XRD of a 225°C 4h annealed single bilayer 5.68μm Cu-Sn film. 120

Table 3-12 XRD analysis (top) for the annealed thick single bilayer Cu-Sn films (10micron:17micron)..... 123

Table 3-13 Electrochemical analysis of the thick single bilayer Cu-Sn (10micron:17micron) films showing the results for the first 1.5 cycles and the initial irreversible loss. The irreversible loss is defined as the difference between the first lithiation and delithiation. 124

Table 3-14 XRD analysis for the annealed thick single bilayer Cu-Sn (10micron:8micron) films. 126

Table 3-15 Electrochemical analysis for the first 1.5 cycles of the thick single bilayer Cu-Sn (10micron:8micron) films. The difference in the first lithiation/delithiation is defined as the irreversible loss.. 127

Table 3-16 X-ray penetration depth based on single direction for triple stacked films utilized with the 2V cycling cutoff. 134

Table 3-17 Single direction x-ray penetration depth analysis for triple stacked Cu-Sn films utilized with the 1.3V cutoff cycling.Table 3-17 Single direction x-ray penetration depth analysis for triple stacked Cu-Sn films utilized with the 1.3V cutoff cycling. 134

Table 3-18 Cycling protocols utilized for the electrochemical evaluation of the copper-tin deposited films. 137

Table 3-19 Electrochemical analysis of the first 1.5 cycles for the triple stacked Cu-Sn films cycled utilizing the 2V cutoff. Included is the comparison are the initial irreversible loss defined as first lithiation/delithiation difference 140

Table 3-20 Electrochemical results for the first 1.5 cycles of the triple stacked Cu-Sn films cycled with the 1.3V cycling cutoff. Irreversible loss is defined as difference in first lithiation/delithiation. 140

Table 3-21 Electrochemical comparison of the 20nm LiPON coated and standard triple stacked 7.5micron film 225°C 4h. The irreversible loss is the difference in 1st lithiation and delithiation. 147

Table 3-22 Electrochemical data for the initial 1.5 cycles including irreversible loss for the 10vol% and standard cycled Cu-Sn films. 150

Table 3-23 Electrochemical investigation of the first 1.5 cycles comparing the standard electrolyte 1M $LiPF_6$ EC:DMC to the 1M $LiPF_6$ EC:EMC cycling for the triple stacked Cu-Sn films. 153

Table 3-24 Investigated cycling rates for optimal electrochemical properties of the triple stacked Cu-Sn films 158

Table 3-25 Capacity retention for varying cycling rates for triple stacked Cu-Sn films 159

Table of Figures

Figure 1-1 Ragone plot comparing performance ability of available energy storage devices..... 2

Figure 1-2 Diagram of a flywheel energy storage device..... 3

Figure 1-3 Diagram of a typical supercapacitor charging and discharging..... 4

Figure 1-4 Diagram of a lithium ion battery showing electronic movement through an outside load and ionic conductivity through the internal insulating membrane..... 5

Figure 1-5 Diagram of the original electrochemical device, the Leclanché cell..... 6

Figure 1-6 Energy capabilities for common secondary (rechargeable) batteries. 9

Figure 1-7 Energy capabilities for common primary batteries. 9

Figure 1-8 Schematic representation of insertion and conversion reactions that occur in lithium ion batteries.. 14

Figure 1-9 Schematic of the layered structure for positive electrodes. Example is $LiCoO_2$. 19

Figure 1-10 Schematic of the cathode material olivine phosphate. a) $LiFePO_4$ b) $FePO_4$ 21

Figure 1-11 Graphite negative electrode. a) Prior to lithiation the stacking order for the graphite layers follows A-B-A-B-A order. b) After lithiation the layers become altered to A-A-A-A-A so that the lithium can sit as interstitials in the voids.....24

Figure 1-12 Determination of the alloy potentials based on its phase diagram and the Gibbs Phase Rule. a) Presence of 2 phases in composition makes intensive property (electrical potential) composition independent, plateau in potential seen. b) Presence of single phase makes the electrical potential dependent on the composition, variable potential across composition.....29

Figure 1-13 Schematic description of the lithiation process for the multiphase composite SnSb, which has an active matrix of Sn. Sn acts as the initial buffering matrix while Sb undergoes lithiation to form Li_3Sb. Further lithiation will result in the Li-Sn alloys, buffered by the no longer active Li_3Sb phase. 33

Figure 1-14 Characteristic potential curve for the lithiation of the SnSb multiphase composite. Lithium is first reactive with the Sb followed by the Sn within the composite. 34

Figure 1-15 Experimental data for Sn, Sb, and SnSb mixtures and alloys. a) Comparison of charge capacities for the pure metals, mixed Sn-Sb, produced SnSb, and annealed SnSb. b) Cycle efficiency for the alloyed SnSb. 35

Figure 1-16 Initial charge-discharge curves for Fe_2O_3. The large difference in the 1st cycle is due to the large irreversible losses that cannot be recovered with the reaction to form Li_2O.....37

Figure 1-17 Adapted from Zhang [28]. The addition of carbon and graphite to the Sb greatly improve the capacity retention of the alloy. 38

Figure 1-18 FESEM images for the porous structure data of Yoshio et al [38]. A) Image of the Ni foam current collector porous structure. B) Image of the Si electrode deposited on the foam structure. 39

Figure 1-19 Lithium-Tin phase diagram showing all the possible alloy phases. 43

Figure 1-20 Evaluation of the volume expansion associated with forming each of the lithium-tin alloys.....44

Figure 1-21 Titration curve for SnO showing the irreversible loss in conjunction with the formation of Li_2O the inactive matrix that improves cycle stability for Sn 45

Figure 1-22 Titration curve for SnO_2 showing the irreversible loss for the initial reaction to form Li_2O. 46

Figure 1-23 Comparison of TCO and SnO cycling efficiency. The TCO with the added glassy network formers B-P-Al show improved cycle ability. 47

Figure 1-24 Comparison of the initial cycling curves for graphite, TCO, Sn_2Fe, and $SnFe_3C$. The SnFe3C had decreased irreversible loss. 48

Figure 1-25 The phase diagram for the Cu-Sn system. Most lithium alloy research focuses on the η-phase (Cu_6Sn_5). 50

Figure 1-26 Comparison of cycling capacities for pure Sn, Cu_6Sn_6, Cu_6Sn_5, Cu_6Sn_4 and Li_2CuSn. The additional Cu in Cu_6Sn_6 provided additional support for better capacity retention. The Li_2CuSn phase had the worse cycling because it did not have the additional Cu typically formed from the initial lithiation of Cu-Sn alloy phase 51

Figure 1-27 Normalized capacities for Cu-Sn alloys and pure tin. 52

Figure 1-28 Schematic depiction of electrode-electrolyte interaction for lithium alloys. A) An initial reaction of the electrolyte with the negative electrode causes the formation of the SEI layer. B) Volume changes during lithiation cause fracturing. C) Fracture in SEI and Electrode expose new surfaces to electrolyte. D) Further reaction forms new SEI on electrode new surface. 58

Figure 1-29 Comparison of cycling capacity retention for silicon lithium alloy negative electrode with focus on the effects of VC additives to electrolyte. 60

Figure 1-30 Cycling analysis for VC and FEC additives with a TiSnSb electrode. a) Comparison of capacity retention shows the improve capabilities with the additives. b) Comparison of the accumulated irreversible losses shows a delayed increase for the cells with VC and FEC mixtures. 61

Figure 1-31 Electrodeposition bath setup composed of metal ions & current supplied to electrodes through an external power source.....62

Figure 2-1 Traversing arm brush plating system setup with stage for working electrode attachment and counter electrode.....71

Figure 2-2 Schematic of the directional movement during brush plating electrodeposition. The titanium working electrode moves back and forth in the 'x' direction while the platinum clad counter electrode simultaneously moves in the 'y' direction. 72

Figure 2-3 Schematic of the solution meniscus formation with flow through the teflon counter electrode holder from the solution reservoir via a peristaltic pump.. 73

Figure 2-4 Schematic representation of Bragg's Law.....79

Figure 3-1 Schematic of location mapping for thickness measurements of a 10micron copper film. The highlighted middle region shows the area of importance.....87

Figure 3-2 Schematic of the film thickness measurements associated with each location of the 10micron copper film. The middle highlighted section confirms the achieved targeted thickness. 87

Figure 3-3 Examples of deposition burning for a copper film. a) The arrows highlight burning of the film in both directions during plating. b) The arrows highlight burning of the film on both end areas of the film signifying the oscillation pauses too long in change of direction.....88

Figure 3-4 Example of a well-plated copper film under the correct deposition parameters.....89

Figure 3-5 Example of a well-plated tin deposition from the utilized conditions.....91

Figure 3-6 Phase diagram for titanium-copper. 92

Figure 3-7 Surface polish and abrasion pretreatment description for metal substrate. a) Surface polishing with sandpaper (grit 180) directionally applied to titanium plate. b) Scouring pad (Scotch Brite) roughened surface of substrate in circular motion to increase variations in surface morphology for better adhesion. c) Scouring pad applied directionally (counter electrode movement direction) to slightly decrease the adhesion properties to increase liftoff capabilities. 94

Figure 3-8 Observed inhomogeneous deposition of copper film due to low roughness in surface morphology of titanium substrate. Pretreatment of surface included only parallel directional roughening. 95

Figure 3-9 Insulating pad material holder design. a) Teflon ring-set designed to hold pad material taut in counter electrode holder. b) Teflon counter electrode holder has cavity to secure ring-set during deposition. c) Example of assembled pad holder with counter electrode holder (cotton batting & sleeving). 96

Figure 3-10 Observations for Cotton Batting and Sleeving. a) The arrows highlight the edges of the film, which show residual current density causing deposition outside of the desired area. b) The profilometer scan shows the overall roughness (Average roughness 487nm) of the film being uniform besides the isolated areas. 99

Figure 3-11 Deposition analysis for towel material. a) The arrows highlight the residual areas of deposition caused by the undesirable expanded area of applied current density. b) The profilometer 3D scan shows the roughness (827nm average) of the deposited film. 100

Figure 3-12 Observation for the cloth material. a) The arrows and circled area highlight the burning and discoloration that occurs during plating. b) The 3D profilometer scan shows that the surface morphology contains large variations in roughness (1.24μm average). 101

Figure 3-13 Observations for the white tuff wrap material. a) The white tuff wrap had a relatively controlled current density during deposition maintaining deposition in desired area. b) The overall roughness (548nm average) was homogenous throughout the film surface as seen in the 3D profilometer scan. 102

Figure 3-14 Areal lithiation capacity comparisons for pulsed deposited films. ●: pulsed 0.1A for 0.1sec film; ◆: pulsed 5V for 5sec film; ★: pulsed 5V for 0.1sec film. 106

Figure 3-15 Electrochemical comparison of pulsed and constant deposition films (10microns:8microns). ■: deposition by constant applied current; ◆: deposition by pulsed 5V for 5sec; ◀: deposition by pulsed 0.1A for 0.1sec; ●: deposition by pulsed 5V for 0.1sec. 108

Figure 3-16 Observed electroless plating that occurs when introducing copper sulfate plating solution to surface of tin film. a) Tin film plated on top of existing initial copper layer. b) Areas of contact for the copper solution with the tin film caused discolored copper film to form without any applied potential/current (electroless plating). c) Higher magnification (20x) shows that copper layer does not form a strong bond with surface film as desired from electrodeposition. 109

Figure 3-17 Visual observations of mixing copper and tin solutions over a 10-day span. 112

Figure 3-18 Profilometer 3D scans of surface topography. a) The surface of the non-annealed Cu-Sn film appears to be uniform and smooth (average roughnes: 487nm). b) The film annealed at 275°C 4h has formed a "hills and valley" topography (average roughness: 7.76μm). 114

Figure 3-19 FESEM EDS analysis of the Cu-Sn 275°C 4h film. The raised areas were dominant in tin (red) content while the 'valleys' had a higher copper (blue) content. 115

Figure 3-20 FESEM EDS spectrum analysis for the 'hills and valleys' of the 275°C 4h Cu-Sn film. a) Spectrum shows dominance in copper for the valley area of the film. b) Spectrum identifies dominance in tin for the hill area of the Cu-Sn film. 116

Figure 3-21 DSC analysis of the Cu-Sn film. The identified endothermic peak of the spectrum confirms the melting of the tin at approximately 226°C. 117

Figure 3-22 Freestanding electrodeposited Cu-Sn film; a) Bottom of film showing copper layer; b) Top view showing tin layer; c) Curled film shows freestanding capabilities. 119

Figure 3-23 XRD top surface analysis for the 1.33:1 molar ratio film with phases identified as: Cu_6Sn_5 (*), Cu_6Sn_5' (^), $Cu_{3.02}Sn_{0.98}$ ($), CuSn (%), Sn (>). 120

Figure 3-24 Voltage vs. time for the initial 1.5 cycles of the single bilayer 5.68micron Cu-Sn film. 122

Figure 3-25 Electrochemical analysis of the annealed 275°C 4h thick bilayer (1:1.22 molar ratio) film showing the poor lithiated (◆) volumetric capacity retention over 50 cycles despite low initial irreversible loss 125

Figure 3-26 FESEM & EDS analysis of non-annealed thick single bilayer film (10micron: 8micron) a.) Secondary electron image of tin plated on plated copper film; b.) EDS elemental mapping of two different metal films; c.) Wide field EDS spectra for identified metal films. 127

Figure 3-27 FESEM (a) and EDS (b and c) of 225°C 8h single bilayer film (10micron:8micron). 128

Figure 3-28 Comparison of the XRD phase for the triple stacked bilayer Cu-Sn films annealed at 225°C 4h as a function of Sn content (top surface analysis) 130

Figure 3-29 Comparison of phases as determined by XRD for the triple stacked bilayer Cu-Sn films annealed at 225°C 4h cycled with 1.3V cutoff (top surface analysis). **131**

Figure 3-30 The phases of the 6.5µm triple stacked film (top and bottom surface analysis) identified as: Cu_6Sn_5 (*), Cu_6Sn_5' (^), $Cu_{3.02}Sn_{0.98}$ ($), Cu_3Sn (+), CuSn (%), Sn (>), SnO (~), Cu (#). **132**

Figure 3-31 XRD phase analysis for the triple stacked Cu-Sn films (bottom surface analysis). **133**

Figure 3-32 FESEM & EDS images and spectrum for the triple stacked 7.5µm bilayer film (1:1.04 molarity). a.) Secondary electron image detailing cross-sectional view of stacked film; b.) EDS of copper content; c.) EDS of tin content; d.) Spectra results for 7.5µm triple stacked bilayer film. **135**

Figure 3-33 FESEM & EDS images and spectrum for the triple stacked 5.68µm bilayer film (1.33:1 molarity). a.) Secondary electron image detailing cross-sectional view of stacked film; b.) EDS of copper content; c.) EDS of tin content; d.) Spectra results for 5.68µm triple stacked bilayer film. **136**

Figure 3-34 FESEM & EDS images and spectrum for the triple stacked 6.5µm bilayer film (1.17:1 molarity). a.) Secondary electron image detailing cross-sectional view of stacked film; b.) EDS of copper content; c.) EDS of tin content; d.) Spectra results for 6.5µm triple stacked bilayer film. **136**

Figure 3-35 Electrochemical analysis of triple stacked bilayer films for the first 50 cycles utilizing 2V cutoff cycling. ■ -(1.33:1) molar ratio; ◆ - (1.17:1) molar ratio; ▼- (1:1.04) molar ratio.. ..... **138**

Figure 3-36 Electrochemical analysis of triple stacked bilayer films first 50 cycles utilizing 1.3V cycling cutoff. ★ – (1.33:1) molar ratio; ● - (1.17:1) molar ratio; ◀ - (1:1.04) molar ratio. 139

Figure 3-37 Voltage vs. time profiles for the first 5 cycles of the 1:1.04 molar ratio (7.5µm) stacked film with 1.3V cutoff. 141

Figure 3-38 Charge-discharge efficiencies for the 7.5µm (1:1.04 molarity) triple stacked film depicted by the comparison of lithiation and delithiation capacities for the 1.3V cycling cutoff. 142

Figure 3-39 Areal lithiated capacities comparison for films with ALD alumina surface coatings. ■: standard triple stacked 7.5micron film; ◀: 7.5micron triple stacked film with 5nm ALD coating; ▼: 7.5micron triple stacked film with 15nm ALD coating. 144

Figure 3-40 Electrochemical comparison of the LiPON coated triple stacked 7.5micron films with a standrad 7.5micron triple stacked film. ⬢: 20nm LiPON coated triple stacked 7.5micron film; ★: standard triple stacked 7.5micron film; ▶: 250nm LiPON coated triple stacked 7.5micron film.. 146

Figure 3-41 Electrochemical analysis of the areal lithiated capacities for FEC additives (5vol% & 10vol%). ◆: standard 1M $LiPF_6$ EC:DMC (50vol%:50vol%); ◀: 5vol% FEC additive; ▶: 10vol% FEC additive. 149

Figure 3-42 Electrochemical analysis of the VC additives 5vol% and 10vol% compared to the standard LiPF6 ED:DMC electrolyte. ★: standard cycling with 1M $LiPF_6$ EC:DMC; ●: 10vol% VC additive; ▶: 5vol% VC additive. 150

Figure 3-43 Electrochemical analysis of the lithiated areal capacities for the standard electrolyte $LiPF_6$ EC:DMC and modified electrolyte $LiPF_6$ EC:EMC. ■: standard 1M $LiPF_6$ EC:DMC (50vol%:50vol%); ▼: modified 1M $LiPF_6$ EC:EMC (30vol%:70vol%). 152

Figure 3-44 Volumetric capacities for the triple stacked Cu-Sn film cycled with a potentiostatic hold. ■: lithiated capacity (mAh/g); ■: delithiated capacity (mAh/g)..... 154

Figure 3-45 Comparison of the lithiated and delithiated surface area capacities (mAh/cm^2) to observe cycle retention with a fixed capacity cutoff. —: lithated capacities; —: delithiated capacities 156

Figure 3-46 The electrochemical comparison of cycling speeds for triple stacked 7.5µm Cu-Sn films annealed 225°C 5h. ●: cycled protocol 3; ◆: cycled protocol 1; ⬟: cycled protocol 2. 158

Figure 3-47 Electrochemical analysis for the first 20 cycles of the triple stacked 6.5µm (1.17:1 molarity) films in Li-ion cells. ■:D627; ◆:D632..... 161

Figure 4-1 Counter electrode geometry proposition. a) The current geometry of the electrode creates areas not uniformly deposited due to mismatch in overlap. b) The rectangular configuration covers the entire width of the film, eliminating the one directional mismatch overlap. 165

Figure 4-2 Binary phase diagrams for Cu-Sn (a) Cu-Sb (b) and Sb-Sn (c)..... 167

Figure 4-3 Cycling stability for ZrO_2 coated $Li_4Ti_5O_{12}$ electrodes. LTO-50 represents the thickest ZrO_2 coating and LTO-0 represents the thinnest coating. 168

Figure 4-4 Electrochemical cycling stability comparison of TiO_2 ALD coatings with graphite electrodes. The 400 ALD reaction cycle film had a thickness of approximately 40nm. The 200 ALD reaction cycle film had a thickness about half that amount. 169

1 Introduction

1.1 General Energy Storage Device Background

Advancement is defined as the progression or development to further improve upon the capabilities of something. The availability of electricity and the way it is used has undergone a vast amount of advancements from its original commercialization back in the 1800s. In the early stages of development, electronics were constricted to plug-in for access to electricity. However with time, the idea of portable electricity brought the development of energy storage devices. Energy storage devices are defined as systems that have the unique ability to store energy in the form of chemical, mechanical, or thermal energies until needed and converted into its final state for use [1]. In today's society, portable electronics such as laptops, cell phones, and digital cameras have been accepted as part of everyday life that most people cannot fathom living without. Moving forward with further advancements, energy storage devices are being looked at as a possible solution for power grid storage and large-scale storage for affordable consumer automobiles. With the vastly growing population worldwide, the energy demand is increasingly reaching overwhelming levels. Proposed solutions for this problem include the addition of renewable energy sources to the established power grid network. However, unlike conventional energy sources, renewables only have the ability to produce energy intermittently. Energy storage devices' unique properties will allow for the effective inclusion of renewable energy sources into the power grid [2,3].

Overall, whether it be on the small or large scale, energy storage devices and technology advancements have become intertwined from the past, present, and leading into the future with no unraveling in sight.

The three main classifications of energy storage systems, with varying properties, that make each appropriate for different applications include: flywheels, capacitors, and batteries. Each of these systems have vastly different energy

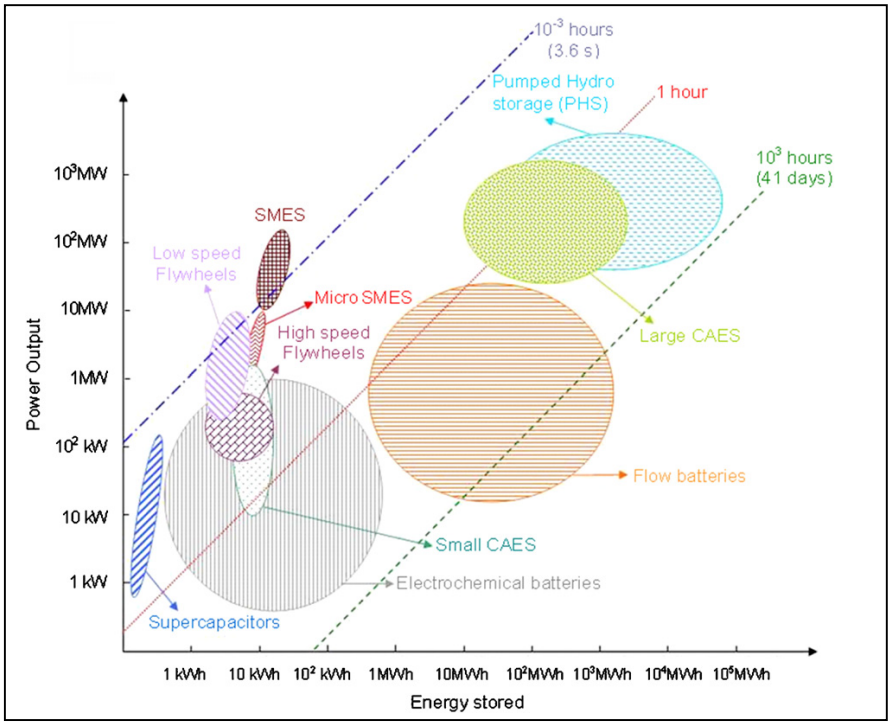

Figure 1-1 Ragone plot comparing performance ability of available energy storage devices.

capabilities which have been compared by Moura et al through a Ragone plot as adapted in Figure 1-1 [4,7]. Ragone plots are graphical interpretations of energy storage devices, which compare their power and energy densities. They are typically utilized to determine cost analysis for applications by comparing performance capabilities in terms of the ratio of mass to energy and power [5,6,7]. In Figure 1-1, the shaded region for each energy storage device is representative of the optimal

power-energy curve with the addition of estimated time slopes to achieve these values. From this plot, it can be concluded that most energy storage systems do not cover both high power density and high energy density for long periods of time.

The first of the energy storage systems to be discussed is flywheels, which have high power densities but for limited amounts of time. A flywheel has the ability to convert stored kinetic energy into electrical energy via a cylindrical rotating mass in conjunction with a motor/generator [1,8]. In the storage state, the motor through a central axis rod accelerates the mass. When the electrical energy is needed, the motor acts as a generator while the cylindrical mass decelerates. An example of a flywheel is seen in Figure 1-2 [9].

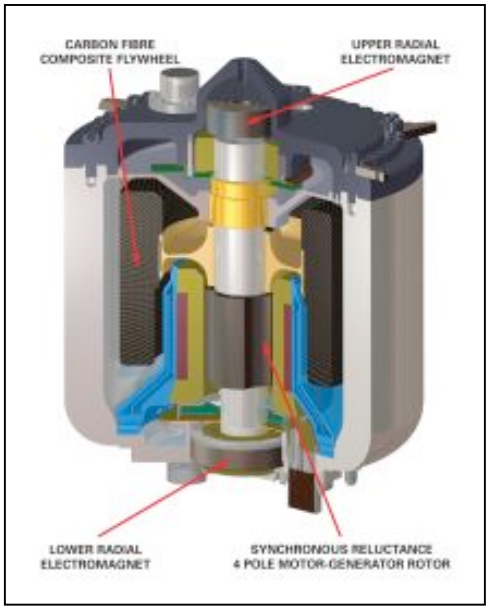

Figure 1-2 Diagram of a flywheel energy storage device

The other energy storage systems consist of transforming electrochemical energy into electrical energy. Capacitors, which are on the high power density but low energy density range, are great for applications that need large burst of energy for short periods of time. Also called supercapacitors or ultra-capacitors, these devices are designed from two parallel conductive porous plates separated by a very thin void filled with electrolyte and an insulating permeable layer [10,8]. Figure 1-3 shows a diagram depicting a typical electrochemical capacitor [11]. During the charging state of the supercapacitor, the two electrodes are connected to an external

power source and a voltage is applied. Due to separation by an electrolyte, the surfaces of the electrodes start to accumulate opposite charges and the electrolyte interface with each electrode forms a layer of opposing attractive charge to form a double layer [10,12]. Upon discharging, the charge build-up is neutralized by the current flow through a connected desired application. The main difference between electrochemical capacitors from the other two energy storage systems is their ability to store energy on the surface of the electrodes as a charge. Due to this inherent property, there are no major structural changes during charging and

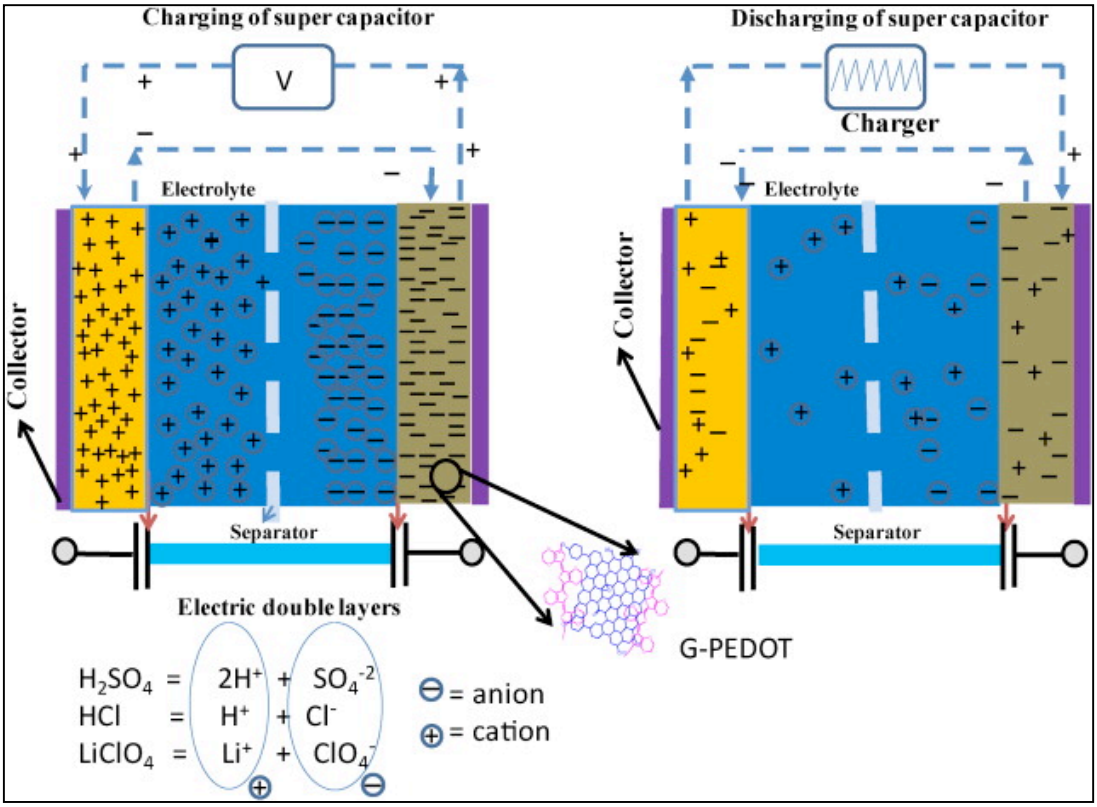

Figure 1-3 Diagram of a typical supercapacitor charging and discharging.

discharging, which allows the devices to have supreme lifetimes. However, this property is also the limiting reason behind capacitors ability to only store short bursts of energy.

The final energy storage devices, which convert electrochemical energy into electrical energy through structural changes, are batteries. Unlike capacitors, these devices have high energy densities but slow cycling rates. Batteries similarly contain two different electrodes separated by insulated permeable material saturated in an electrolyte. Upon completing the circuit through an external source, the electrodes undergo an electrochemical redox reaction. During the discharging phase, the negative electrode is oxidized and yields positive ions to the positive electrode through the electrolyte while electrons are given up through the external closed circuit. The positive electrode undergoes a reduction process as the electrons are consumed by meeting up with the excess ions [8]. The opposite reaction would then occur for the charging process.

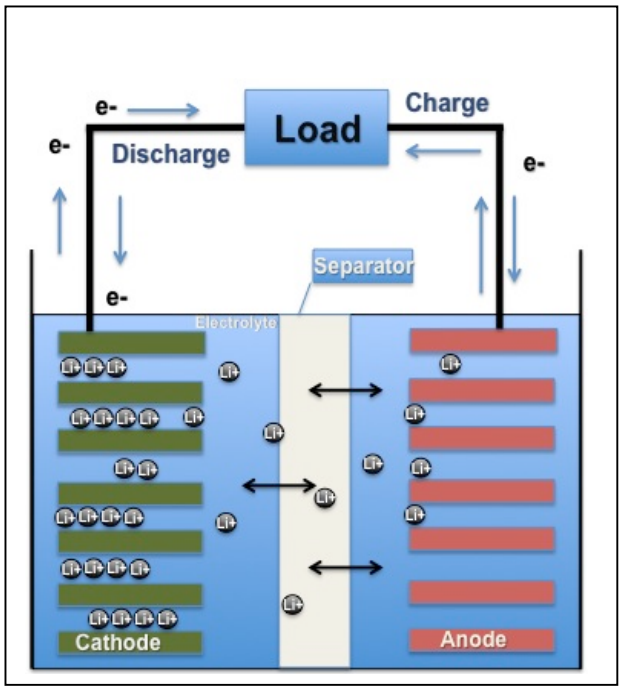

Figure 1-4 Diagram of a lithium ion battery showing electronic movement through an outside load and ionic conductivity through the internal insulating membrane.

Batteries typically contain liquid or solid electrolytes that are nonreactive and stable with the electrochemical potential range dictated by the electrodes so that proper exchange of ions may occur. Figure 1-4 depicts an example of a typical lithium ion battery. The most important thing to note for batteries in comparison to capacitors is the fact that their energy capabilities are from the electrode bulk

material [12]. This property is the ultimate reason why these devices have limitations to their charge and cycling rates, as well as increased energy densities in comparison to the other energy storage devices.

1.2 Batteries: Primary & Secondary

Batteries can be divided into two categories: primary and secondary. Primary batteries consist of all batteries that do not have the ability to reversibly overcome the structural changes that occur during the conversion of electrochemical energy to electrical energy and therefore are one time use only. The original design for the primary battery cell was the carbon-zinc Leclanché aqueous cell. In this design, the zinc negative electrode functions also as the containment for the cell itself. The carbon rod is centrally located in the cylindrical can and isolated from the outer containment by the top seal. The interior space surrounding the central rod contains a paste of carbon and manganese dioxide. The interface between the negative electrode and the paste is filled with an ammonium chloride electrolyte. Figure 1-5 gives a diagram of the simplistic cross section of the cell, which is further detailed by

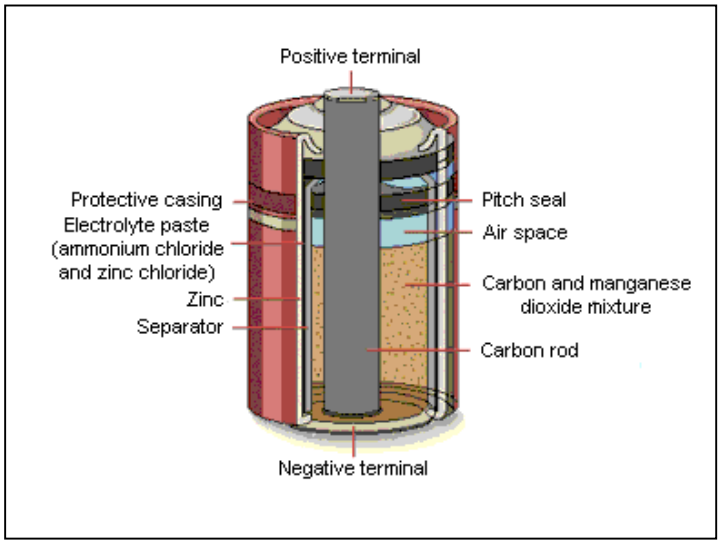

Figure 1-5 Diagram of the original electrochemical device, the Leclanché cell.

Dell [13,14]. Over the years, this design of the battery has evolved so to include higher capacity materials for the electrodes and better packaging design so that there is an increase in the active material procured. Table 1-1 details types of primary batteries including their common applications [13,15]. This table gives a general idea of the primary batteries utilized commercially, but it should be noted that several variations of these listed cells exist with fine-tuning to one of its electrodes or electrolyte. Figure 1-6 presents the typical performance capabilities of some of these devices [16].

Table 1-1 Description of primary batteries and their typical applications.

System	Negative Electrode	Positive Electrode	Electrolyte	Application
Carbon-Zinc	Zinc	Carbon	Ammonium/Zinc Chloride Zinc Chloride	Small Electronics
Alkaline Manganese	Zinc	Manganese Dioxide	Potassium Hydroxide	Electric Shavers, Cassette Players, Smoke Detectors
Zinc-Air	Zinc	Air	Potassium Hydroxide	Hearing Aids
Lithium	Lithium Foil	Iodine poly-2-vinyl pyridine complex	Lithium iodide	Heart Pacemakers, Watches, Pocket calculators
		Thionyl Chloride	Thionyl Chloride Lithium Tetrachloroaluminate complex	Naval sonar buoys, Space power
		Polycarbon Monofluoride	Lithium tetrafluoroborate in γ-butyrolactone	Memory
	Li/Al Alloy	Iron Sulfide	Lithium Halide	Rocket/Missile Power Source
	Lithium Foil	Silver Vanadium Oxide	Lithium Hexafluorophosphate in Propylene Carbonate/ Dimethoxyethane	Implantable cardiac defibrillator

The additional category of batteries that will be the main focus of this review is secondary batteries. This group of batteries has the inherent ability to reversibly convert electrochemical energy into electrical energy and vice versa through the simultaneous movement of ions and electrons along separate paths. Due to this capability, this group of energy devices is also known as rechargeable batteries. Although this group of batteries may not have the same high performance capabilities as their primary counterparts (Figure 1-7.), the additional characteristic of recharging ability, makes them prime candidates for high-tech applications [16]. Table 1-2 is a compilation of several major secondary battery

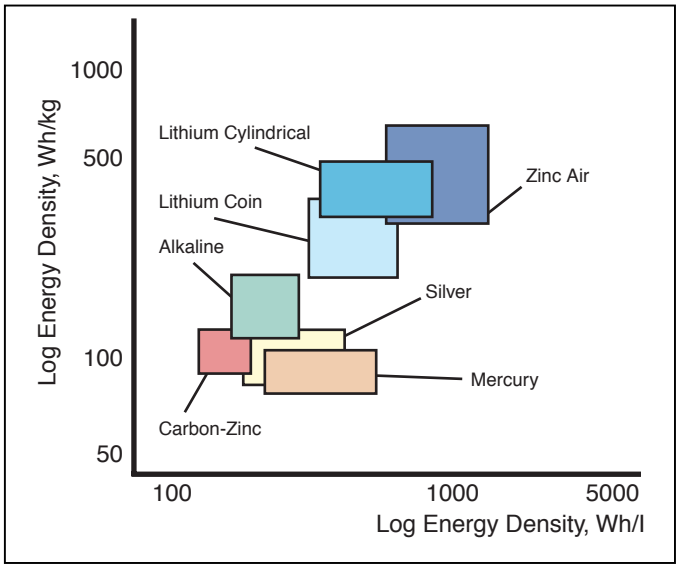

Figure 1-7 Energy capabilities for common primary batteries.

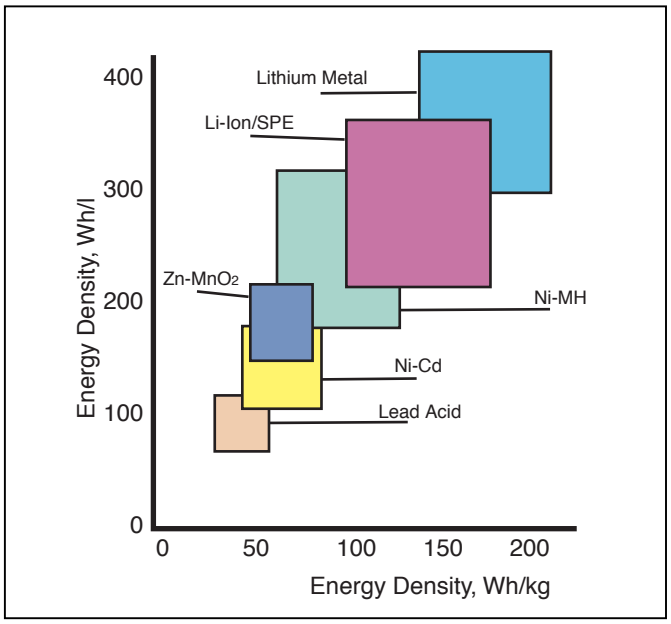

Figure 1-6 Energy capabilities for common secondary (rechargeable) batteries.

systems and their major applications [1,13,15,16]. Of the listed systems, the lead-acid battery is the oldest technology, dating back from 1859. Its well known properties and capabilities have brought about the use of lead-acid batteries throughout a wide range of storage requirements and its straightforward manufacturing needs have made this technology the most cost effective of the secondary batteries in initial cost ($/Wh) [1]. However, on the downside, these systems include toxic heavy metals and undergo detrimental self-discharge, as well as suffer from much lower energy densities in comparison to the other rechargeable battery systems. The nickel cadmium system shares some similarities to the lead-acid system, namely power density and aqueous electrolyte, but ultimately has a higher energy density and better life cycle. The nickel metal hydride systems have almost identical structural design to that of the nickel cadmium however have higher energy densities, making them a superior choice for small portable electronics. Some possible options for the metal hydride in this type of battery include: lanthanum-nickel based or titanium-zirconium based [13]. The sodium sulfur and sodium nickel chloride battery systems are separate from the rest of the rechargeable batteries in that they require high temperatures to function efficiently. Unlike the rest of the rechargeable batteries, these two systems utilize molten salts with liquid electrodes. Although these systems tend to have energy capabilities above lead-acid and nickel cadmium systems, the temperature requirements of these systems limit their uses and add more emphasis to safety factors. Lithium metal batteries have been investigated for secondary batteries, but safety issues present a barrier to further use in common applications. The final rechargeable

system of interest is the lithium ion battery, which utilizes the movement of lithium ions from electrode to electrode for its capacity capabilities and the use of non-aqueous electrolytes. Out of all the secondary batteries, lithium ion batteries have undergone the fastest development in present years and have the greatest potential for further optimization due to the short period of time in existence and plethora of electrode options still worth exploring. Although lithium ion batteries have the highest viable energy density capabilities, growth in many applications have been stunted because of their high manufacturing and materials costs in comparison to other technologies [1,2].

Table 1-2 Identification of some common rechargeable batteries' properties and their applications

System	Negative Electrode	Positive Electrode	Electrolyte	Application
Lead-Acid	Lead Alloy	Lead Oxide	Sulfuric Acid	Automobiles, Uninterruptible Power Sources
Nickel-Cadmium	Cadmium	Nickel Oxide	Potassium Hydroxide	Engines, Locomotives, Industrial Trucks
Nickel Metal Hydride	Metal Hydride	Nickel Oxide	Potassium Hydroxide	Terrestrial Applications
Sodium Sulfur	Liquid Sulfur	Liquid Sodium	Beta Alumina	Heavy Machinery, Space, Grid Storage
Sodium-Nickel Chloride (ZEBRA)	Nickel Chloride	Sodium	Beta Alumina	Electric Vehicles, Miltary
Lithium Ion	Carbon/ Graphite	Lithium Metal Oxide	Non-aqueous lithium ion conductor	Cameras, Cellphones, Computers

1.3 LIB Components

There are three main components to the lithium ion rechargeable cell that affect the overall capacity of the device: the electrolyte, positive electrode, and the negative electrode. As mentioned previously there is a wide range of materials for these components, which allow each specific combination to undergo an indicated reaction. In all, there are two main types of reactions that may occur for use of energy in the lithium ion cell: reconstitution and insertion reactions. The main

difference between these reactions is that in reconstitution reactions, the microstructure of one of the electrodes undergoes phase transformation to form a new phase. Two classifications include displacement and conversion reactions. In a displacement reaction, the products are formed through the extrusion of one phase while the addition of lithium creates a new phase as seen in Equation 1.1:

$$\mathbf{xLi^+ + xe^- + MN \leftrightarrows Li_xM + N} \qquad \mathbf{(1.1)}$$

In the above equation, as more of the phase Li_xM is formed through the displacement of the constituent, N, the additional phase N is formed. In a simple conversion reaction, the reactants of lithium ions with electrons and the electrode alter the microstructure to form a new phase. This is demonstrated in Equation 1.2:

$$\mathbf{yM + xLi^+ + xe^- \leftrightarrows Li_xM_y} \qquad \mathbf{(1.2)}$$

In this reaction process, upon the reactants combining within the cell, there will be the formation of the new phase Li_xM_y with its own unique properties and structure.

Switching gears to the other main type of reaction, insertion reactions undergo a different approach to energy conversion in that one of the main reactants can be inserted into the vacancies of the additional reactant. This reaction, also called an intercalation reaction, undergoes minimal changes to the actual structure of the host material, which sets it apart from the previously discussed reconstitution reactions. Equation 1.3 gives the general reaction:

$$\mathbf{MO_x + yLi^+ + ye^- \leftrightarrows Li_yMO_x} \qquad \mathbf{(1.3)}$$

where the structure of MO_x is maintained after insertion of the lithium. Figure 1-8 shows the schematic of both an intercalation and conversion reaction. Ultimately, electrodes undergoing the reconstitution reactions tend to have higher capacities due the ability to utilize charge transfer per molecular unit of a higher order than +1. This is not the case for intercalation reactions, which are confined to the 1:1 ratio of lithium ions to metal atoms due to the simple insertion of the ion into low energy voids within the crystal structure of the metal host [17,18]. Overall, the three different reaction mechanisms have led to the plethora of options for electrode materials leading into the variety of possible lithium ion batteries.

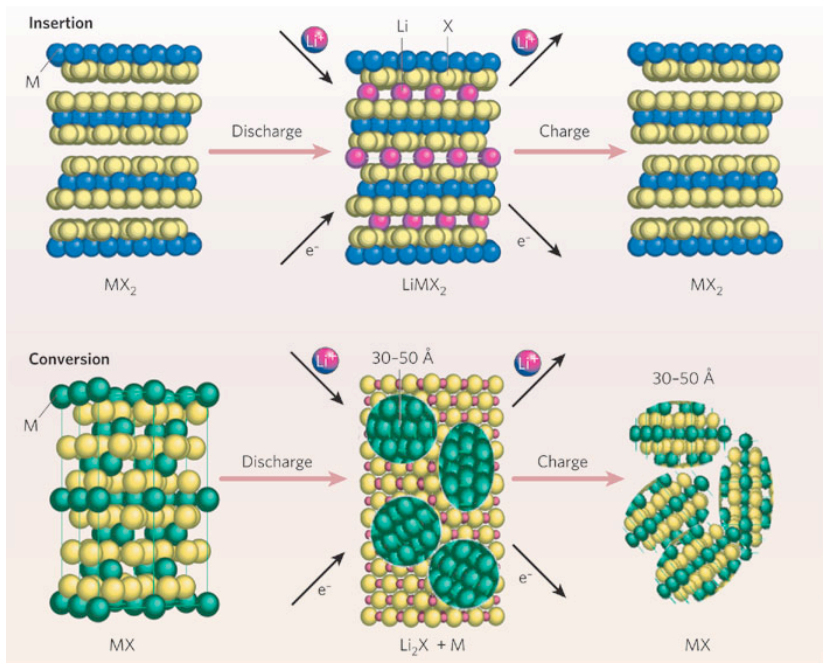

Figure 1-8 Schematic representation of insertion and conversion reactions that occur in lithium ion batteries.

1.4 Electrolyte

In order for the above reaction mechanisms to properly function, an intermediate transporter is required with the ability to selectively mobilize only

ions from one electrode to the other across the insulating barrier of the separator material. This intermediate transporter is also known as the electrolyte. An electrolyte is typically comprised of a solvent and dissolved salts, acids, or alkalis [20]. There are several important aspects that must be considered in choosing an appropriate electrolyte with two of the most important characteristics being conductivity and stability [19]. The electrolyte must be strictly an ionic conductor that prohibits the electrodes' electrons from passing through the internal electrochemical circuit of the lithium ion battery. Good electrolyte conductivity values for lithium ion batteries are described in Table 1-3 for the various types of electrolytes [20]. Of these specified electrolytes, the organic liquid electrolytes are the most commonly used for commercial purposes. For stability purposes, the electrolyte should be as nonreactive as possible (wide HOMO-LUMO range for electrochemical stability) to the electrode materials being as its sole purpose is simply to transfer ions rather than have a physical task in the chemical reaction within the cell. However, due to the electropositive properties of typical electrode materials versus the contrasting properties of the electrolyte components some intermediate reactions do tend to occur as described by Huggins [17]. Other important characteristics also include thermal and electrochemical stability in accordance to the lithium ion cell design. For most typical cells, liquid electrolytes are required to maintain their state through a temperature range of -40°C to 70°C while having thermal stability up to 85°C. There is also an emphasis on the electrolyte maintaining its properties through the working electrochemical window

for lithium of 0 to 5.0 V [21]. Other areas of consideration also include availability and cost.

Table 1-3 Conductivity values for different types of electrolytes under ambient conditions.

Electrolyte Type	Aqueous	Molten Salt	Inorganic	Organic	Polymer	Inorganic Solid
Specific Conductivity $\Omega^{-1}cm^{-1}$	$1\text{-}5 \times 10^{-1}$	$\sim 10^{-1}$	$10^{-3}\text{-}10^{-1}$	$10^{-3}\text{-}10^{-2}$	$10^{-7}\text{-}10^{-3}$	$10^{-9}\text{-}10^{-5}$

As briefly mentioned in Table 1-3, there are several different categories of electrolytes. Aqueous electrolytes are less commonly used for lithium ion cell purposes because of their smaller electrochemical stability window in comparison to other types of electrolytes. Huggins describes several molten salts that act as lithium ion conductors at elevated temperatures as seen in Table 1-4 [17]. Inorganic electrolytes for lithium ion batteries typically are composed of liquid SO_2-based $LiAlCl_4$ or $LiGaCl_4$ as described in detail by Reddy et al [22]. Polymer electrolytes are of the solid or gel phase and act as both the ionic conductor and separator for the system. Examples include the solid dry electrolyte: poly[ethylene oxide-co-2-(2-methoxyethoxy)ethyl glycidyl ether or the gel electrolyte: PVdF with the salts, $LiClO_4$ or LiTFSi as further described by Wakihara [19]. Solid electrolytes, although having lower conductivity values than their liquid counterparts are also used throughout the lithium ion cell technology. Table 1-5 lists some of the common solid electrolyte options that have been described by Owens [23].

Table 1-4 Common lithium conducting molten salts with their operating temperatures

Molten Salt	Operational Temperature	Type of Salt
LiCl-KCl	380°C	Inorganic
LiF-LiCl-LiI	334°C	Alkali Halide
LiF-LiCl-LiBr-LiI	325°C	Alkali Halide
LiF-LiBr-KBr	280°C	Alkali Halide
$LiAlCl_4$	135°C	Low Melting
$LiCl-NaCl-KCl-AlCl_3$	61°C	Low Melting
$LiCl-KCl-AlCl_3$	86°C	Low Melting

Table 1-5 Typical solid electrolytes for lithium ion cells

Electrolyte	$LiI(Al_2O_3)$	LiI	$Li_{0.36}Si_{0.365}O_{0.04}P_{0.01}S_{1.36}$	$Li_{1.26}I_{0.12}O_{0.31}P_{0.12}S_{0.098}$	$Li_{0.35}I_{0.12}O_{0.31}P_{0.12}S_{0.098}$	$Li_{0.39}N_{0.20}O_{0.47}P_{0.12}$
Log S $W^{-1}cm^{-1}$	-5	-7	-3.3	-4.7	-4.7	-5.6
Typical Cell System	Li/PbI_2	$Li/I_2(P_2VP)$	Li/TiS_2	$InLi_x/Li_{1-x}CoO_2$	Li/TiS_2	$Li/a\text{-}V_2O_5$ $Li/LiMn_2O_4$

The final grouping of electrolytes and probably the most commonly used are the organic liquid electrolytes. Organic electrolytes typically contain organic cations and carbonate anions. Some of the possible solvents and salts are described in Table 1-6 [17,21]. Due to the various different solvents and salts, there are several different possible combinations to compose of a working electrolyte. The standard electrolyte for commercial lithium ion batteries contains the combination of lithium hexafluorophosphate with ethylene carbonate and dimethyl carbonate.

Table 1-6 Electrolyte organic solvents and salts commonly used in lithium ion cells

Lithium Salts	Formula	Solvents	Formula
Lithium hexafluorophosphate	$LiPF_6$	Diethyl Carbonate	DEC
Lithium hexafluoroarsenate	$LiAsF_6$	Ethyl Methyl Carbonate	EMC
Lithium bis(trifluoromethylsulfonyl)imide	LiTFSI	Propylene Carbonate	PC
Lithium tris(trifluoromethylsulfonyl)methide	LiMe	Butyrolactone	GBL
Lithium bis[oxalate(borate)]	BOB	Acetonitrile	AN
		Ethylene Carbonate	EC
		Tetrahydrofuran	THF
		Dimethyl Carbonate	DMC

As mentioned previously, stability is a very important characteristic for the electrolyte. The organic solvent electrolytes ironically are highly reactive when they are in contact with electropositive metals at low potentials. At the interface of the electrolyte and negative electrode of the lithium ion battery, an irreversible chemical reaction will occur forming what is known as the solid electrolyte interphase or SEI. This SEI layer is composed of an electronically insulating amorphous reaction product that forms on the negative electrode surface while simultaneously generating an organic radical gas upon formation [17]. This self-limiting passivation barrier plays a vital role in prohibiting further chemical reactions at the interface as well as assuring only ionic conductivity through the electrolyte. This reaction typically takes place only during the initial cycles of the battery. However, new exposed interfaces will cause new SEI layer formation as will be discussed later on. The solid electrolyte interphase has both pros and cons to its existence. Advantageously, this layer makes it possible to utilize the most popular

choice group of electrolytes for lithium ion battery technology. It acts as a self-healing barrier to increase the stability range of the electrolyte. But as mentioned, this is an irreversible reaction with the surface material of the negative electrode that decreases the available energy capacity for use in the electrochemical reactions within the battery. Also of concern can sometimes be the thickness of the SEI layer. It is desirable that this layer be electronically insulating to cease electron activity but if the SEI layer is too thick issues will arise with the ionic activity and the battery can then become non functional. Overall, the solid electrolyte interphase is crucial to the livelihood of organic electrolytes in the present and future of lithium ion batteries.

1.5 Positive Electrode

Lithium ion batteries do not contain pure lithium metal in its electrode materials and therefore the initial source for lithium ions tends to be the responsibility of the positive electrode or cathode material. This material is pre-lithiated during the fabrication process before cell assembly. The most common reaction mechanism that occurs at the positive electrode within the cell is intercalation. There are three main groups of positive electrode materials that are commercially available for lithium ion

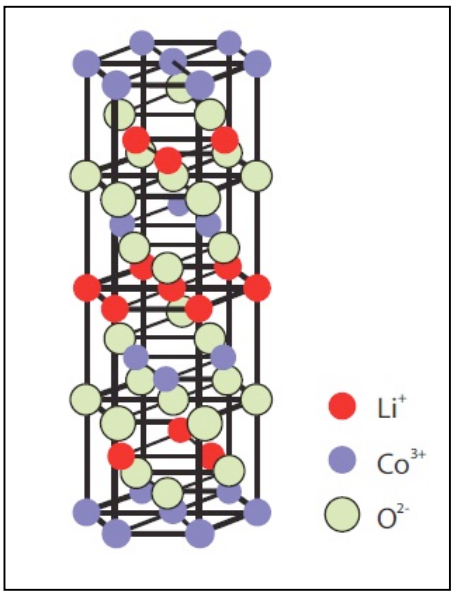

Figure 1-9 Schematic of the layered structure for positive electrodes. Example is $LiCoO_2$.

batteries. The first group of materials is known as having a layered close packed face centered cubic structure in which the lithium and metal ion layers alternate between the oxide ions. A model of this layered structure is seen in Figure 1-9 [24]. Typical positive electrodes of this structure are $LiCoO_2$, $LiNiO_2$, $LiVO_2$, $LiCrO_2$, and $LiNi_{1-x}Co_xO_2$ [19,25].

Another group of positive electrode materials has a more three-dimensional framework structure, also called spinels. In this structure design, the oxide ions also follow the close packed face centered cubic structure but the locations of the metal and lithium cations can be located in either octahedral or tetrahedral sites [27]. The generalized formula for the spinel structure is AB_2O_4 where the lithium cations are in 'A' and the metal cations are in 'B'. For most cases, the cations in position 'A' occupy ⅛ of the possible tetrahedral sites and the cations of 'B' occupy ½ of the octahedral sites. Some examples of spinels used for positive electrode materials include: $LiMn_2O_4$ and $LiM_yMn_{2-y}O_4$ (where M=Co, Cr, Al, Ni, Li) [19].

The final group of positive electrodes is the lithium transition metal phosphates. This group of materials has an olivine structure where a portion of the lithium atoms sit in the octahedral sites and ⅛ the metal atoms sit in the tetrahedral sites of the hexagonal closed packed array [26]. This group of materials can be viewed as an advantageous replacement for the lithium cobalt oxide electrodes due to their lower cost and safety [27]. The top examples of these positives electrode materials include $LiMnPO_4$ and $LiFePO_4$. Figure 1-10 provides a schematic of the structure for the olivine phosphate, $LiFePO_4$. Of the described cathode materials,

Table 1-7 gives a brief comparison of the electrochemical properties of some of the major cathode materials in current use [25].

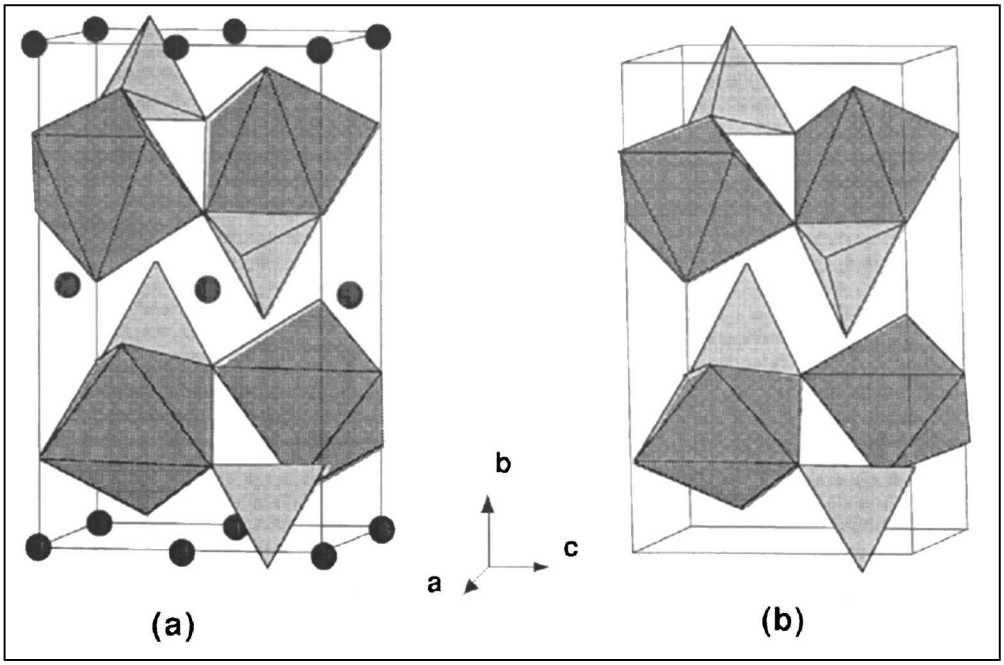

Figure 1-10 Schematic of the cathode material olivine phosphate. a) $LiFePO_4$ b) $FePO_4$

Table 1-7 Comparison of the electrochemical properties of common positive electrode materials for lithium ion batteries

Material	LiCoO2	$LiNi_{1-x}CoO_2$	$LiMn_2O_4$	$LiFePO_4$
Specific Capacity ($mAh.g^{-1}$)	~155	~205	~120	~170
V vs. Li	3.88V	~3.75V	4.0V	3.5V

There are other important aspects that must be considered in choosing the best positive electrode material for lithium ion batteries. For instance, the material should have high stability over a range of potentials against the electrolyte. Also in consideration should be the materials reversibility. In the lithium ion battery, the positive electrode will undergo repetitive volume changes to its structure when the

lithium ions are inserted and extracted and therefore materials that can integrate lithium reversibly with minimal structure change are of importance. The material should also maintain good electronic conductivity as well as high lithium ion diffusivity [25]. Kinetics is ultimately the limiting factor for the conversion of electrochemical energy into electrical energy within the cell and therefore fast accessibility of the electrons and ions is needed. Finally, fabrication costs tend to be the deciding factor of materials' ability to move from the research phase into full commercial production and therefore low cost synthesis processes are desired.

1.6 Negative Electrode

The final aspect of the lithium ion cell that needs to be discussed is the negative electrode. Like the positive electrode, the negative electrode should have good reversibility to undergo repetitive cycling so that lithium ions can be inserted and extracted from the material without destroying the electrode. For this reason, the material should possess good mechanical strength. A negative electrode with high discharge capacity is also desirable to maintain the overall high capacity for the cell. It is also of importance that the negative electrode has minimal reactivity with the electrolyte so that only a small portion of the capacity is lost to the formation of the SEI layer during the initial cycling. Finally, fabrication cost of the material should be reasonable for mass production.

One of the most tempting materials for use as the negative electrode was lithium metal, which initially found its way into the lithium ion cell in the 1970s through the early 1980s [25]. However, it was quickly realized that although its

electrochemical properties are the most appealing, other characteristics are actually detrimental towards proper use. Electrochemically, pure lithium metal has a theoretical specific capacity of 3862Ah/kg and a low voltage potential of only 0.0V [22,28]. It is also one of the lightest metals, making it a favorable option for maintaining a low weight device. But the downfalls of lithium metal outweigh its initial appeal, which mainly occurred during the process of recharging. In high temperature scenarios, unwanted deposition and shape change posed as some of the main issues with molten lithium as electrode materials [17]. Upon the recharging process, the electrode fails to resume its original structure, causing impairment to further cycling. For ambient parameters, dendritic growth occurs during the recharging stage. These structural inhomogeneities occur because of how the lithium metal surface reacts with the solution electrolyte. With the formation of lithium alkyl carbonates (part of the passivation SEI layer that will be discussed later), the electrode undergoes numerous cycles of non-epitaxial re-deposition of lithium, leading to increased surface area. Ultimately, the surface complexity of these continuous deposits cause uneven growth of the electrode causing finger-like growths that eventually short circuit the cell by a large rise in cell impedance or produce cell failure with the dendrites touching the positive electrode [29]. Other issues also included filamentary growth leading to the loss of material during subsequent cycling due to weakening in structure and thermal runaway caused by exothermic reactions of the electrolyte with new surfaces of the lithium metal [17]. These issues brought about the rise for simply utilizing lithium ions instead of lithium in its metal form.

Moving forward with negative electrodes employed by the hosting of lithium ions, carbon-based materials, initially amorphous coke then more specifically graphite, were the next most promising. Graphite has a theoretical specific capacity of 372Ah/kg and a potential of 0.05V versus lithium [22,28]. Structurally, graphite has a resilient layered structure that easily allows lithium insertion between these stacked layers for a maximum uptake of one lithium ion per six carbons. More precisely, graphite has an A-B-A-B-A stacking order which upon lithium insertion morphs into an A-A-A-A-A stacking as described in Figure 1-11. This process is highly reversible because of its systematic uptake and extraction of the lithium ions. The strong internal covalent bonding within each of the layers provides for desirable mechanical strength. Also graphite maintains relatively good charge-discharge retention with the formation of the SEI layer with values of 400mAh/g and 290mAh/g for charging and discharging, respectively [19]. Additional features for this material include good

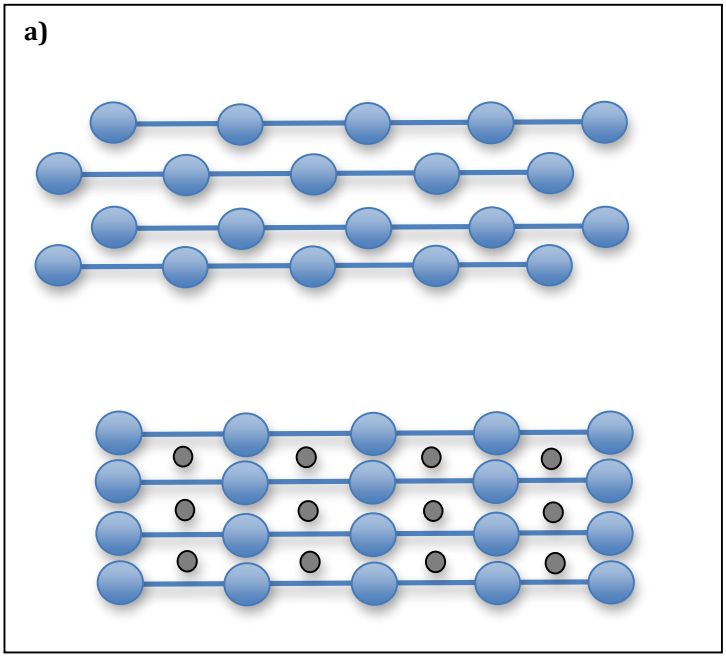

Figure 1-11 Graphite negative electrode. a) Prior to lithiation the stacking order for the graphite layers follows A-B-A-B-A order. b) After lithiation the layers become altered to A-A-A-A-A so that the lithium can sit as interstitials in the voids.

conductivity and compatibility with the other components of the cell. It also has a long cycle life of about 1200 cycles and is readily available. Other carbon materials that have been used in the past such as petroleum cokes have less organization throughout their structures and are inferior to that of graphite. In this case, it has been found that structure disorder has a direct effect on the reaction mechanism with lithium as described by Nazar et al [29].

1.7 Lithium Alloys

1.7.1 General Description

One important group of materials that has been heavily researched due to their higher capacity capabilities is lithium alloys. Periodic Table Group III, IV, and V metals and select transition metals are known to be highly reactive with lithium and undergo phase transformations when an electrochemical reaction occurs. These metals include: silicon, tin, antimony, aluminum, magnesium, bismuth, indium, zinc, lead, silver, platinum, gold, cadmium, arsenic, gallium, and germanium [28]. This group of materials is known to have much higher capacities, 2-5 times higher than that of carbon materials due to their much higher lithium uptake, which could greatly improve the application possibilities for the lithium ion battery by improving the energy density. Table 1-8 reviews a direct comparison of the electrochemical properties of some popular lithium alloys versus the present commercial negative electrode, graphite.

Table 1-8 Comparison of the theoretical capacity potentials for various lithium alloying materials and current commercial negative electrode graphite. *Some values have been adapted from Zhang [28].

Materials	C	Si	Sn	Sb	Al	Mg	Bi	Ge
Density ($g.cm^{-3}$)	2.25	2.33	7.29	6.70	2.70	1.30	9.78	5.32
Lithiated Phase	LiC_6	$Li_{4.4}Si$	$Li_{4.4}Sn$	Li_3Sb	LiAl	Li_3Mg	Li_3Bi	$Li_{4.4}Ge$
Un-lithiated Theo. Specific Cap. ($mAh.g^{-1}$)	372	4199	994	660	993	3350	385	1624
Lithiated Theo. Specific Cap. ($mAh.g^{-1}$)	339	2012	790	564	790	1782	350	1143
Un-Lithiated Theo. Specific Cap. Density ($mAh.cm^{-3}$)	837	9783	7242	4424	2682	4301	3763	9092
Lithiated Theo. Specific Cap. Density ($mAh.cm^{-3}$)	748	2374	2025	1878	1399	1782	1770	4687
Volume Changes (%)*	10	320	260	200	96	100	215	264
Voltage Potential vs Li (V)*	0.05	0.4	0.6	0.9	0.3	0.1	0.8	0.7

1.7.2 History

The first research that involved lithium alloys focused strictly on high temperature systems and mainly focused on lithium-aluminum and lithium-silicon as the targeted electrodes [29,30]. Although some of this work is still pertinent in the development of high temperature applications, a move towards ambient systems in the 1980s is where most of today's research and advancements stem from. The first commercial negative electrode utilizing lithium alloys was Wood's

metal (a combination of bismuth, lead, tin and cadmium) in 1983 [31]. It was also during this time that graphite was being investigated for its lithium intercalation phenomena which has led to its popular use today.

1.7.3 Reaction Mechanism

Based on the described possible reaction mechanisms for lithium ion batteries, alloy materials typically can undergo insertion or reconstitution reactions. Graphite and amorphous alloys, such as Si, all undergo the simple intercalation/deintercalation reaction, which inserts the lithium ions into the existing microstructure without any alterations [31,32]. This leads to stable retention and minimal structural damage to the alloying material. All the other lithium alloys undergo phase transformations through a displacement or conversion reaction, which tend to present some issues during repetitive cycling and will be discussed in the upcoming sections.

1.7.4 Potential & Capacity Determination

The potentials and capacity values for lithium alloys can be determined based on the thermodynamic properties and/or composition of the inclusive phases. Although experimental parameters typically are variable, the basis of these values can be calculated utilizing the binary and ternary phase diagrams as guidelines. This can be accomplished by utilizing phase diagrams in conjunction with the Gibbs Phase Rule as written in Equation 1.4:

$$\mathbf{f = C - P} \qquad \textbf{(1.4)}$$

where f is the number of degrees of freedom under equilibrium conditions, C is the number of independent components, and P is the number of existing phases. According to this rule, all intensive properties, such as electrical potential will be composition independent when no degrees of freedom are present, i.e. more than one phase is accumulated. Similarly, the electrical potential will vary with composition when one phase is present, therefore having one degree of freedom according to the Phase rule [17,32,33]. The schematics of Figure 1-12 show an adaption of this concept where potential plateaus are present with the existence of two phases and variable potentials occur when only one phase exists [34]. The values of these potential plateaus can be determined utilizing the Nernst Equation in Equation 1.5:

$$\mathbf{E_A = \Delta G_f^\circ \div nf} \qquad \mathbf{(1.5)}$$

where E_A is the reaction potential, ΔG_f° is the Gibbs free energy of formation of the product for the reaction, n is the number of electrons involved for the reaction, and F is Faraday's constant (96485 C/mol) [17,32]. The Gibbs free energy of formation values can be found typically from thermodynamic data tables.

In similar fashion, the theoretical capacity for any of the lithium alloys can be determined utilizing Faraday's constant and the following Equation 1.6:

Theo Cap. (mAh/g) = Stand Atomic Wt. × (# mol e- (rxn) ÷ mol material) × Faraday's Const. **(1.6)**

where the theoretical capacity can be determined by: the materials standard atomic

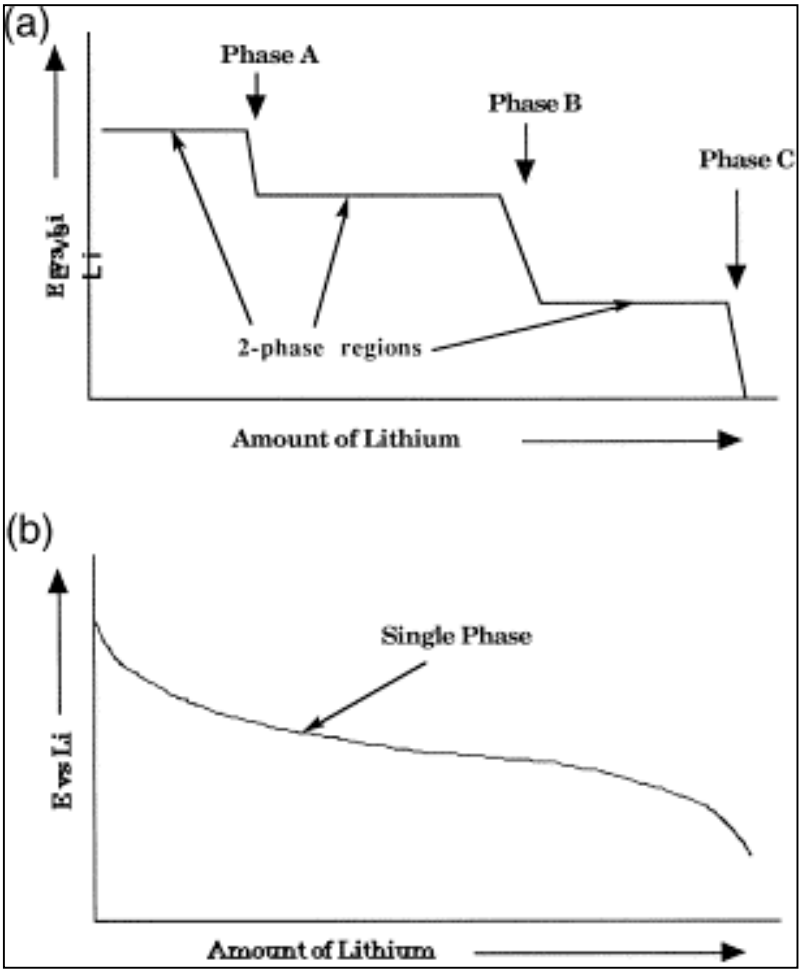

Figure 1-12 Determination of the alloy potentials based on its phase diagram and the Gibbs Phase Rule. a) Presence of 2 phases in composition makes intensive property (electrical potential) composition independent, plateau in potential seen. b) Presence of single phase makes the electrical potential dependent on the composition, variable potential across composition

weight, the number of electrons involved in the reaction to form the alloy, and

Faraday's constant. This same format can be utilized to determine the theoretical volumetric and areal capacities.

1.7.5 Detrimental Issues For Lithium Alloys

As seen in Table 1-8, although the high capacities of lithium alloys make them very appealing, some cycling issues do arise from their inherent properties. The most prominent is the volumetric changes that occur during lithiation and de-lithiation of the electrode. From Table 1-8, it can be seen that most of the commonly researched alloys undergo dramatic volume changes ranging from 100-300% of their original volume, which leads to mechanical strain on the material's microstructure [17,28]. Repeatedly enduring this structural transformation causes pulverization or decrepitation of the material and ultimately destroys the existing electrode. Huggins details this phenomenon as being similar to metal hydrides, in which fracture of the material continues until reaching the terminal particle size characteristic of the material [17]. Once reaching this smaller particle size the material will not continue crumbling further. However, this process typically causes loss of electronic contact resulting in decreased reversible capacity.

Lithium entrapment is another issue associated with the electrochemical use of lithium alloys. This problem may arise for a few different reasons but results in the lithium permanently confined to the host alloy. Slow kinetics is one possible cause in which lithium ions are not released quickly enough from the alloy phase [28]. Another motive is from the formation of highly stable lithium compounds, usually the result from the presence of S, P, O, and/or C impurities within the host

alloy material [28]. And finally, the large dimensional changes that occur during cycling result in high densities of defect sites at exposed surfaces and grain boundaries. These defect sites are optimal for strong bonding between the lithium ions because of the atoms having lower coordination, leading to irreversibility [28].

Another problem that can arise for lithium alloys includes reactions with surface oxides. Lithium is highly reactive with any existing oxides in the host material and tends to form the passivation oxide layer, Li_2O [28]. This irreversible reaction occurs typically between 0.8-1.6V and decreases the available lithium ions for the reversible cycling.

The solid electrolyte interface (SEI) layer formation with the use of lithium alloys poses as a prominent issue with further use past the first lithiation. The SEI layer, which will be discussed in further detail in a future section, is an important reaction that is needed for the reversible cycling of lithium ions. In most cases, the formation of this interface occurs only during the initial cycle and is responsible for the first-cycle irreversible capacity, as typical for the commercial negative electrode, graphite [28]. Lithium alloys repeatedly expose new surfaces with the reoccurring volume changes creating fractures within the material during cycling. This causes the formation of more of the solid electrolyte interface with increasing cycling numbers. Therefore lithium alloys introduce the new issue of the reversible capacity being diminished by the outgoing growth of the SEI layer.

The final issue that arises for lithium alloys involves the aggregation of the alloy particles or Ostwald ripening [17,28]. This concept occurs due to larger particles being energetically favored because the decrease in surface area to volume

ratio decreases the system's surface energy. This can occur because of pressure build-up from volume expansion creating a welding effect in which less host sites are available for lithiation. This process is also problematic because it increases the diffusion length for the lithium ions leading to slowing in kinetics and possible entrapment of SEI layers. Each of these described issues is a barrier that must be overcome if lithium alloys will be used effectively as negative electrodes moving forward.

1.7.6 Addressing Issues/ Improvements

In order to utilize lithium alloys for negative electrodes of lithium ion batteries, methods of improvement must be investigated. Therefore the main focus in lithium alloys has been concentrated in finding solutions for the catastrophic failure that occurs during cycling. Since there is no easy solution to avoiding the stresses associated with the volumetric changes, there are two approaches to managing these barriers and making this technology viable: macroscopic and microscopic solutions.

1.7.7 Macro-scale Solutions

From the macroscopic approach, the alloy material is combined with an additional component forming a multiphase composite. This additional component is thought to improve the dimensional stability by distributing the stresses so that the alloy material is less inclined to pulverization [34]. There are several options to form these multiphase composites, which include: an active matrix, inactive matrix, carbon-matrix composite, or a porous structure. For an active matrix composite, both components of the composite will react lithium. However, the two components are typically reactive at varying potentials and therefore result in a complementary system [28]. Depending on the potential, one component of the composite will react to form a lithiated phase while the other component will act as a buffer to offset the

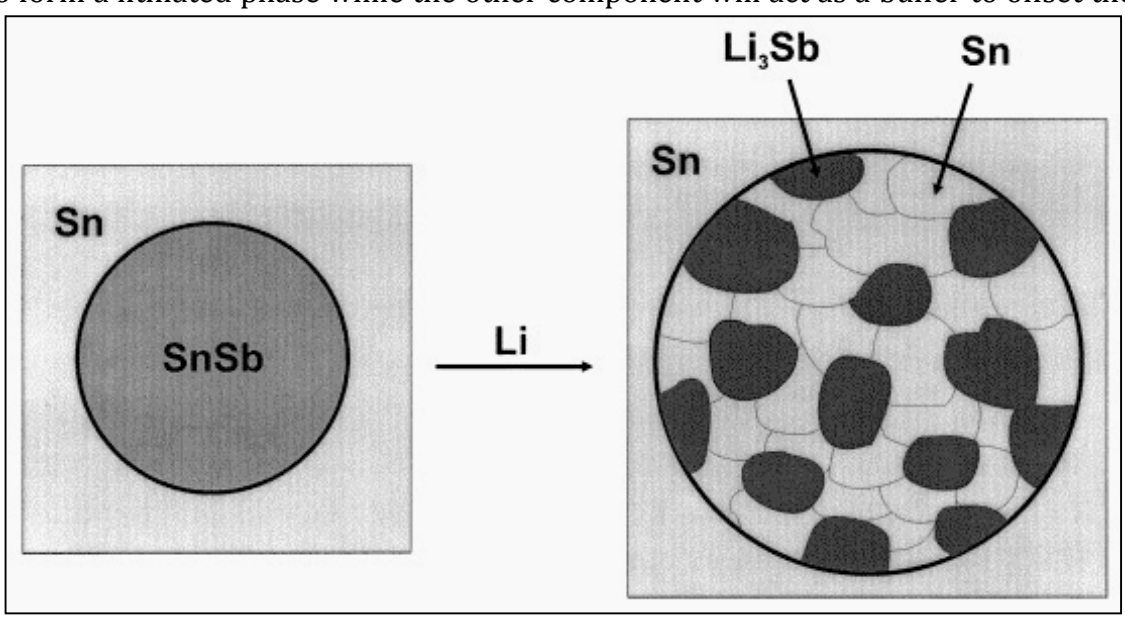

Figure 1-13 Schematic description of the lithiation process for the multiphase composite SnSb, which has an active matrix of Sn. Sn acts as the initial buffering matrix while Sb undergoes lithiation to form Li_3Sb. Further lithiation will result in the Li-Sn alloys, buffered by the no longer active Li_3Sb phase.

stresses incurred during this process. Likewise, once at a lower potential, the initial component will no longer become active towards the lithium and will become the buffer for the other component, which has become the lithiating phase. An example of this concept is the use of the SnSb alloy. Figure 1-13 schematically describes the initial lithiation for the following reaction in Equation 1.7:

$$\mathbf{SnSb + 3Li^{+} + 3e^{-} \leftrightarrows Li_3Sb + Sn} \qquad \mathbf{(1.7)}$$

In this case, the Sb is reactive with lithium while the Sn acts as a matrix buffer during its volume changes. The additional reaction is described in Equation

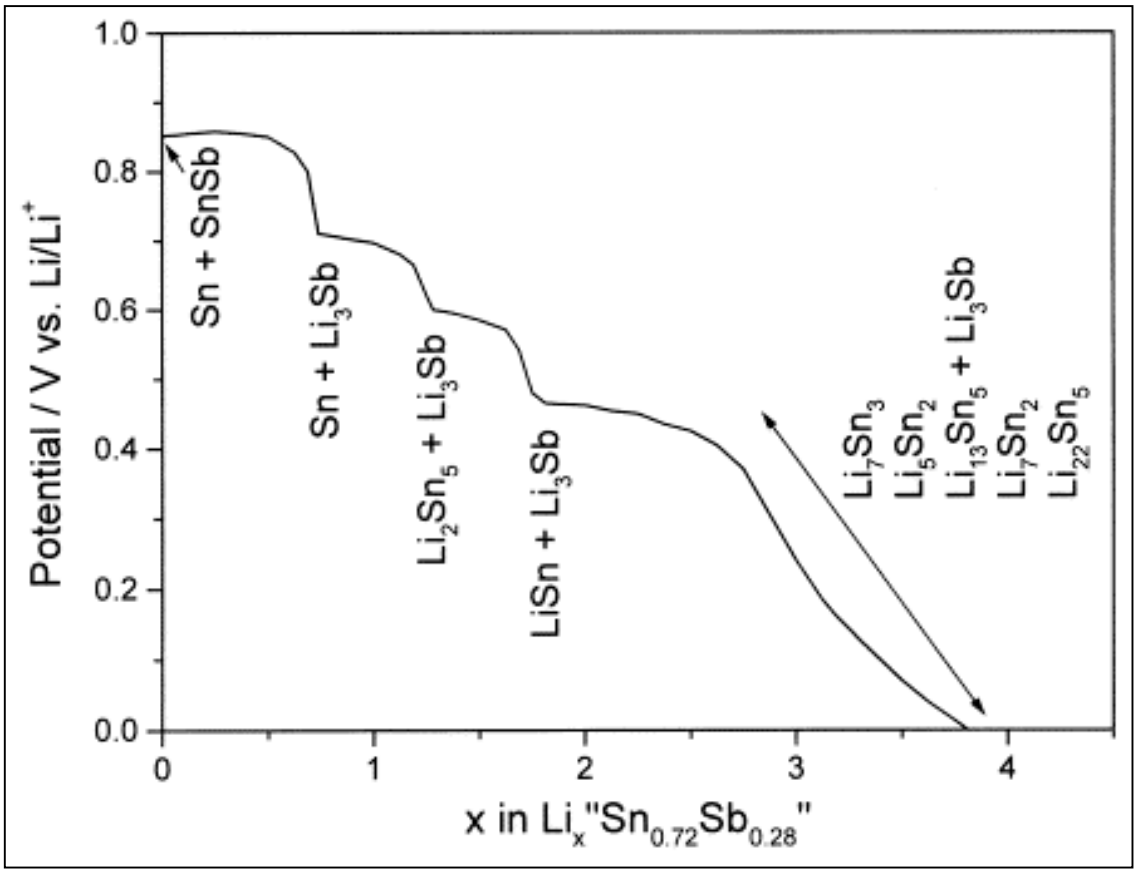

Figure 1-14 Characteristic potential curve for the lithiation of the SnSb multiphase composite. Lithium is first reactive with the Sb followed by the Sn within the composite.

1.8, which shows that the newly formed metallic Sn, displaced with the formation of the alloy Li_3Sb proceeds to react with additional lithium uptake, forming the Li-Sn alloy phases:

$$\mathbf{Sn + xLi^+ + xe^- \leftrightarrows Li_xSn} \qquad \mathbf{(1.8)}$$

Figure 1-14 details the full characteristic potential curve for the SnSb lithiation [35]. The electrochemical improvements with the use of the multiphase composite, alloy phase SnSb, are seen in the research of Simonin et al [36]. Figure 1-15 details this work, in which the alloy phase, SnSb is compared electrochemically with the pure metals and Sn-Sb that has been stoichiometrically mixed but not alloyed. From this data it can be determined that the composite has better capacity retention and the phase

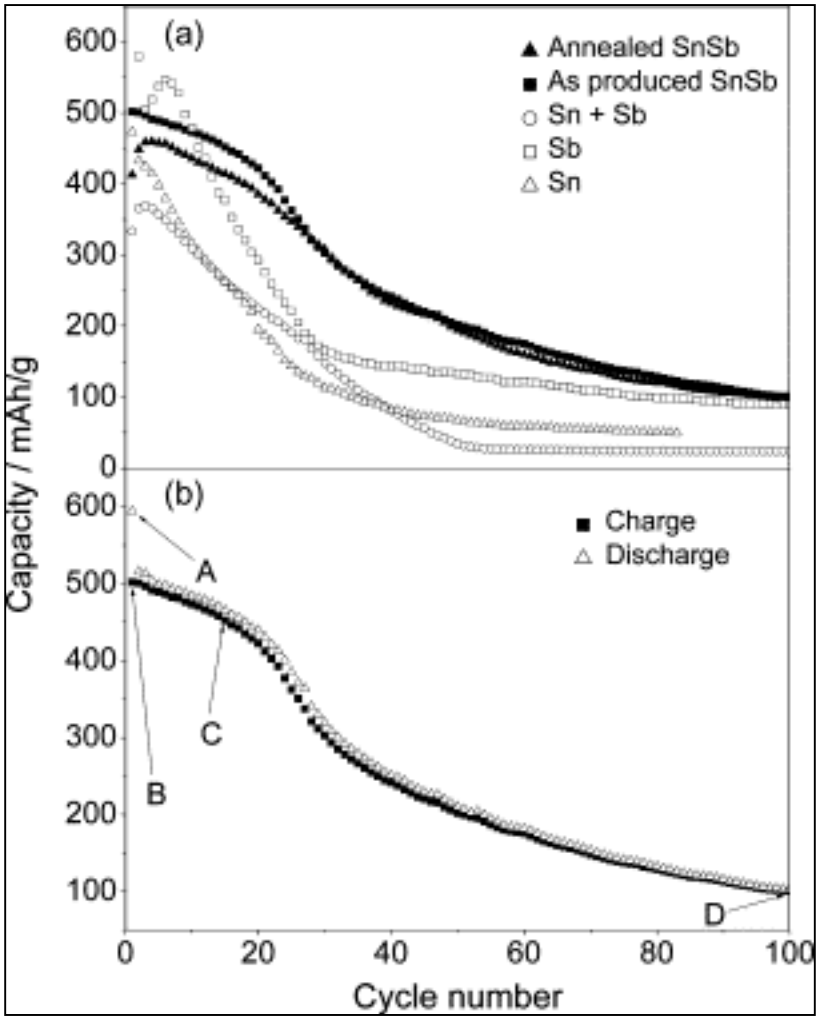

Figure 1-15 Experimental data for Sn, Sb, and SnSb mixtures and alloys. a) Comparison of charge capacities for the pure metals, mixed Sn-Sb, produced SnSb, and annealed SnSb. b) Cycle efficiency for the alloyed SnSb.

transformation that occurs in forming the composite is important in producing this improvement. Other active matrix multiphase composites include SbIn, $SbAg_3$, SbAl, SnAg, and Mg_2Si [28]. The one drawback to this concept is that the two phases still undergo the inherent large volume changes associated with the lithium alloy formations and therefore will show signs of decrepitation and capacity loss over cycling.

The next option that can be used to alleviate the concentrated stresses from the alloy materials is utilizing an inactive matrix composite. For this case, the matrix material is strictly used to buffer the alloy material and is electrochemically inert with lithium [28]. Examples of some inactive materials include: Fe, Cu, Nb, $FeSi_2$, Al_2O_3, Li_2O, TiN, SiC, TiC and TiB_2 [28,32]. The desirable properties of this matrix material include good ionic and electronic conductivities to assist in the diffusion of the lithium ions to the alloy host material. High mechanical and yield strength are also of importance to compensate for the extensive stresses and deformation that occurs with cycling. Li_2O has been heavily researched through the use of tin oxide and other transition metal oxides. For these cases, the initial oxide material is reacted with lithium to form the Li_2O inactive matrix with the metal active particles finely dispersed throughout [29,30,32,33]. The reaction descriptions are shown in Equation 1.9 and Equation 1.10:

$$\mathbf{MO_x + xLi^+ + xe^- \leftrightarrows M + xLi_2O} \qquad \mathbf{(1.9)}$$

$$\mathbf{M + xLi_2O + xLi^+ + xe^- \leftrightarrows Li_xM + xLi_2O} \qquad \mathbf{(1.10)}$$

In most cases, the Li_2O formed during the initial reaction with lithium ions is irreversible and therefore Equation 1.9 cannot be reversed and there is an

associated loss in capacity. An example of this is seen in the cycling of Fe_2O_3 in Figure 1-16. The described oxide starts with a capacity of 1000mAh/g on the initial discharge capacity but recovered only 720mAh/g on the charge capacity due to the irreversible losses with the formation of the lithium oxide inactive phase [28]. The use of SnO and SnO_2, which have been heavily investigated, will be discussed extensively in the upcoming section on tin research. Alternatively, there is also the option of using carbon-matrix composites. Carbon has already been proven to be a viable electrode material through its current use of graphite in today's lithium ion

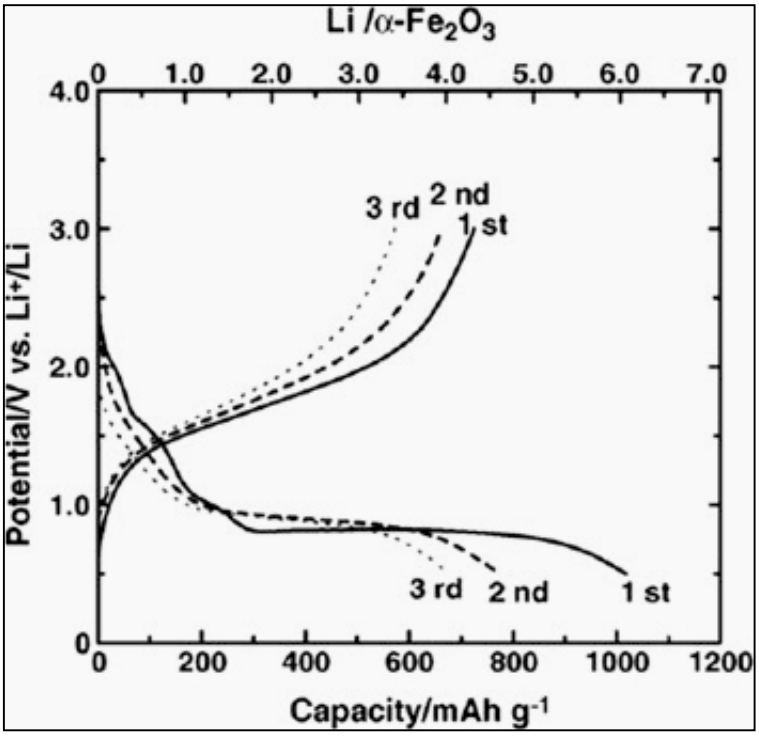

Figure 1-16 Initial charge-discharge curves for Fe_2O_3. The large difference in the 1st cycle is due to the large irreversible losses that cannot be recovered with the reaction to form Li_2O.

batteries. Some of the advantages of using carbon as the matrix material include its good ionic conductivity for certain configurations, tolerance to mechanical stresses and electrical conductivity [28]. These properties will allow the alloy material to increase its cycle ability even through fracturing of the material by providing pathways and connections for lithiation. Some of the other advantages of using carbon include its structure's free volume to absorb the stresses upon expansion-contraction of the alloy material and its ability to form a protective layer around its alloying active material [37]. An example of the carbon-matrix composite is shown

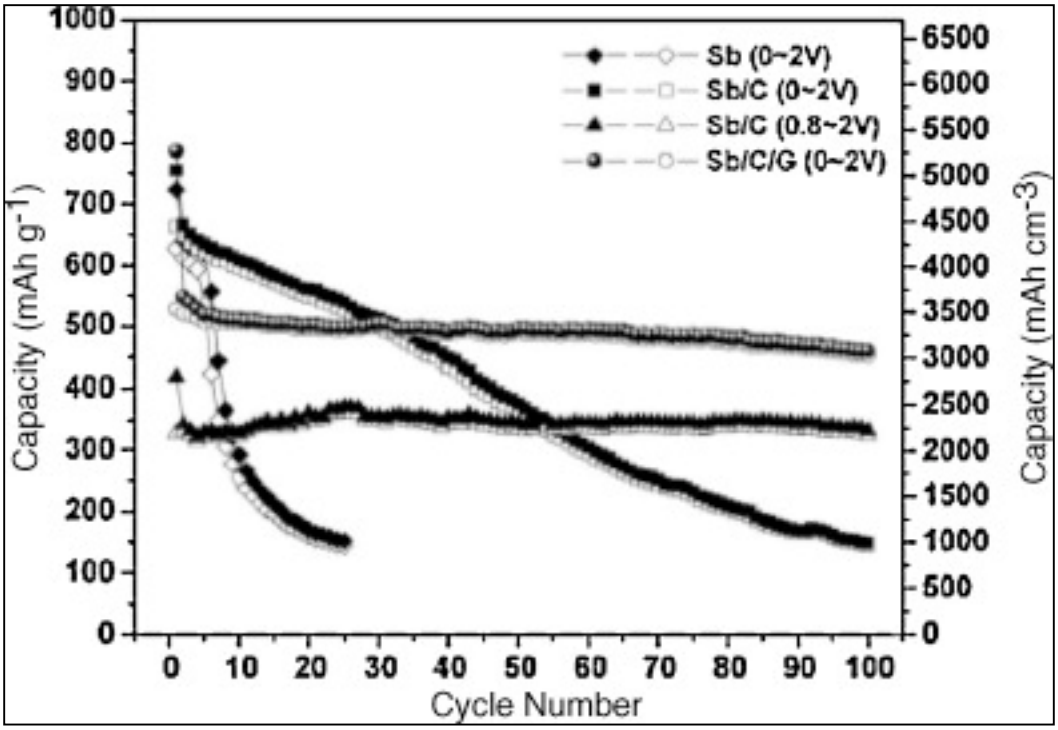

Figure 1-17 Adapted from Zhang [28]. The addition of carbon and graphite to the Sb greatly improve the capacity retention of the alloy.

in Figure 1-17, taken from Zhang, for addition with Sb [28]. From this cycle performance data, it can be concluded that the pure Sb begins to experience

detrimental failure by the 10th cycle. However, the addition of carbon with the same cycling parameters extended the cycling retention to approximately 30 cycles. The best results were seen from the composite with both carbon and graphite, which maintained cycling retention (500mAh/g) for nearly 90 cycles.

Finally the last option from the macroscopic standpoint is using porous structures for the composite material. This idea utilizes a matrix or substrate that can absorb the majority of the stresses from expansion and contraction by providing sufficient free volume through pores [28]. The structure's pores allow the alloy material to expand freely, which would help in the distribution of stresses. A balance between free space for expansion and actual active material is needed in order to maintain a practical volumetric energy density. The research by Yoshio et al. (Figure 1-18) is an example of a Ni foam current collector with silicon active material [38]. From the use of this porous structure, successful cycling of about 500mAh/g for

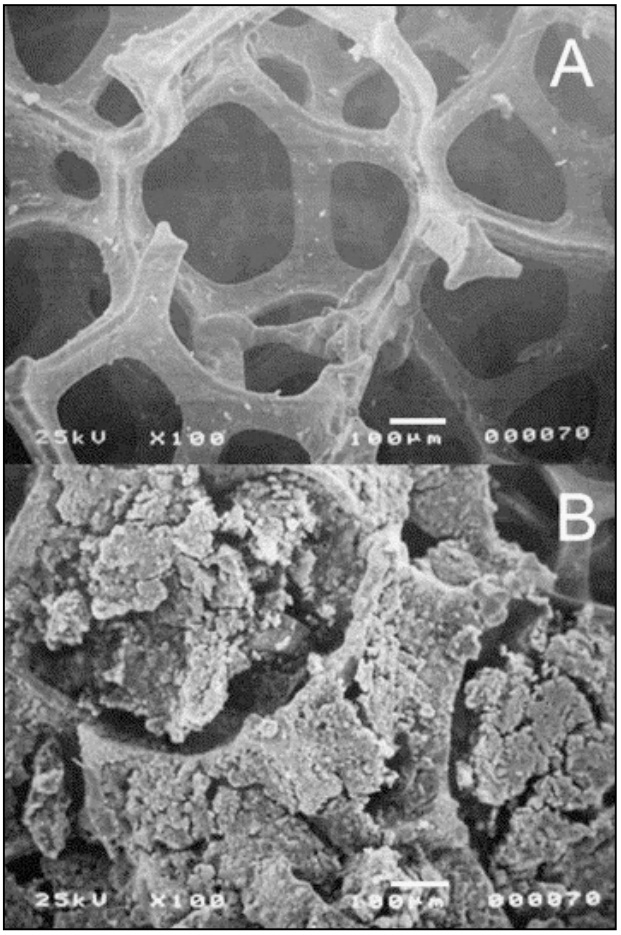

Figure 1-18 FESEM images for the porous structure data of Yoshio et al [38]. A) Image of the Ni foam current collector porous structure. B) Image of the Si electrode deposited on the foam structure.

approximately 400 cycles was achieved [28,38]. All of the discussed options aim to alleviate the stresses involved in cycling the alloy materials and are steps forward for making lithium alloys feasible for lithium ion battery negative electrodes.

1.7.8 Micro-scale Solutions

Now that we have considered the macroscopic approaches to fixing the main problems of lithium alloys, it is also important to look at the problems from the microscopic view. This solution involves maintaining control of the particle size. Reduction of the particle size to the nanometer range can help improve cycling by having better accommodation of the stresses. This is made possible by the increased yield and fracture strength that occurs in nanosized particles [28]. This helps in reducing cracking throughout the alloy material, which can lead to losses in active material. Primarily, according to fracture mechanics as described by Hu et al and Lee et al [39,40], when the particle size is below the critical size, the surface energy will be greater than the energy required for crack propagation and therefore fracture enlargement will not occur. This is based on Equation 1.11 described below:

$$\mathbf{d_{critical} = 2\gamma \div Z_{max} E \varepsilon_m^2} \qquad \mathbf{(1.11)}$$

where $d_{critical}$ is the particle size needed to avoid fracture, γ is the surface energy, Z_{max} is the maximum function of the crack length divided by the particle diameter, E is the elastic modulus, and ε_m is the elastic strain mismatch [41]. Nanosized particles can also be beneficial because of their shorter electronic and ionic transport pathways, which can help with the slow kinetics issues that were discussed earlier

[28]. Overall, the microscopic viewpoint looks to alter the morphology of the alloy material to suppress the electrode's reaction to strains in the material to improve upon the cycling stability.

1.7.9 Amorphous Research

Amorphous microstructures for lithium alloys provide more solutions in alleviating acquired stress and deformation during cycling. These materials have minimal long-range crystal structure and order; therefore do not experience the same directional mechanical stresses and strains that typical crystalline lithium alloys undergo. The volumetric expansion for these materials is more homogenous with isotropic stresses, which allow for the material to adjust evenly to the volume changes when the lithium ions are inserted and can therefore withstand repetitive cycling without the early introduction to decrepitation [35,28]. This can be contributed to amorphous alloys participating mostly in intercalation reactions.

A popularly researched example is amorphous silicon. The crystalline lithium alloy, $Li_{22}Si_5$ produces the highest theoretical capacity of 4200mAh/g but has an associated inhomogeneous volumetric expansion of almost 400%, causing extreme irreversible losses [28]. Sanyo Electric Co. fabricated micro-columns of amorphous silicon on a copper substrate with allowed spacing for volume fluctuations. Through this design and specific use of amorphous silicon, they were able to report initial coulombic efficiencies of 96% and a delithiation capacity of 3590mAh/g [35]. It should be noted, however, that degradation and pulverization still pose a problem for silicon due to its inherent transformation to a crystalline structure when

lithiating to high lithium alloys below 50mV. This can be avoided by limiting the operating voltage but will jointly limit the overall obtained capacity [28,32,35].

1.7.10 Tin Research

One of the specific lithium alloys that have been investigated over the past several years is tin metal. Tin is a fairly well understood metal that has been used for various applications for many years. It is known for its low modulus structure but also its brittle tendencies upon overworking the metal. Tin also can be used in its various easily formed alloy phases with metals such as copper, antimony, and lithium. As previously mentioned in Table 1-8, the theoretical capacity of the lithium tin alloy is 994mAh/g [28]. Figure 1-19 shows the phase diagram for lithium and tin so that a better understanding of their alloys can be concluded. The maximum lithiation that can be achieved is the $Li_{22}Sn_5$ phase also written as $Li_{4.4}Sn$. The phase transformations that occur to allow for lithium insertion are extreme and detailed in Figure 1-20. Of the seven alloys, six of the lithium alloys experience more than 50% volume change from its original structure.

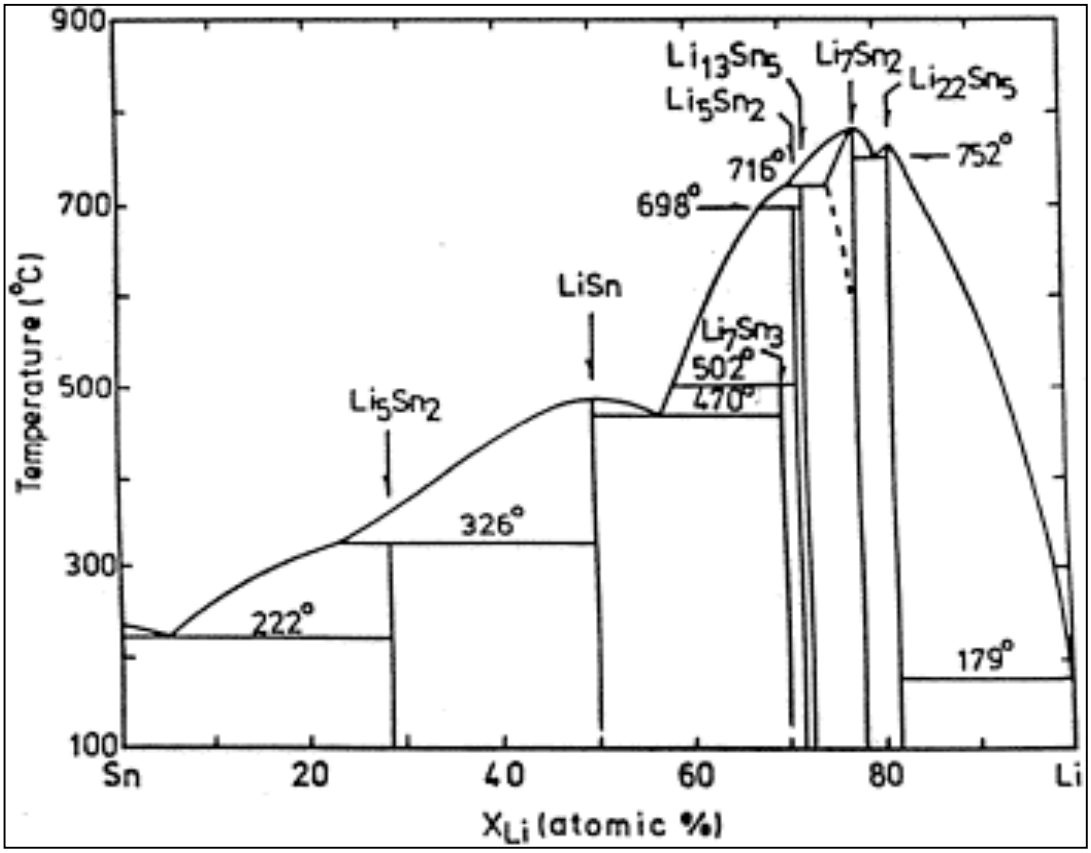

Figure 1-19 Lithium-Tin phase diagram showing all the possible alloy phases.

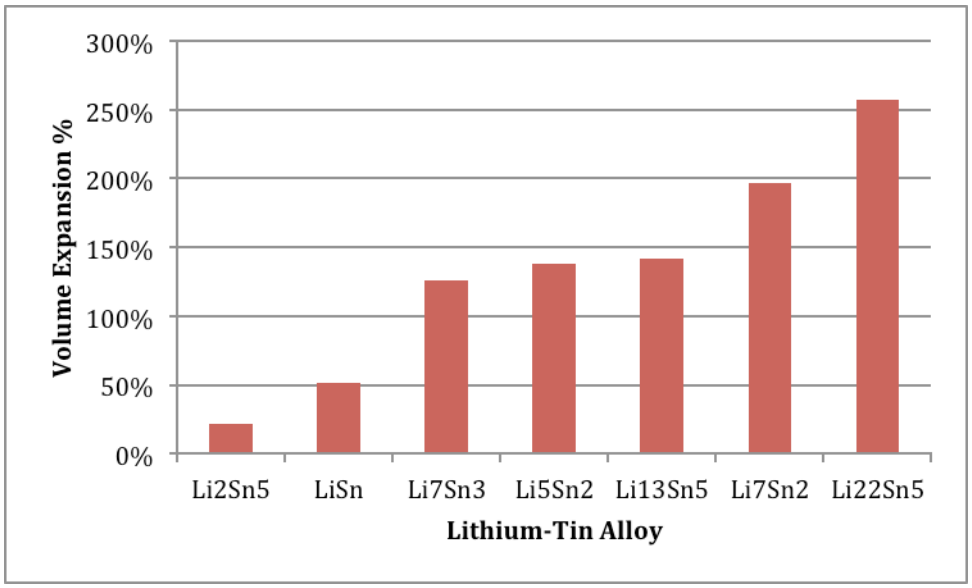

Figure 1-20 Evaluation of the volume expansion associated with forming each of the lithium-tin alloys

1.7.11 History

The oxide phases of tin were initially researched due to their ability to provide additional support during cycling with the formation of an inactive matrix. The process of forming the Li_2O inactive matrix with suspended tin particles led to a sacrificial portion of the capacity (irreversible losses) but extended the capacity retention contrary to pure tin. The potential curves for SnO and SnO_2 are shown in Figure 1-21 and 1-22 [30]. Although a large portion of the capacity is lost with these initial reactions, the stabilization is enough to make the electrode maintain a portion of reversible capacity, which is an improvement on the pure tin. The capacities for SnO and SnO_2 are compared in Table 1-9 adapted from Huggins [30].

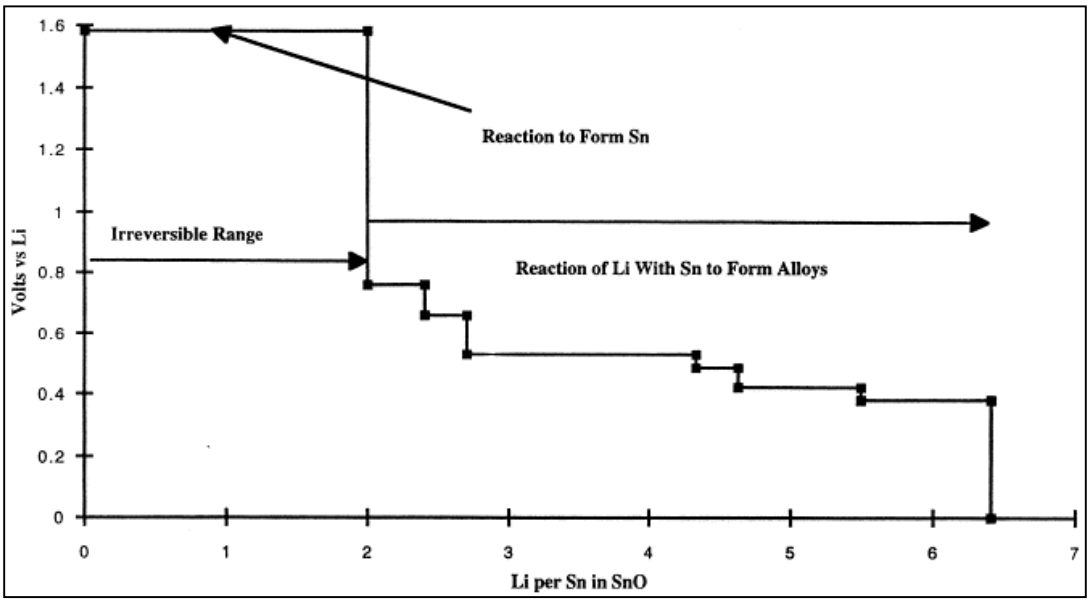

Figure 1-21 Titration curve for SnO showing the irreversible loss in conjunction with the formation of Li_2O the inactive matrix that improves cycle stability for Sn

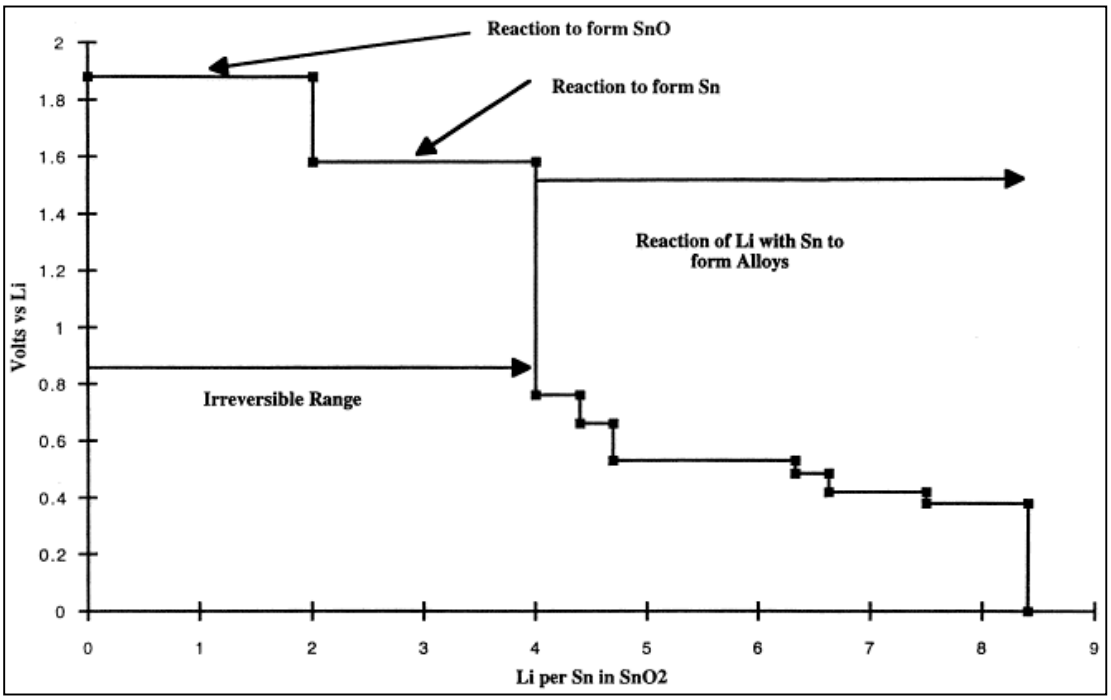

Figure 1-22 Titration curve for SnO_2 showing the irreversible loss for the initial reaction to form Li_2O.

Table 1-9 Theoretical capacities for the oxide phases of tin. The SnO phase has a lower irreversible loss due to the single O atom compared to the dioxide phase

Oxide	Oxide Total Capacity (mAh/g)	Irreversible Capacity (mAh/g)	Reversible Capacity (mAh/g)
SnO	1273	398	875
SnO_2	1494	711	782

Fuji Film publicized the first successful extensive work on lithium-tin alloys with their tin oxide composite (TCO), $Sn_xAl_yB_zP_pO_n$. This amorphous composite glass undergoes the initial irreversible reaction with lithium to form

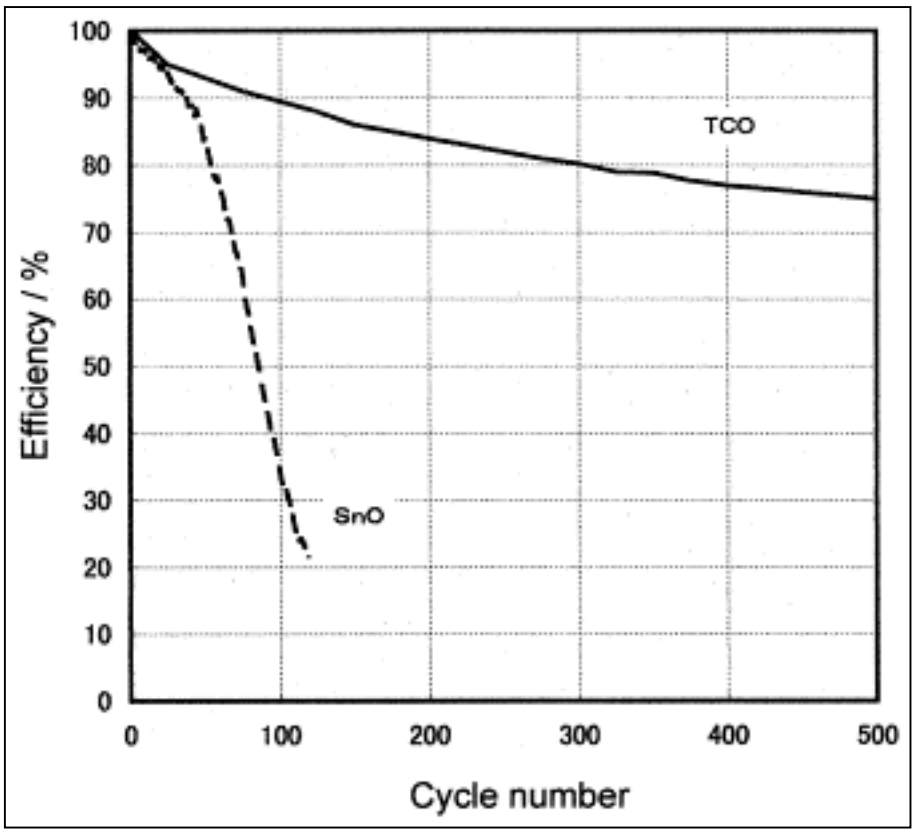

Figure 1-23 Comparison of TCO and SnO cycling efficiency. The TCO with the added glassy network formers B-P-Al show improved cycle ability.

dispersed nanoparticles of metallic tin in the glassy matrix, which then can be lithiated to form the lithium-tin alloys. The glassy matrix acts as a buffering inactive phase to help alleviate the acquired stresses. The additional glassy network formers actually showed improvements on cycling from the regular SnO and SnO_2 phases. This can be seen in Figure 1-23, which compares the cycling performance of TCO and SnO. The improvements are attributed to the additional network formers with the Li_2O better inhibiting the aggregation of the tin particles, which has been previously discussed as an issue for decreased capacity retention in lithium alloys [36]. However, over time, the energy density decreased dramatically, leading to research in other materials without oxides [35].

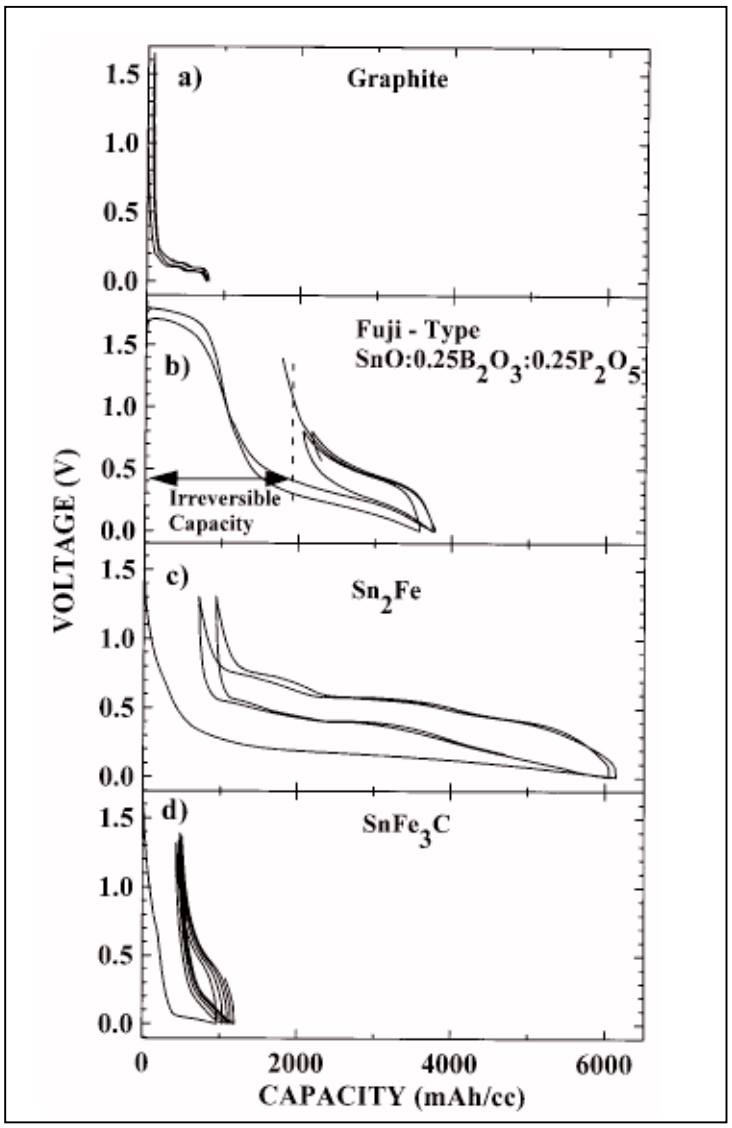

Figure 1-24 Comparison of the initial cycling curves for graphite, TCO, Sn_2Fe, and $SnFe_3C$. The SnFe3C had decreased irreversible loss.

Further improvement for tin utilization in lithium alloys came with the use of inactive

transition metals for the buffering matrix material. Areas of interest included systems containing Fe, Ni, Mn, or Co. The elimination of the oxide phases reduced the irreversible losses incurred with Li_2O formation. Due to the large volume changes, the delithiation process could lead to the dispersal of the tin particles throughout the inactive matrix instead of returning to its original structured material, eventually leading to electrode degradation. Proposed solutions to improve the cycle stability include increasing the inactive metal to tin ratio and the addition of carbon. Sn_2Fe and $SnFe_3C$ are examples of these materials that Dahn et al investigated and identified lower irreversible loss and improved capacity retention as seen in Figure 1-24 [42,29,43]. Although the irreversible loss for the lithium alloy ($SnFe_3C$) is still significant compared to graphite, the increased control allows for the better utilization of the alloy's higher capacity.

More recent investigations have focused on the intermetallic system of Cu-Sn. Figure 1-25 provides the phase diagram for this system. Copper is an advantageous component as the matrix of the composite electrode with lithium alloys due to its well-known properties and various applications it can be used for. It is already used throughout the lithium ion cell production as the choice current collector for the negative electrode. This is due to the fact that copper has excellent electrical conductivity. It also undergoes low reactivity with lithium and therefore will not affect the electrochemical properties of the cell during cycling. Other beneficial characteristics for copper include its soft and ductile structure, making it easy to work with [44]. For this reason, copper makes a great buffering material to absorb and better distribute the stresses incurred during the cycling of lithium

alloys. This helps to stabilize the structure of the composite and hopefully prolong the integrity of the active material. Also, as mentioned, copper has superior conductivity properties, which helps to prolong the cycling of fractured/disconnected alloy pieces through the creation of and intertwined network throughout the composite material.

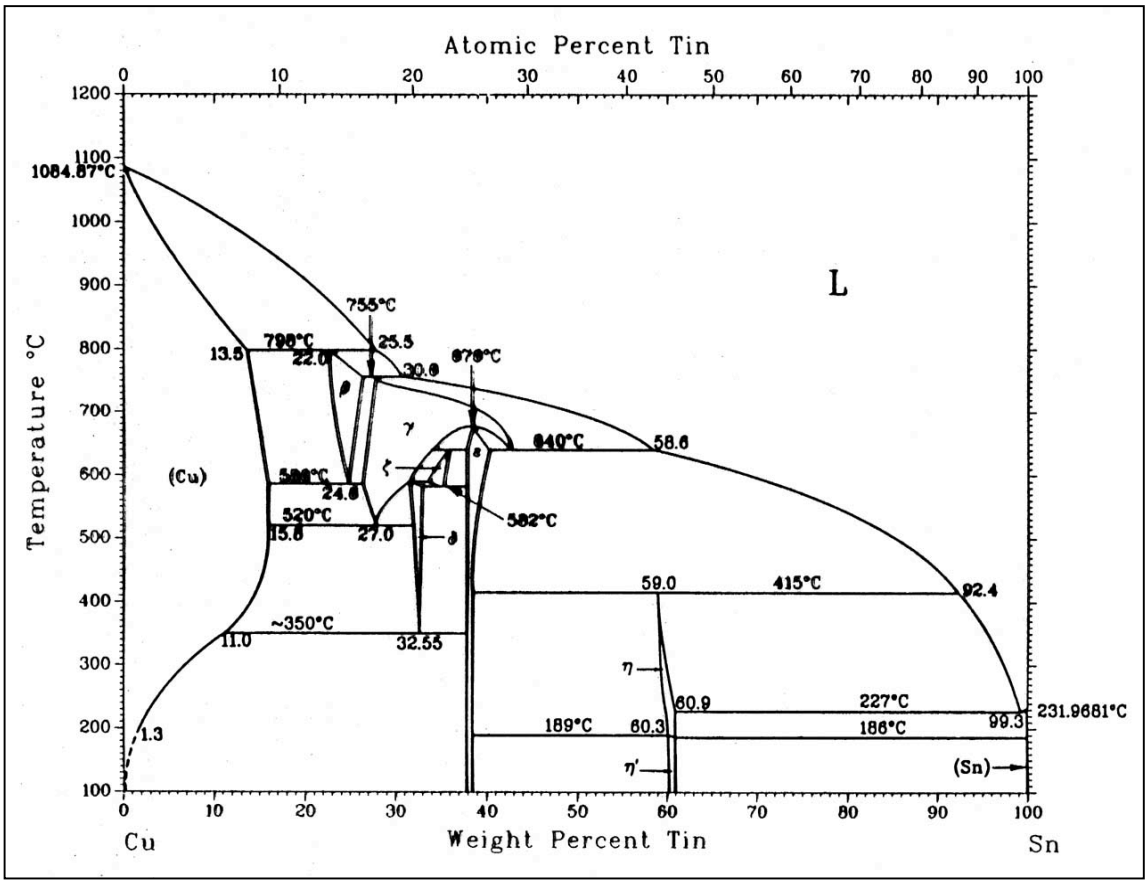

Figure 1-25 The phase diagram for the Cu-Sn system. Most lithium alloy research focuses on the η-phase (Cu_6Sn_5).

Thackeray et al introduced the Cu_6Sn_5 alloy with theoretically improved cycling stability due to formation of its intermediate phase during lithiation, which hosts lithium topotactically [45]. Unlike the Sn-Fe system, the Cu_6Sn_5 alloy has the

ability to form the lithium ternary Li_2CuSn through the following reaction in Equation 1.12:

$$\mathbf{Cu_6Sn_5 + 10Li^+ + 10e^- \leftrightarrows 5Li_2CuSn + Cu} \qquad \mathbf{(1.12)}$$

This ternary should accept further lithiation through the reaction in Equation 1.13:

$$\mathbf{xLi^+ + xe^- + Li_2CuSn \leftrightarrows Li_{2+x}Cu_{1-y}Sn + yCu} \qquad \mathbf{(1.13)}$$

where ($0 \leq x \leq 2.4$) and ($0 \leq y \leq 1$) [29,45]. Li_2CuSn phase has a Zintl crystal structure and therefore in theory should create hexagonal channels for the further lithiation from an insertion reaction mechanism similar to that of graphite instead of the typical conversion reaction that occurs for most lithium alloys. In practice, cycling the Cu_6Sn_5 across the full potential range to achieve the high capacity capabilities

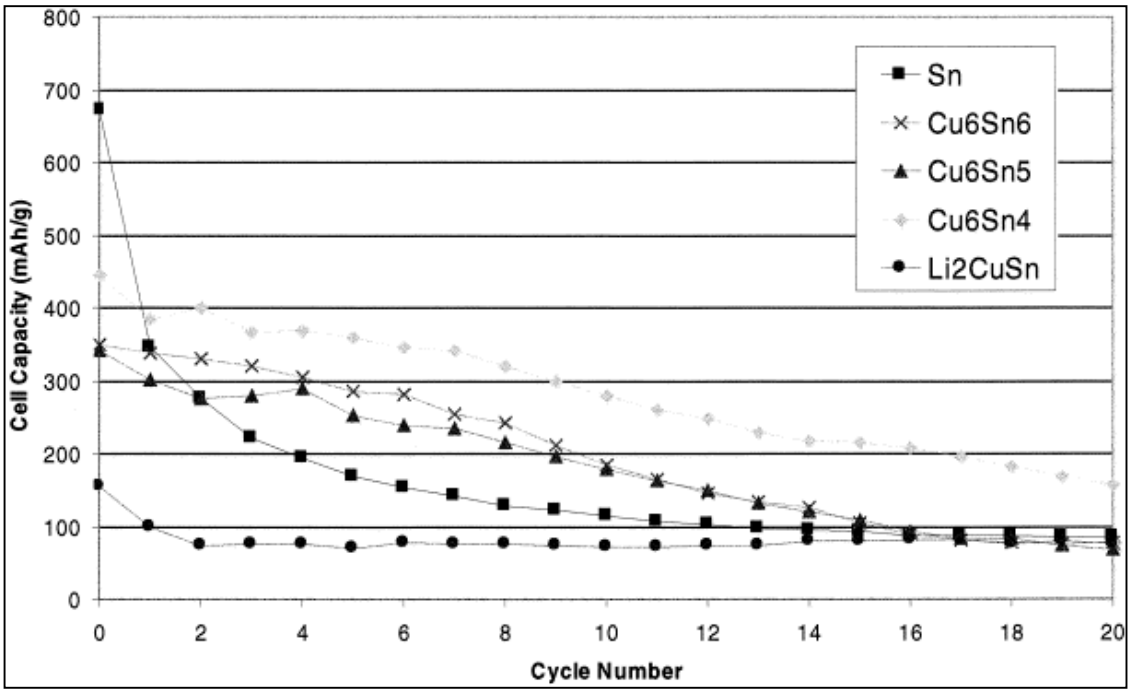

Figure 1-26 Comparison of cycling capacities for pure Sn, Cu_6Sn_6, Cu_6Sn_5, Cu_6Sn_4 and Li_2CuSn. The additional Cu in Cu_6Sn_6 provided additional support for better capacity retention. The Li_2CuSn phase had the worse cycling because it did not have the additional Cu typically formed from the initial lithiation of Cu-Sn alloy phase

induced the formation of the lithium-tin alloys and the full displacement of the copper inactive phase similar to the Sn_2Fe. Early results with experimental alterations to the stoichiometry of Cu_6Sn_5 are seen in Figure 1-26 [42]. From this data it can be seen that cycling the ternary (Li_2CuSn) as the initial phase was detrimental to the use of Sn for the negative electrode. However, the Cu heavy Cu-Sn alloy, Cu_6Sn_4 showed the most promising results with the first 8 cycles maintaining a capacity above 300mAh/g for the composite. When the capacity values for each of the composites are normalized for tin weight the true effects of the Cu matrix can be seen (Figure 1-27) [42]. The promising results of Cu_6Sn_5 (above 500mAh/g for 7 cycles) and Cu_6Sn_4 (above 600mAh/g for 7 cycles) prompted further investigation with fabrication optimization and composite additives.

The fabrication process of electrodeposition was investigated as an optimal

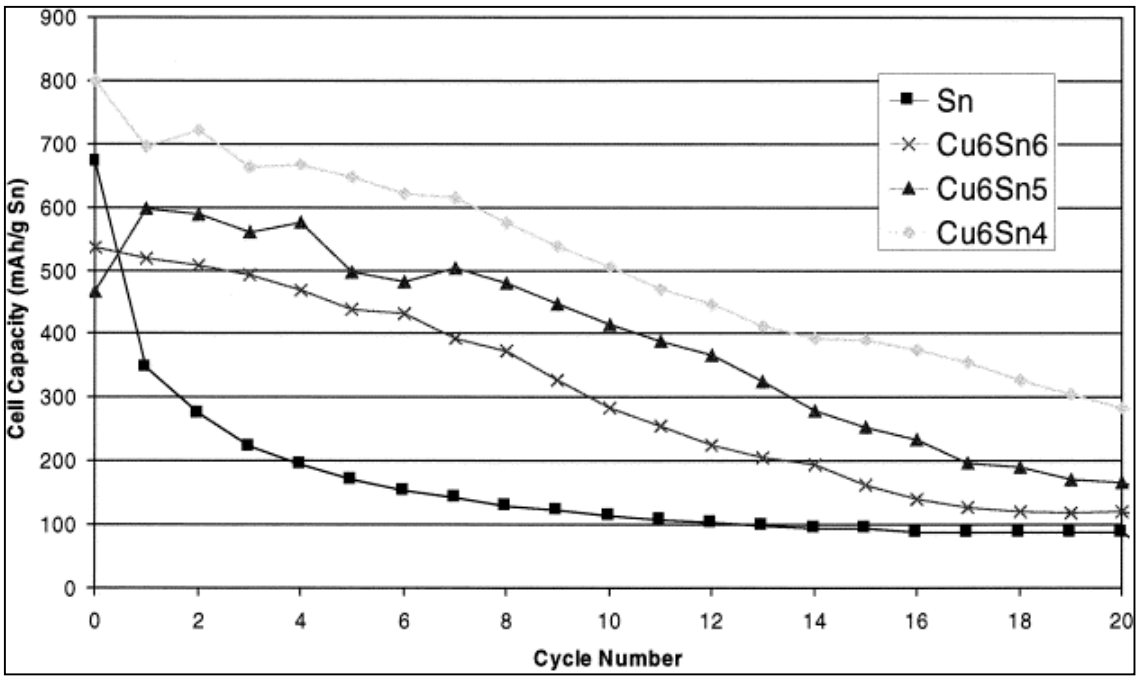

Figure 1-27 Normalized capacities for Cu-Sn alloys and pure tin.

tool for improving the microstructure of the Cu-Sn alloys to further enhance capacity retention during cycling in lithium ion batteries. Ke et al. and Trahey et al. described the use of this technique to fabricate macroporous and microporous structures of copper-tin alloys respectively [46 57]. In both cases, the electrochemical growth of the Cu-Sn alloys established porous microstructures with smaller particle sizes, which mechanically strengthened the electrode. The research of F. Ke et al. reported composite capacities of 400mAh/g for up to 40 cycles for films with 180nm pores and up to 30 cycles for films with 500nm pores [46]. Similarly, L. Trahey et al. made improvements by electroplating the Cu_6Sn_5 on a foam porous structure with a capacity of 670mAh/g for almost a steady 30 cycles after the initial drop off [57]. Dahn et al also utilized electrodeposition but with a pulsing technique and mixed Cu-Sn solution to intricately obtain the desired stoichiometry for cells of Cu_6Sn_5 of composite capacities 400mAh/g for up to 40 cycles and 175mAh/g for up to 70 cycles with a modified cycling range [47]. Dahn's further work incorporated graphite as an additive for sputtered and milled (Cu_6Sn_5) material for electrode tapes. This addition excelled the capacity retention above all previous investigations with 400mAh/g composite capacity for over 100 cycles [48]. It was concluded that the additives of graphite increased the electronic conductivity to provide networking of the alloying material even during fracturing. Table 1-10 provides a comparison of some tin research achievements that have been made over the past years [42,45,46,47,48,57,49,50]. These examples portray a wide range of capacities with some of the materials having good volumetric capacity and others having low irreversible loss. Careful evaluation concludes that no solution has been

found as of yet to allow for the lithium-tin system to be used for negative electrodes. However, these examples show promising potential, which can be used as building blocks for even greater improvements with new ideas and techniques.

Table 1-10 Comparison of some researched lithium-tin alloying compositions

Material	Irreversible Loss (1st Cycle)	Cycle Life (20% 3rd Cycle)	Gravimetric Capacity (mAh/g) 5th Cycle	Volumetric Capacity (mAh/cc) 5th Cycle
TCO (Sn_2BPO_2)	51%	> 20	500	1615
Sn_2Fe	15%	20	500	984
$SnFe_3C$	40%	50	550	700
Cu_6Sn_4	N/A	10	375	480
Microporous Cu_6Sn_5 500nm pore dia	32%	33	500	2389
Macroporous Cu_6Sn_5 Foam precursor	43%	5	670	705
Electrodeposited Cu_6Sn_5	10%	50	390	3116
Milled Cu_6Sn_5 + C	21%	15	440	578
Sputtered Cu_6Sn_5 +C	13%	10	502	287

1.8 Solid Electrolyte Interface (SEI)

As discussed earlier, an imperative solid electrolyte interface layer forms during the initial cycling to prohibit further reaction of the negative electrode with the electrolyte. Typically, this passive layer formation occurs during the initial cycling due to the electrolyte's unstable thermodynamics with the high/low potentials versus Li/Li^+ [51]. This interface layer is crucial for proper cycling in lithium ion batteries because it prevents electron transport by ceasing electrolyte degradation, establishes a pathway for Li+ conductivity between the electrode and

electrolyte, and protects the electrode material from further electrolyte reactivity. A balance in thickness for this layer is needed to prevent insulation and resistance build up if the film is too thick and to prevent further reactivity if it is not thick enough. The SEI layer is typically comprised of several different inorganic and organic electrolyte decomposition products but its exact composition is variable due to its dependence on the electrolyte's composition, electrode morphology and nature, and cycling parameters. Typically formation occurs between 0.8-2V.

Table 1-11 Typical SEI components found for lithium ion batteries listed with their most common electrolyte sources. Adapted from Verma et al & Agubra et al. [51,52].

SEI Component	Typical Source
Li_2CO_3	Ethylene Carbonate Propylene Carbonate Semicarbonate
LiF	Fluorinated Salts
LiOH	H_2O Contamination
$Li_2C_2O_4$	Ethylene Carbonate Dimethyl Carbonate
HCOLi	Methyl Formate
Polycarbonates	Ethylene Carbonate Propylene Carbonate Dimethyl Carbonate Ethyl Methyl Carbonate
Li_2O	Li_2CO_3 Degradation
ROLi	Ether Electrolytes Dimethyl Carbonate Ethyl Methyl Carbonate
$ROCO_2Li$	Propylene Carbonate Ethylene Carbonate
$(CH_2OCO_2Li)_2$	Ethylene Carbonate

Table 1-11 lists some of the commonly reported SEI components [51,52]. Other common byproducts also include gases such as CO_2 or C_2H_4, which can lead to negative side effects in the presence of H_2O contaminants and create cell venting

[52]. With the formation of the solid electrolyte interface, a portion of the negative electrode's capacity will be reduced because of the surface material becoming incapacitated for lithium ion acceptance with the formation of this 'bridging' layer. This capacity decrease that occurs because of the SEI formation, normally in the first cycle is known as irreversible loss. For graphite, the current commercial negative electrode, the SEI layer forms completely during the first cycle and the irreversible losses are low (12-13%).

Lithium alloys experience a constant growing SEI layer with cycles due to their large volume changes within the electrode creating new surfaces that are freshly exposed to the reactive electrolyte [28]. This process causes the formation of additional solid electrolyte interphase layers and increases in the irreversible loss throughout the entire cycling of the cell. Figure 1-28 schematically depicts the growth of the SEI layer for a lithium alloy material.

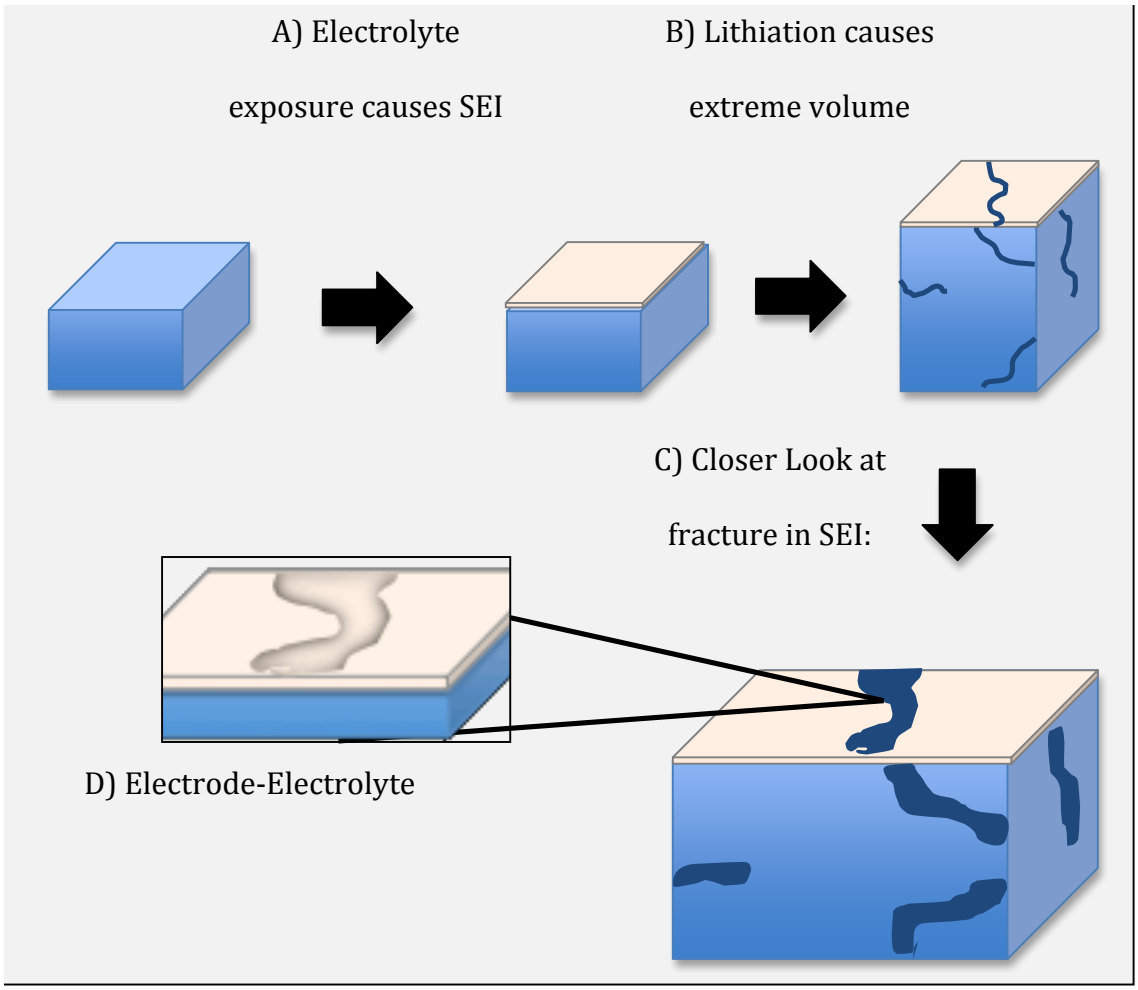

Figure 1-28 Schematic depiction of electrode-electrolyte interaction for lithium alloys. A) An initial reaction of the electrolyte with the negative electrode causes the formation of the SEI layer. B) Volume changes during lithiation cause fracturing. C) Fracture in SEI and Electrode expose new surfaces to electrolyte. D) Further reaction forms new SEI on electrode new surface.

Electrolyte additives have been investigated for use with lithium alloys to help create a more stable SEI layer to improve capacity retention and decrease accumulated irreversible loss. The most commonly used additives are vinyl carbonate (VC) and fluoroethylene carbonate (FEC). Figure 1-29 analyzes the effects of VC additive for the cycling stability of a silicon negative electrode material [53]. Although a decrease in the capacity retention is still seen for the cell cycling with the VC additives, the degradation and/or increase in irreversible loss is delayed. It has been concluded that such additions to the electrolyte alter the morphology and chemistry of the SEI layer so that there is an increased homogeneity in the interface and contains more stable components. Chen et al describe the limitation of isolated

LiF crystals, which are permeable to further electrolyte degradation and a smoother SEI surface as reasoning for improved cycling characteristics for the VC additive cell [53]. Similar results were seen with the Wilhelm et al research studies of VC and FEC, which attribute the additives forming flexible long chain polycarbonates in the SEI layer, leading to less electrolyte/electrode interaction with the extensive volume changes [54]. Figure 1-30 provides the supporting electrochemistry results for the inclusion of VC and a mixture of VC and FEC with a TiSnSb electrode. From this data it can be seen that rapid increase in the irreversible losses (associated with electrode/electrolyte interactions from volume change new surfaces) for the films with the electrolyte additives did not occur until about 80 cycles, whereas the standard electrolyte underwent rapid increase between 40-50 cycles. These alterations in the cycling habits for lithium alloys may not be a complete solution to the inherent issues stunting lithium alloys use as negative electrodes, but these additives do provide a pathway for adaption.

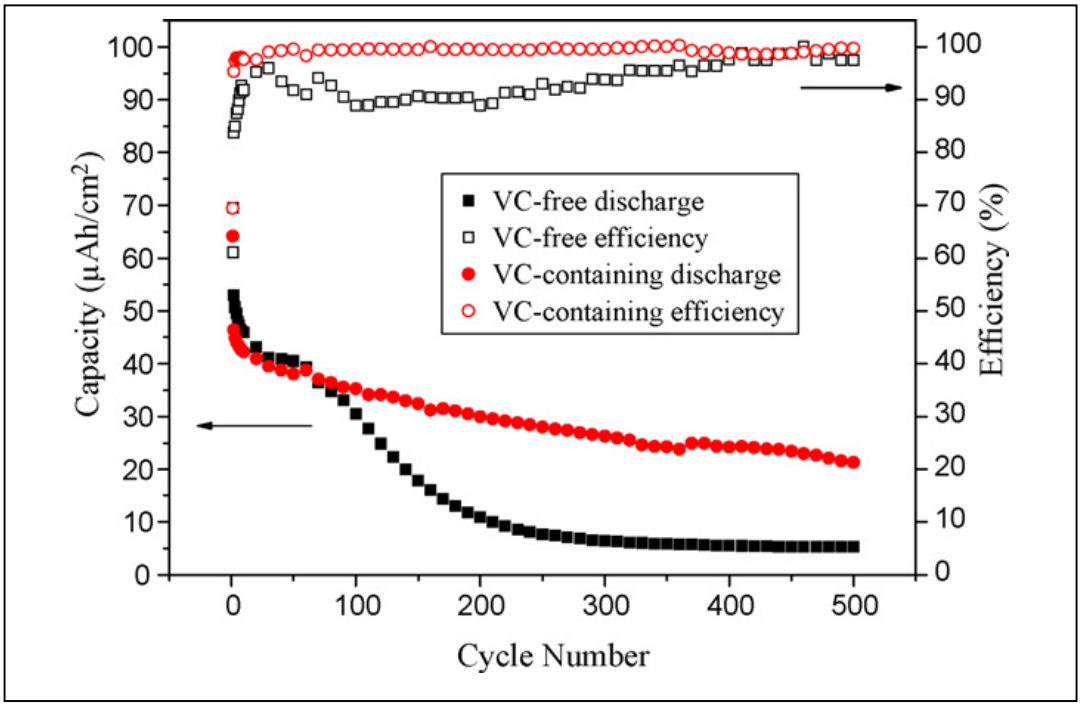

Figure 1-29 Comparison of cycling capacity retention for silicon lithium alloy negative electrode with focus on the effects of VC additives to electrolyte.

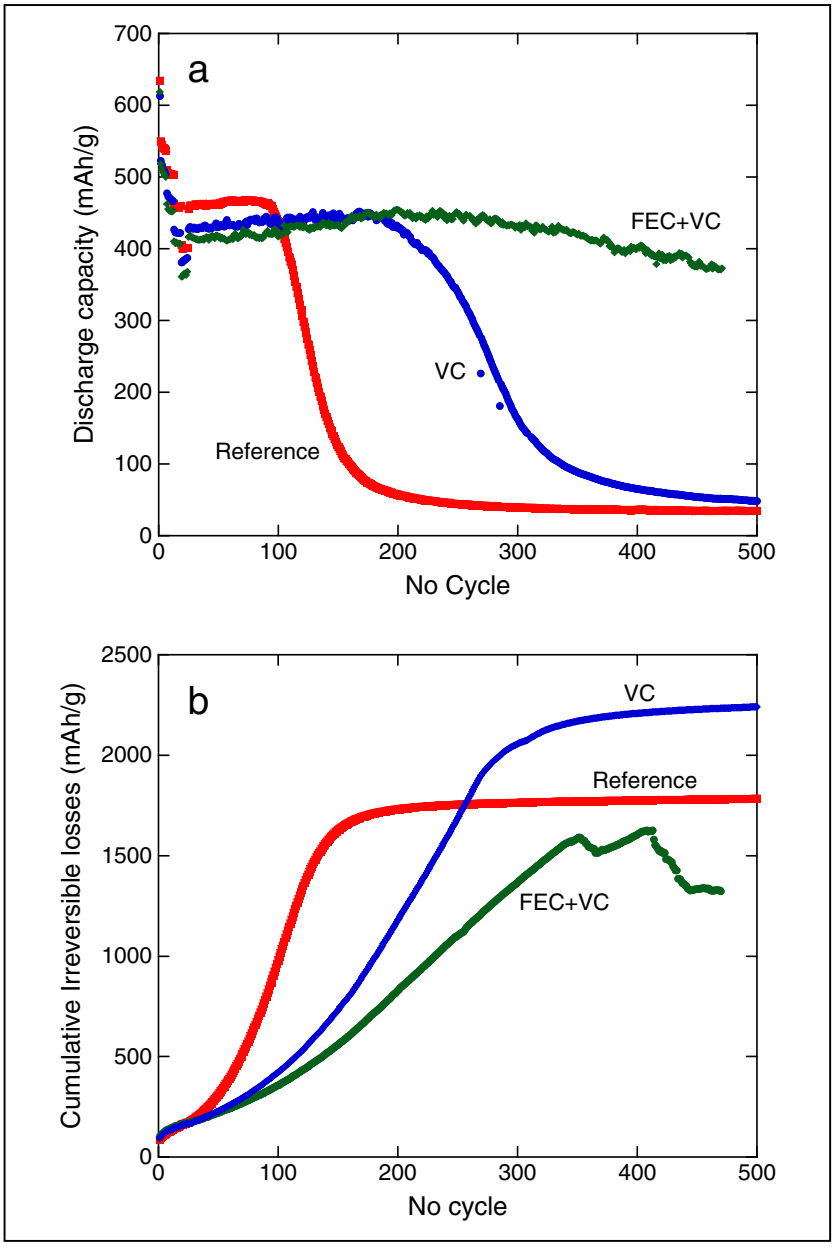

Figure 1-30 Cycling analysis for VC and FEC additives with a TiSnSb electrode. a) Comparison of capacity retention shows the improve capabilities with the additives. b) Comparison of the accumulated irreversible losses shows a delayed increase for the cells with VC and FEC mixtures.

1.9 Fabrication Process: Electrodeposition

As briefly mentioned, electrodeposition is a beneficial fabrication technique that can intertwine macroscopic and microscopic solutions for lithium alloys to improve its cycling capabilities for lithium ion batteries. This technique utilizes electrical currents to establish layers of metal on the surface of a substrate [55]. This can be accomplished with the use of a liquid solution containing the desired metal ions and the application of electrolysis through the electrodes by means of an external power source [55,56]. Figure 1-31 gives an example of a typical electrodeposition plating bath setup. The liquid solution, the plating bath, is typically an aqueous solution made of dissociated metal salts. Similar to the setup of a battery, the electrodeposition process requires two electrodes connected through a power supply. Upon negatively charging the cathode material through this power supply, the metal ions within the bath move towards this surface because of the electric field that has been created with the anode being positively charged. Once reaching the negatively charged surface of the cathode, the metal ions are removed from the solution through electrolysis to form a coating of metal on the surface of the cathode [55].

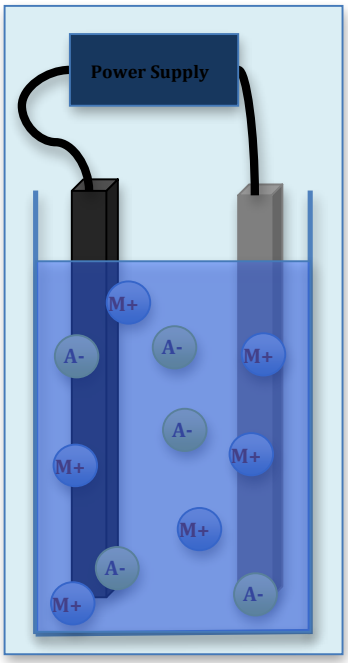

Figure 1-31 Electrodeposition bath setup composed of metal ions & current supplied to electrodes through an external power source.

To fully grasp the electrodeposition technique, it is important to discuss some of the fundamentals. As mentioned, this process evolves around the movement of electrical current through an outside source to produce electrochemical reactions on a working substrate. The current density is the defining property of the solution and electrode interface that controls the rate of deposition. This property is limited by the transport of the metal ions from the bulk of the solution to the surface of the electrode [56]. There is a defined thickness for the area of the solution near the electrode surface that experiences deficiencies in the metal ion concentration due to the formation of the metal at the electrode-solution interface. This layer is known as the double layer or Nernst diffusion layer and controls the current density for electrodeposition in the plating bath. The equation for the relationship of the current density to this diffusion layer is defined in Equation 1.14:

$$\mathbf{i_L = ((nFD)/\delta).\ c_b} \qquad \mathbf{(1.14)}$$

where i_L is the current density, n is representative of the number of electrons involved in the reaction, F is Faraday's constant, D is the diffusion coefficient, δ is the thickness of the diffusion layer, and c_b is the concentration of the metal ions in the bulk solution [56]. Another important concept used in electrodeposition is Faraday's law. This law states that there is a defined amount of electrochemical reaction that will occur for a given amount of electric charge [55,56]. This is a theoretical value that does not take into account the additives in the solution for brightening and smooth coating characteristics. The efficiency of the solution will therefore never be 100% due to side reactions that occur from these additives in the solution [56].

There are two types of electrodeposition that ultimately affect the film morphology: constant and pulsing techniques. In constant deposition, the current or potential is applied as a set parameter until film thickness has been accumulated. This type of electrodeposition usually fabricates films of larger grains through the growth mechanism of nucleation-coalescence, which occurs when isolated seed crystallites grow three dimensionally until combining to form larger networks leading to a continuous film [56]. Pulsing electrodeposition applies the current or potential in set intervals (rectangular, periodic-reverse, or symmetric sinusoidal pulses) [56]. In the rectangular pulse setup, the current or potential is applied for a set time followed by a set time of no applied current or potential. The periodic-reverse pulse deposition is similar to the rectangular pulse waveform except during the time off, the polarization is switched from cathodic to anodic. Finally, the sinusoidal pulse waveform applies the current or potential through the summation of a direct cathodic current and a sinusoidal alternating current. These alterations in the electrolysis are advantageous for films composed of smaller grains, which accrue from the growth mechanism of layer growth. Layer growth occurs from nucleates forming steps along the surface of the substrate cumulatively until a full layer of deposit is formed. Layer growth also can occur from nucleates forming steps at various positions along the substrate until accruing for a full layer [56]. Pulsing the current or potential does not give the formed nucleates time to continue growth into larger crystallites because of the intermittency of the electrolysis.

Additives are crucial constituents for plating bath solutions due to effects on chemical and physical adsorption on the surface of the substrate [56]. From the

chemical adsorption perspective, such components facilitate the exchange of electrons from the substrate with the metal ions of the solution, accelerating the deposition of metal on the surface. In the physical adsorption perspective, additives utilize van der Waals forces to attract the metal ions of the plating solution to the plating substrate. These characteristics act as catalysis in nucleation and growth of the metal films by altering the concentration of growth sites, the concentration of metal ions from the solution, the activation energy of the surface, and by lowering the diffusion coefficient of the metal ions [56]. Solution additives will also affect the film morphology, structure, and appearance.

Electrodeposition is a fabrication technique that can be beneficial for lithium alloys because of its ability to fine-tune compositions and physical properties of the plated metal through adjustments in the metal ion solution and deposition conditions [57]. This can be accomplished by the addition of additives and/or surfactants as mentioned previously. Also, adjustments in concentrations of the solution composition can play a role in surface properties of the plated metal. This process is favorable because of the strong electrical contact the deposition makes with the substrate forging bonds created electrochemically [55]. Much effort would be needed to break apart these newly formed bonds, which can be beneficial for the lithium alloys when undergoing extreme volume changes. This could prolong the cycling of the material before complete decrepitation is reached. The final advantage of utilizing electrodeposition for lithium alloy electrodes is the fact that the process is commercially viable [55]. Unlike other film depositing techniques such as e-beam evaporation, chemical vapor deposition, atomic layer deposition, pulsed laser

deposition, and molecular beam epitaxy, electrodeposition can be executed in ambient conditions. This helps in lowering the overall cost of the process and therefore in the long run could drive down the pricing of these negative electrodes. The plethora of solution options for this process also establishes a wide selection of plating possibilities so that end results can be refined according to the user's desire for specific products.

1.10 Our Research

In this paper, the utilization of electrodeposition for the fabrication of heterogeneous lithium alloying materials will be described in full detail. The described fabrication technique, meniscus brush-plating electrodeposition, is unique in that it is the first of its kind at the macro scale creating freestanding films. This process is advantageous for its ability to limit the nucleation growth with the introduction of a mechanical 'pulse' by the simultaneous movement of the counter and working electrodes during the plating process. The elimination of the typical bath solution setup and addition of a reservoir-fed, location specific brush electrode, established a user defined working area.

Copper and tin films were deposited utilizing the described electrodeposition setup. These metals were chosen for their valuable properties and enticing potential for the negative electrode of the lithium ion battery. Since most past research focuses on the nano-scale version of this composite electrode, the goal of the following research is to adapt the combination into a viable negative electrode with competitive capacity values in comparison to the current commercial electrode

material, graphite, for practical applications. This is accomplished through the building of the heterogeneous composite electrode from the bottom up through separate layers of copper and tin. This theory allows for the complete control of the formation of the copper-tin alloy composition through an optimized anneal heat treatment. The design of the research allows for the intertwining of the current collector with the electrode material with excess pure copper remaining at the bottom of the film post heat treatment. This is advantageous for the lithium ion battery because of its ability to better utilize volume within the cell and eliminate 'dead' volume from additives, fillers, and a separate current collector in the current system. Combining the current collector and electrode into one piece would also generate an electrode with superior electrical conductive properties due to its inherent blending with the current collector electrochemically.

The main aspect of this research focuses on the optimization of the copper-tin alloy composition to fabricate the most competitive electrode material. In this process, many different parameters were studied. Some of these include anneal temperature and time, as well as the individual film electrochemical deposition optimization and film thicknesses. Since diffusion limitations proved to have major effects on long-term ability to produce a desired copper-tin composition, the shorter diffusion lengths throughout the film were controlled by the introduction of the stack and press anneal method. Further details of this process will be described in this paper, but in general, this process manually creates an alternating stacked film of copper and tin layers prior to heat treatment. Upon annealing the layers together,

the copper-tin alloys will be formed throughout the entire electrode because of the many interfaces within the stacked film.

Other areas of interests discussed in this research include the additions of surface coatings as well as electrolyte additives for modifications of the reactivity of the lithium alloy during cycling. As previously discussed, irreversible losses are a major issue in the cycling of lithium alloys in lithium ion batteries. Therefore it is beneficial to the electrode material if barriers can be created to minimize these losses. This can be accomplished through neutralizing the surface of the lithium alloy through coatings of Alumina or LiPON so that less active material is lost to the formation of the SEI layer. Additives in the electrolyte, such as vinyl chloride or fluorinated ethylene carbonate, can also be beneficial to the cycling of the lithium alloy due to the fact that they can reduce the chemical reactiveness of the electrolyte.

This paper will describe the optimization work and advancements of conjoining macro brush plating with the electrodeposition of copper-tin alloys. Herein, a reproducible composite film will be described that possesses areal discharge capacities above 1000mAh/cc and 2.5mAh/cm^2. These values have also been linked with low irreversible losses such as less than 15% for subsequent cycles. These characteristics have been made possible by the identified copper-tin alloys within the described optimized composition. Furthermore, a detailed explanation will be given on maintaining the film's capacity retention and cycle stability.

1.11 References

1 J. Baker. Energy Policy 36 (2008) 4368-4373.
2 K.C. Divya, J. Østergaard. Electric Power Systems Research 79 (2009) 511-520.
3 P.J. Hall, E.J. Bain. Energy Policy 36 (2008) 4352-4355.
4 S.J. Moura, J. Siegel, D.J. Siegel, H.K. Fathy, A.G. Stefanopoulou. Vehicle Power and Propulsion Conference. IEEE. (2010).
5 T. Christen, C. Ohler, Journal of Power Sources. 110 (2002) 107-116.
6 T. Christen, M.W. Carlen, Journal of Power Sources. 91 (2000) 210-216.
7 H. Ibrahim, A. Ilinca, J. Perron, Renewable & Sustainable Energy Reviews. 12 (2008) 1221-1250.
8 S. Koohi-Kamali, V.V. Tyagi, N.A. Rahim, N.L. Panwar, H. Mokhlis. Renewables and Sustainable Energy Reviews 25 (2013) 135-165.
9 http://www.electricalreview.co.uk/asset/3137/Flywheel%20Diagram%20FINAL-220.jpg
10 M.S. Whittingham. Fundamentals of Materials for Energy and Environmental Sustainability. 44 (2011) 608-623.
11 http://origin-ars.els-cdn.com/content/image/1-s2.0-S0013468611012254-gr12.jpg
12 J.R. Miller, P. Simon. The Electrochemical Society Interface Spring. (2008) 31-32.
13 R.M. Dell. Solid State Ionics 134 (2000) 139-158.
14 http://www.mpoweruk.com/images/carbonzinc.gif
15 R.J. Brodd, K.R. Bullock, R.A. Leising, R.L. Middaugh, J.R. Miller, E. Takeuchi. Journal of The Electrochemical Society 151 (2004) K1-K11.
16 R.J. Brodd. The Electrochemical Society Interface Fall. (1999) 20-23.
17 R.A. Huggins. Advanced Batteries: Materials Science Aspects. (2009)
18 R. Malini, U. Uma, T. Sheela, M. Ganesan, N.G. Renganathan. International Journal of Ionics. 15 (2009) 301-307.
19 M. Wakihara. Materials Science and Engineering. R33 (2001) 109-134.
20 J. Broadhead, H.C. Kuo. Handbook of Batteries. 3 (2002) 2.1-2.37.
21 S. Megahed, W. Ebner. Journal of Power Sources. 54 (1995) 155-162.
22 T.B. Reddy, S. Hossain. Handbook of Batteries. 3 (2002) 34.1-34.62.
23 B.B. Owens. Journal of Power Sources. 90 (2000) 2-8.
24 http://www.azonano.com/images/Article_Images/ImageForArticle_3053(1).jpg
25 G.M. Ehrlich. Handbook of Batteries. 3 (2002) 35.1-35.94.
26 A.K. Padhi, K.S. Nanjundaswamy, J.B. Goodenough, Journal of the Electrochemical Society. 144. (1997) 1188-1194.
27 A. Ritchie, W. Howard, Journal of Power Sources. 162 (2006) 809-812.
28 W.J. Zhang. Journal of Power Sources. 196 (2011) 13-24.
29 L.F. Nazar, O. Crosnier, Anodes and Composite Anodes: An Overview. 4 (2003) 112-127.
30 R.A. Huggins, Solid State Ionics. 113-115 (1998) 57-67.

31 W.-J. Zhang. Journal of Power Sources. 196 (2011). 877-885.
32 C. Liang, M. Gao, H. Pan, Y. Liu, M. Yan, Journal of Alloys and Compounds. 575 (2013) 246-256.
33 R.A. Huggins, Journal of Power Sources. 81-82 (1999) 13-19.
34 J. Yang, J.I. Wang. Encyclopedia of Electrochemical Power Sources. (2009) 225-236.
35 M. Winter, J.O. Besenhard, Electrochimica Acta. 45 (1999) 31-50.
36 L. Simonin, U. Lafont, E.M. Kelder, Journal of Power Sources. 180 (2008) 859-863.
37 B. Scrosati, J. Garche. Journal of Power Sources. 195 (2010) 2419-2430.
38 M. Yoshio, T. Tsumura, N. Dimov, Journal of Power Sources. 146 (2005) 10-14.
39 Y. Hu, X. Zhao, Z. Suo, Journal of Materials Research. 25 (2010) 1007-1010.
40 S.W. Lee, M.T. McDowell, L.A. Berla, W.D. Nix, Y. Cui, PNAS. 109 (2009) 4080-2085.
41 A. Mukhopadhyay, B.W. Sheldon, Progress in Materials Science. 63 (2014) 58-116.
42 O. Mao, R.L. Turner, I.A. Courtney, B.D. Fredericksen, M.I. Buckett, L.J. Krause, J.R. Dahn, Electrochemical and Solid State Letter. 2 (1999) 3-5.
43 O. Mao, R.A. Dunlap, J.R. Dahn, Journal of the Electrochemical Society. 2 (1999) 405-413.
44 J.S. Smart, P.T. Gilbert, Copper, The Science and Technology of the Metal, Its Alloys and Compounds. 17-18 (1954) 360-409.
45 K.D. Kepler, J.T. Vaughey, M.M. Thackeray, Journal of Power Sources. 81-82 (1999) 383-387.
46 F. Ke, L. Huang, J. Cai, S. Sun. Electrochimica Acta. 52 (2007) 6741-6747.
47 S.D. Beattie, J.R. Dahn, Journal of the Electrochemical Society. 150 (2003) A894-A898.
48 J.S. Thorne, J.R. Dahn, M.N. Obrovac, R.A. Dunlap. Journal of Power Sources. 216. (2012) 139-144.
49 I.A. Courtney, J.R. Dahn, Journal of the Electrochemical Society. 144 (1997) 2943-2948.
50 U.G. Nwokeke, R.Alcantara, J.L. Tirado, E. Zhecheva, Journal of Power Sources. 196 (2011) 6768-6771.
51 P. Verma, P. Marie, P. Novák, Electrochimica Acta. 55 (2010) 6332-6341.
52 V.A. Agubra, J.W. Fergus, Journal of Power Sources. 268. (2014) 153-162.
53 L. Chen, K. Wang, X. Xie, J. Xie, Journal of Power Sources. 174 (2007) 538-543.
54 H.A. Wilhelm, C. Marino, A. Darwiche, L. Monconduit, B. Lestriez, Electrochemistry Communications. 24 (2012) 89-92.
55 M. Schlesinger. Electrochemistry Encyclopedia. (2002).
56 M. Paunovic, M. Schlesinger, D.D. Snyder, Modern Electroplating. 5 (2010) 1-32.
57 L. Trahey, J.T. Vaughey, H.H. Kung, M.M. Thackeray, Journal of the Electrochemical Society. 156, 5 (2009) A385-A389.

2 Experimental

2.1 Materials Fabrication

2.1.1 Brush Plating Setup

The two main components for our brush plating electrodeposition system consisted of the modified SICFO Traversing Arm and Process Power Pack (20V/60A). Unique to our design, this process had a simulated mechanical "pulse" with the movement of both the working and counter electrodes during the plating process. Figure 2-1 provides an image of the traversing arm working zone. To create this pulse, a sinusoidal movement of the counter electrode in the 'y' direction and motor driven left/right movement of a titanium substrate attached to the base area in the 'x' direction were executed simultaneously as depicted in Figure 2-2. The counter electrode, a platinum coated niobium ½" diameter electrode, was confined to parallel repetitions above the substrate at

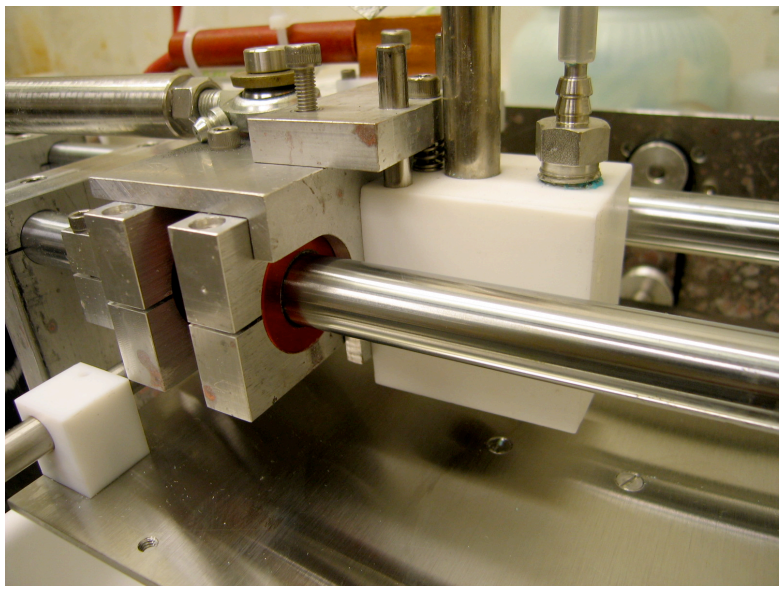

Figure 2-1 Traversing arm brush plating system setup with stage for working electrode attachment and counter electrode.

34rpm based on the traversing arm length of 45.72cm and diameter 15.25cm. The titanium plate (17.78cm x 17.78cm x 0.3175cm) was motor driven at about 0.148mm/sec. Additionally, the working area was confined to a meniscus of the plating solution with an approximate 7.1mm gap separating the insulated pad of the counter electrode from the working electrode surface. The Masterflex Peristaltic Pump regulated the solution flow through L/S 16 tubing (~3.1mm dia) at about 0.8-1.0mL/min. Figure 2-3 depicts the cross-section of the counter electrode holder with the solution flow from the reservoir and pump to create a meniscus on the surface of the titanium substrate. With a slight tilt of the entire plating setup, all excess solution was easily collected in the basin under the base working area. The repetitive electrode movements with the controlled solution working area helped to create a macro scale film with user-defined morphology. Several different insulating

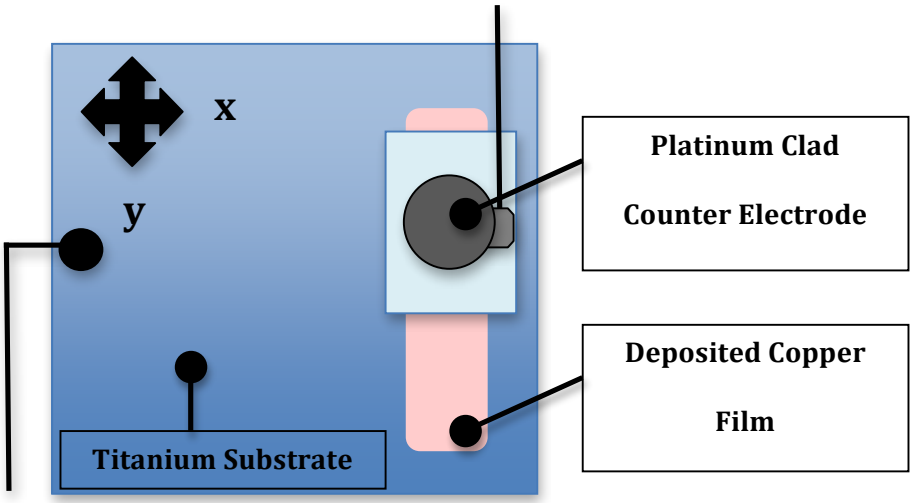

Figure 2-2 Schematic of the directional movement during brush plating electrodeposition. The titanium working electrode moves back and forth in the 'x' direction while the platinum clad counter electrode simultaneously moves in the 'y' direction.

pad materials and meniscus heights were tested. The titanium plate was pretreated with sandpaper Grade 180 and scuffed with Scotch-Brite to establish adherence of the deposited films.

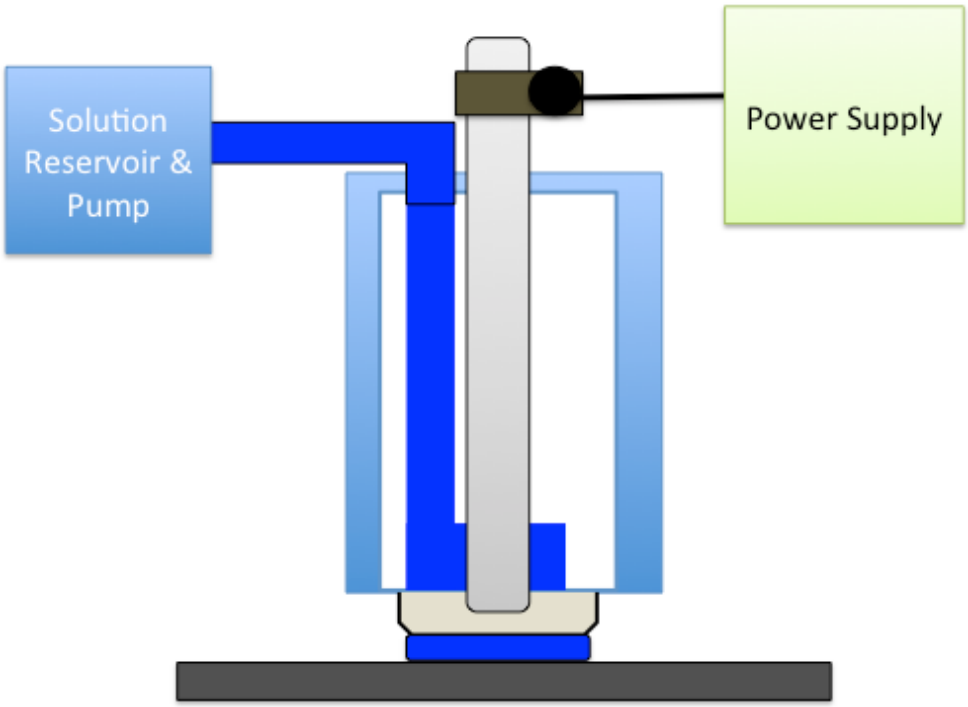

Figure 2-3 Schematic of the solution meniscus formation with flow through the teflon counter electrode holder from the solution reservoir via a peristaltic pump.

Following all fabrication processes, the titanium plate was removed from the base area and rinsed. The initial rinse step consisted of 200mL of de-ionized water to remove any additional salts and additives from the deposited film. This bath was followed by an Acetone and Methanol rinse to remove any residual water from the surface. The substrate was dried at 70°C for 5-10min before additional plating or characterization.

2.1.2 Plating Conditions For Copper & Tin Layers

Both plating solutions were from SIFCO Applied Surface Concepts: Copper Acid Code 2050/5250 and Tin Code 2093. The copper solution maintained a working pH of 0.350 at 20°C while the tin solution had a pH of 0.613 at 20°C. All operations were completed in ambient conditions.

The copper film was consistently applied using the SIFCO Process Power Pack (20V/60A) under constant galvanostatic conditions at 6.5-8.0mA/cm^2. The tin film was fabricated utilizing the EG&G Princeton Applied Research Potentiostatic/Galvanostatic Model 273A in conjunction with CorrWare electrochemical software for constant galvanostatic (500-700μA/cm^2), pulsed potentiostatic (60mV/cm^2) or pulsed galvanostatic (1.2mA/cm^2). Table 2-1 describes the copper-tin film thicknesses fabricated according to their apparent deposition conditions.

Table 2-1 Described plating conditions and film thicknesses for fabricated electrodeposited copper-tin films.

Film	Copper	Tin	Conditions
1.	3μm	5.68μm	Constant
2.	10μm	17μm	Constant
3.	10μm	8μm	Constant
4.	10μm	8μm	Pulsed Potential (5sec)
5.	10μm	8μm	Pulsed Potential (0.1sec)
6.	10μm	8μm	Pulsed Current (0.1sec)
7.	3μm	6.5μm	Constant
8.	3μm	7.5μm	Constant

2.1.3 Heat Treatment of Single Bilayer Copper-Tin Films

Following fabrication, the copper-tin films were annealed in a tube furnace under flowing Argon. Table 2-2 describes the heat treatment protocols for all films annealed in an alumina boat for this process. All single copper-tin bilayer films that were annealed under pressure followed the described heat treatment protocol of the triple stacked bilayer films.

Table 2-2 Heat treatment protocols for copper-tin bilayer films.

Temperature (°C)	150	200	225	275	275	325
Time (h)	8	4	8	4	24	4

2.1.4 Triple Stacked Bilayer Copper-Tin Film Heat Treatment

Three bimetallic copper-tin films were stacked and pressed (8in.lbs/ft) between stainless steel plates flanked by Teflon sheets. The films were stacked alternating metals so that the bottom layer of the film was copper and the top most layer was tin. The stacked films were heat treated in a tube furnace for approximately 4h under argon unless otherwise stated. Post anneal, the tube furnace was cooled back to room temperature before disassembly and removal of films.

2.1.5 Post Anneal Surface Coatings: LiPON & Alumina

The fabrication of the LiPON and alumina surface coatings was completed utilizing high vacuum techniques such as physical vapor (PVD) and chemical vapor deposition (CVD). The LiPON coatings were deposited via the PVD technique of sputter deposition. In sputter deposition, under high vacuum conditions, a target

material (desirable deposited material) and the substrate are polarized so that when the target is bombarded with ionized plasma (inert gas), the target material is exfoliated and deposited on the substrate [58]. The CVD process of Atomic Layer Deposition (ALD) was utilized to fabricate the alumnia coatings of the Cu-Sn films. This high vacuum technique employs heated precursor gases and vapors that are chemisorbed or surface reacted with the substrate to create the coating of the desired material [59]. Both the surface coatings from sputter deposition and ALD can produce thin films in the low nanometer range, with the ALD process reaching down to 1angstrom.

Additional surface coatings were applied to the heat-treated copper-tin films to alter the electrochemical capabilities during cycling. The solid electrolyte coating, LiPON (lithium phosphorous oxynitride) was fabricated utilizing the Kurdex system ($2^{x}10^{-3}$Pa) from LiPON target precursor. For coating preparations, the copper-tin films were masked with glass slides taped to the bottom surfaces to ensure flat, smooth coatings on the top surface and protect the back surface from deposition. Film thicknesses were varied between 20nm and 250nm. Following deposition, the films were characterized and electrochemically tested in half-cells.

Alumina coatings were also investigated as a surface coating option utilizing ALD (Atomic Layer Deposition). Precursors of H_2O vapor and TMA (Trimethyl Aluminum) vapor were applied at 100°C. Glass slides masked the bottom side of the films from the coatings. Coating thicknesses included 5nm and 15nm. Similarly, the films were electrochemically tested for their effects on cycling.

2.2 Physical Characterization

2.2.1 FTIR Analysis of Insulating Pad

Fourier Transform Infrared spectroscopy utilizes infrared light for the examination and identification of organic materials via the excitation of their unique vibrational bonds. In this technique an interferogram composed of all infrared frequencies is guided through the sample at which point certain radiation will be absorbed or transmitted due to the specific bonding in the material [60]. This produces a unique frequency spectrum for all compounds that can be used for materials identification, purity analysis of a sample, and/or component percentage recognition in a mixture.

Several insulating pad materials were investigated for effects on deposition film morphology. Pad material identification was executed utilizing the Mid-IR KBr filter of the Thermo Scientific FTIR Nicolet 6700. 250scans of each material were used to show the organic peaks from 4000-400cm^{-1} wavelengths. The results of the FTIR analysis in conjunction with the surface analysis of the profilometer were used to conclude which material yielded the best results.

2.2.2 Profilometer Analysis

The mechanical characterization technique utilizing measureable contact to investigate the surface roughness of a material is profilometry. The use of contact profilometry employs a cantilever stylus profiler moved over the surface of the material to measure the high and low points of the surface topography [61]. The

average of these measurements defines the surface roughness of the material. The stylus tip radius can range from 20nm to 25μm [62]. Minimal force for stylus contact is desired to preserve the surface texture of the material but sufficient force is needed to obtain detail. To increase the resolution of surface definition, smaller tip radii are desirable. More advanced measurements can be investigated to produce 3D surface topography with multiple scans.

Following deposition of each metal film, the Veeco Detak 150 Profilometer was utilized to investigate the surface roughness. The cantilever was applied with 3mg for 400sec over 6000μm with resolution 0.05μm/sample. Analysis of the central area of the film gave a general roughness evaluation. Additionally, a 3D mapping of the surface (3000μm x 1000μm) with 10sec scans, 1μm x-y resolution, and 2mg-applied force gave a topographic visualization of the surface.

2.2.3 XRD Analysis

X-ray diffraction analysis is the characterization technique used to study the crystalline structure of materials. Incident x-rays are resultant from an electron beam striking a metal target (typically copper or molybdenum) causing the ionization of K-shell electrons and the dropping of electrons from the L- and M-shells [63]. In order for the electrons from these higher levels to drop into the K-shell, energy is emitting from the material via x-rays. These x-rays (incident beam) can then be focused on a crystalline material of interest at which point the x-rays will diffract in accordance to the planes of atoms in the material. The collected diffracted x-rays form a specific x-ray diffraction pattern. All crystalline materials

have unique x-ray diffraction patterns that are characteristic to their spacing of atoms between planes (d-spacing). The relationship of the x-rays and the d-spacing of a material can be explained by Bragg's Law seen in Equation 2.1:

$$n\lambda = 2d\sin\theta \qquad (2.1)$$

where n is the integer for the order of diffraction (most cases n=1), λ is the

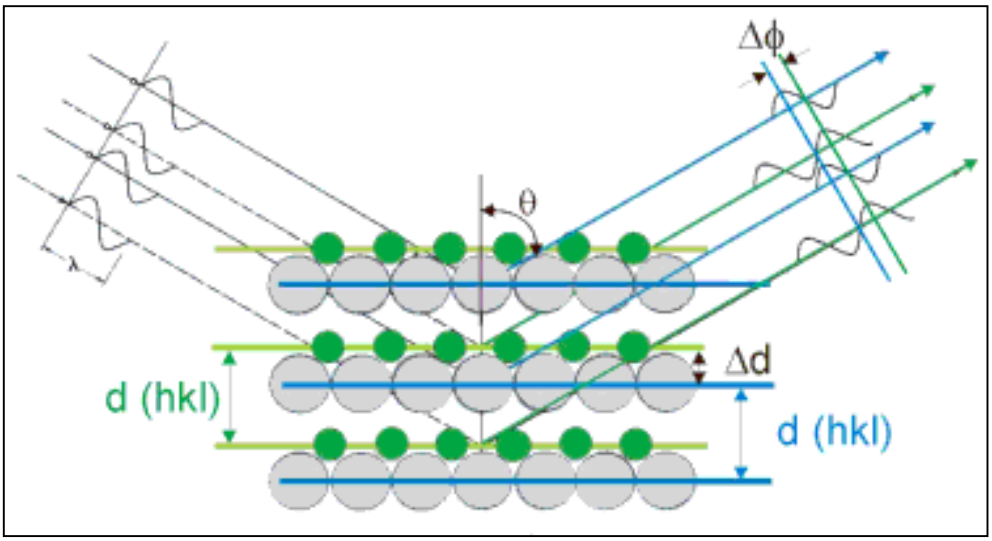

Figure 2-4 Schematic representation of Bragg's Law.

wavelength of the x-ray, θ is the incident angle of the x-ray, and d is the spacing between two planes of the crystal [64]. Bragg's law can only be satisfied for a material when constructive interference of the x-rays at a certain angle produces the diffracted x-rays leading to the x-ray spectra [63,64]. Figure 2-4 shows a schematic representation of x-ray diffraction with the satisfaction of Bragg's Law [65]. Otherwise the x-rays produce destructive interference and no obtainable information for x-ray analysis. This useful technique can be used to identify: crystal structure, phase identity, phase purity, lattice parameters, percent phase composition, and crystallinity.

Individual phase identification comprised of x-ray diffraction (Bruker D8 Advance) using monochromatic Cu K_α with the Bragg-Brentano setup. The bilayer and triple stacked films were analyzed from both the top and bottom surfaces to obtain more precise investigation of the overall composition that may be distorted due to x-ray penetration limits. The x-ray penetration depth was calculated using Equation 2.2:

$$\tau = \sin\alpha \div \mu \tag{2.2}$$

where τ is the penetration depth, α is the x-ray angle of incidence, and μ is the linear absorption coefficient.

2.2.4 DSC Analysis

Differential scanning calorimetry studies the relationship of heat flow for material transitions as a function of time and temperature [66]. This technique is unique because of its ability to measure the enthalpy associated with these transitions. In this process the material of interest and a reference sample are heated in a thermoelectric disk in a furnace. Due to the heat capacity of the material, a measureable temperature difference between the material and reference will occur.

The melting temperature of the tin from the Cu-Sn film was established utilizing differential scanning calorimetric analysis with the DSC Q10. Non-annealed samples of the electrodeposited Cu-Sn films were heated at 5°C/min to 300°C under Argon unless otherwise specified. This analysis in combination with FESEM EDS was

used to study the morphological effects of heat treatment at temperatures above the melting point of tin without applied controlled pressure.

2.2.5 Pycnometer Density Analysis

Gas pycnometry is utilized to study the true volume and true density of a material (powder or solid). This is accomplished with the analysis of pressure changes in an enclosed chamber of known volume containing the material of interest. An inert gas is flowed into the chamber filling all accessible space including exterior pores of the material of interest [67].

True density was established by He pycnometry (Micromeritics Accu Pyc II 1340) to identify each film's copper:tin molar ratio and composite film densities. The composite density after thermal anneal was calculated based on the film's total weight and measured volume by pycnometery. In addition, electrodeposited individual films of pure copper and tin were analyzed to establish a baseline for densities of each metal. These values were compared to the theoretical values for the pure and intermetallic phases to evaluate our joint deposition and anneal process.

2.2.6 FESEM/Cross Ion Polished Analysis

Field Emission Scanning Electron Microscopy (FESEM) is the characterization technique used for high magnification surface imaging and feature analysis. The microscope employs the use of an electron beam to excite the secondary electrons of the material's surface, which are ejected at characteristic angles and velocities that can be recorded to produce the scan-image [68]. This

technique can be used to image surface details down to 1 nanometer. Energy Dispersive Spectroscopy (EDS), supplementary electron microscopy, uses backscattered electrons to achieve x-ray spectrum based on compositional contrast due to different atomic number elements [69]. Therefore the combination of FESEM and EDS analysis can be used for full examination of the materials surface structure.

Film morphology and elemental distribution was determined with the Zeiss FESEM (Field Emission Scanning Electron Microscopy) to analyze the diffusivity of the pure electrodeposited metal films. All samples were cross-sectional ion polished at 5kV for 5h under flowing Argon. The triple stacked bilayer films were supplemented with a silver epoxy coating for additional support during polishing. EDS (Energy Dispersive X-ray Spectrometer) spectra and maps of the cross-sectional films revealed the elemental mixture of the pure deposited layers after thermal anneal and determined the composite molar ratio for comparison with results from the pycnometer.

2.3 Electrochemical Characterization

2.3.1 Standard Half Cells with Galvanostatic Protocols

Electrochemical analysis of the copper-tin films was accomplished using 316 stainless steel coin cells (Hohsen Corp.) with the described electrolytes (BASF Selectilyte Sample Series A5) in Table 2-3. All coin cells were assembled with an argon press in a helium filled glove box (Mbraun) kept at 2.5mbar and contaminates less than 0.3ppm H_2O and less than 0.1ppm O_2. Half-cells were fabricated with ½”

electrode film disks versus lithium and cycled utilizing a battery cycler (Arbin) under galvanostatic conditions. Table 2-4 describes some of the cycling protocols used in the experiments.

Table 2-3 Electrochemically tested electrolyte combinations for the Cu-Sn half-cells

Electrolyte	Formula
Standard	1M LiPF6 EC:DMC (1:1)
Vinyl Carbonate Additive	1M LiPF6 EC:DMC 5% VC
	1M LiPF6 EC:DMC 10% VC
Fluoro Ethylene Carbonate Additive	1M LiPF6 EC:DMC 5% FEC
	1M LiPF6 EC:DMC 10% FEC
EMC	1M LiPF6 EC:EMC (30%:70%)

Table 2-4 Cycling protocols utilized for the Cu-Sn film half-cells.

Protocol	Cycling Range	Applied Current
1	0.01-2V	15mA/g (First 1.5 Cycles) 30mA/g (All Other Cycles)
2	0.01-2V	30mA/g (All Cycles)
3	0.01-2V	[A] 15mA/g (first 1.5Cycles) [B] 30mA/g (15 Cycles) [C]15mA/g (1Cycle) *Repeat B & C For 1000 Cycles*
4	0.01-1.3V	15mA/g (First 1.5 Cycles) 30mA/g (All Other Cycles)

Additional examination included modifications to the standard cycling protocols to include potentiostatic holds or cycling capacity cutoffs. Table 2-5 defines these modified protocols.

Table 2-5 Protocol modifications used for further electrochemical analysis for the Cu-Sn film half-cells

Protocol Assessment	Cycling Range	Applied Current
Potentiostatic Hold	0.01-1.3V	30mA/g Lithiation Hold to 15mA/g 30mA/g Delithiation
Capacity Cutoff	0.01-1.3V	30mA/g (All Cycles) Limit to 3.0mAh/cm^2

2.3.2 Standard Full Cell vs LCO (3mA/g)

Additional electrochemical evaluation was conducted in lithium ion cells for comparison against MCMB 25-28 graphite. Aluminum coin cells (Hoshen Corp.) with 1M $LiPF_6$ EC:DMC electrolyte (BASF Selectilyte Sample Series A5) were utilized with ½" disks of $LiCoO_2$ 3mAh/cm^2 versus the deposited copper-tin films. The full cells were cycled from 2.5-4.15V for 1000 cycles at 15mA/g ($LiCoO_2$).

2.4 References

58 http://users.wfu.edu/ucerkb/Nan242/L07-Sputtering_a.pdf
59 http://www.chembio.uoguelph.ca/educmat/chm753/Third%20Class/maryam.ppt
60 http://mmrc.caltech.edu/FTIR/FTIRintro.pdf
61 http://www.mecheng.iisc.ernet.in/~bobji/funtri/Assign_2012/PROFILOMETER.ppt
62 http://www.veeco.com/pdfs/database_pdfs/B509%20Dektak150%20_281.pdf
63 H. zur Loye, http://www.chem.sc.edu/faculty/zurloye/xrdtutorial_2013.pdf
64 http://web.pdx.edu/~pmoeck/phy381/Topic5a-XRD.pdf
65 http://www.xtal.iqfr.csic.es/Cristalografia/archivos_05/bragg2.gif
66 P. Gill, T.T. Moghadam, B. Ranjbar, Journal of Biomolecular Techniques. 21 (2010) 167-193.
67 http://www.pmiapp.com/ProductPages/brochures/Gas_Pycnometer.pdf
68 http://www.vcbio.science.ru.nl/public/pdf/fesem_info_eng.pdf
69 http://www.charfac.umn.edu/instruments/eds_on_sem_primer.pdf

3 Results & Discussions

There are several important parameters that affect the morphology and properties of the electrodeposited films. The initial sections of this chapter will focus on the optimization of such factors during the deposition process to produce coherent copper and tin films, while the final sections will concentrate on the enhancement of the architectural design and electrochemical properties.

3.1 Brush Plating Deposition: Optimization

Guidelines for required amp-hours for desired film thickness were administered from SIFCO Applied Surface Concepts, fabricators of the electrodeposition plating solutions, counter electrode, traversing arm setup, and power pack. The basic formula for this determination is seen in Equation 3.1:

$$\textbf{Amp}\cdot\textbf{Hour} = \textbf{F} \times \textbf{A} \times \textbf{T} \qquad \textbf{(3.1)}$$

where F is the solution factor provided by SIFCO, A is the working surface area in squared centimeters, and T is the desired thickness of the deposited film in microns [70]. The solution factor takes into account that solution additives (introduced to improve film deposition appearance and ease in plating) cause side reactions to occur during electrodeposition, decreasing the columbic efficiency to be less than 100% [71]. However, due to alterations and additions to the setup to create a mechanical pulse with meniscus brush deposition, some modifications were needed to further optimize the deposition of both the copper and tin film layers.

3.1.1 Optimization of Plating Parameters for Copper Films

Table 3-1. Technical guidelines for the electrodeposition of copper films.

Technical Data Sheet For Copper Acid Code 2050/5250	
Factor	0.0008
Average Current Density	0.46 amp/cm
Maximum Current Density	0.93 amp/cm
Voltage Range	3 to 12
Maximum Recommended Usage	30 Amp-hr per liter
Plating Rate	575 μm/hr
Metal Content	60 g/l

The general guidelines provided by SIFCO for the Copper Acid Code 2050/5250 solution are included in Table 3-1 [70]. According to this data, utilizing the provided factor value for copper in Equation 3.1 should allow for the calculated amp-hours needed for such experimental thicknesses (3microns and 10microns). However, after several trials, it was determined that the simultaneous movement of the counter and working electrodes established much thicker films than anticipated. It was concluded that the dual movement of the counter and working electrodes in partner with the constant flow of the plating solution decreased the Nernst diffusion layer typically present during bath solution electrodeposition, so that it had minimal effect on the coulombic efficiency [71]. Therefore there were limited issues with concentration polarization.

The calculated amp-hour value from Equation 3.1 was therefore reduced to 54.5%. Support for this adjustment is seen in Figure 3.1 and Figure 3.2, which show the thickness measurement mapping for a copper film. The targeted thickness of this film was 10micron. The central location of the film (highlighted in blue on the

schematic) is the area of importance. The outer region of the deposited film was regarded as unviable due to the drastic variations in the film thickness from the sinusoidal oscillations of the counter electrode attached to the traversing arm. The combination of Figure 3-1 and Figure 3-2 supports the adjustment in calculation of amp-hours for the desired film thickness. Further confirmation was seen for reproducible films of 3micron thickness.

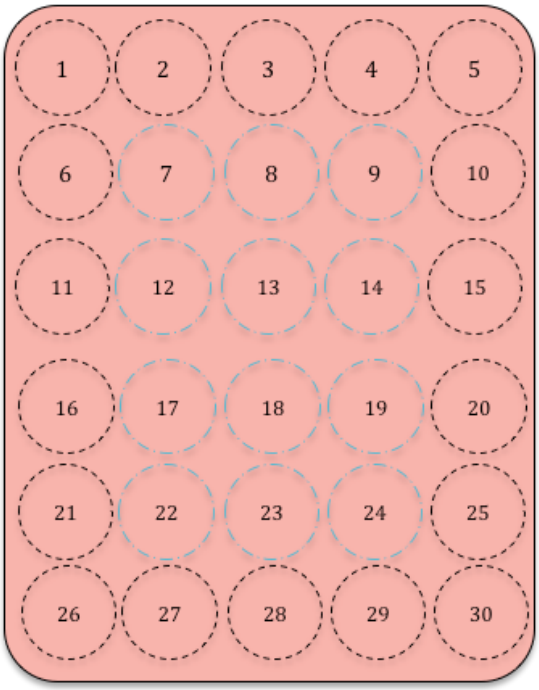

Figure 3-1 Schematic of location mapping for thickness measurements of a 10micron copper film. The highlighted middle region shows the area of importance.

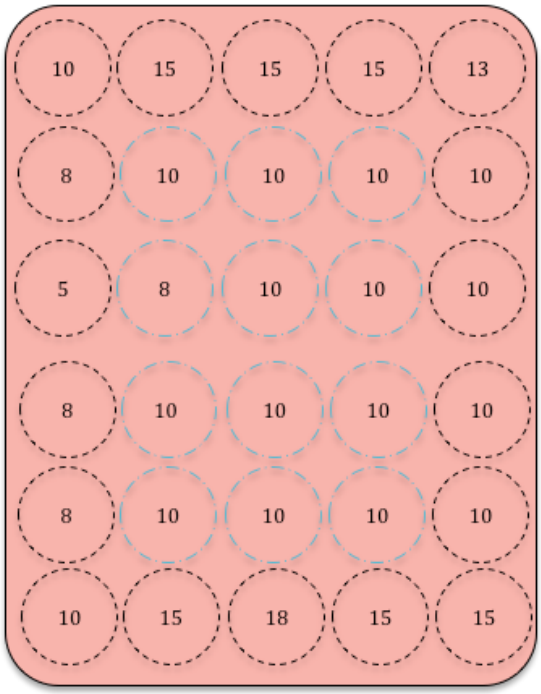

Figure 3-2 Schematic of the film thickness measurements associated with each location of the 10micron copper film. The middle highlighted section confirms the achieved targeted thickness.

Table 3-2 Optimized plating conditions for copper film deposition.

Experimentally Determined Target Parameters For Copper Films	
Counter electrode (traversing arm) speed	34rpm
Working electrode (base stage) speed	0.148mm/sec
Applied Electrical Current	6.5-8.0mA/cm^2

Movement of the counter and working electrodes also played a role in the physical properties of the films. The ideal settings (electrode speeds and electrical conditions) for copper deposition are reviewed in Table 3-2. Experimental results showed that when the counter electrode moved at too slow of a rate, 'burning' occurred during plating, producing a dark powdery deposit that was less adherent to the substrate/previous layer. Burning occurs because the applied current density exceeds the requirements for the proper electrochemical reaction to occur to form strong

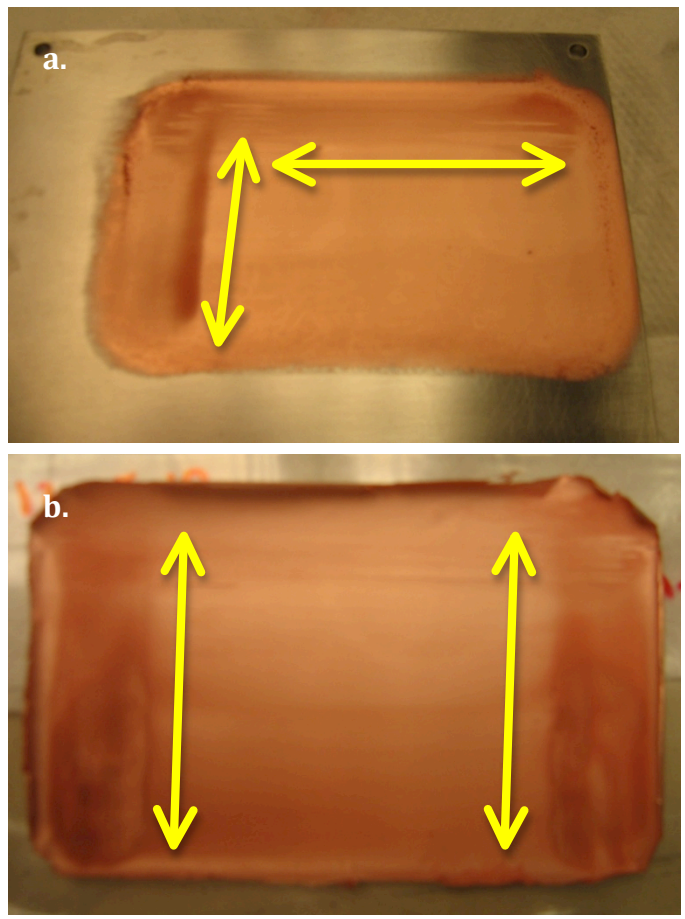

Figure 3-3 Examples of deposition burning for a copper film. a) The arrows highlight burning of the film in both directions during plating. b) The arrows highlight burning of the film on both end areas of the film signifying the oscillation pauses too long in change of direction.

covalent bonding between the deposited film layers. The extreme over-potential causes the instantaneous reduction of the metal from the solution held on the substrate by surface forces such as ionic bonding and van der Waals forces [70,71]. Examples of this form of deposit are seen Figure 3-3. When the speeds of the electrodes moved too quickly, more plating solution and time were required to create a cohesive film. Ideally, it was determined that the oscillation of the traversing arm at 34rpm moved at the best pace for the quickest turnover in direction. Speeds were examined between 28-55rpm. Similarly, the current range of 6.5-8.0 mA/cm^2 helped in producing a bright matte copper colored film as seen in Figure 3-4, which did not experience any loose powdery deposition. The best results were produced from utilizing a current density of 7.13 mA/cm^2.

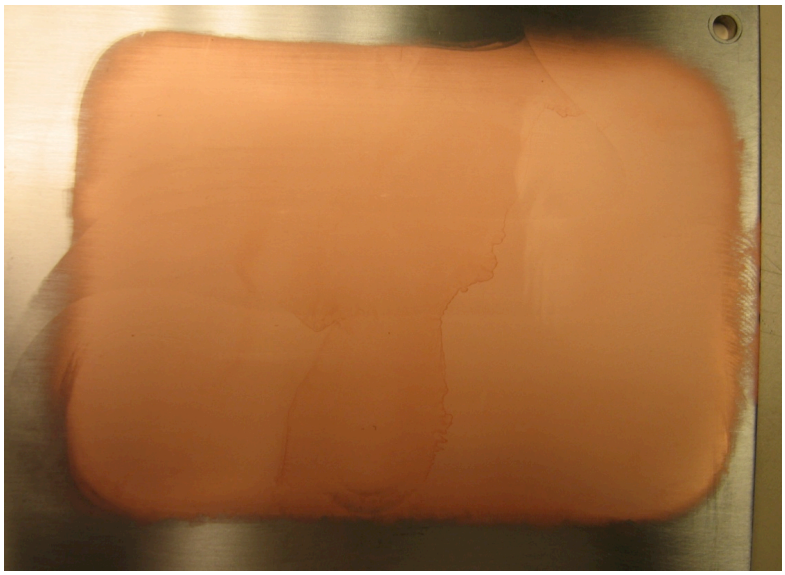

Figure 3-4 Example of a well-plated copper film under the correct deposition parameters.

3.1.2 Plating Optimization For Tin Films

Table 3-3. Technical guidelines for the electrodeposition of tin films.

Technical Data Sheet For Tin Code 2093	
Factor	0.00034
Average Current Density	0.46 amp/cm
Maximum Current Density	0.93 amp/cm
Voltage Range	4 to 15
Maximum Recommended Usage	20 Amp-hr per liter
Plating Rate	175 μm/hr
Metal Content	80 g/l

Table 3-3 describes the guidelines for the Tin Code 2093 plating solution from SIFCO Applied Surface Concepts [70]. Similar to the adjustments for the copper film deposition, the tin calculations required manipulation after experimental attempts proved an increased coulombic efficiency from the theoretical calculations with Equation 3.1. The estimated amp-hours was reduced to 26.17% for the approximate desired tin deposition. The required speeds and electrical current are reviewed in Table 3-4. These conditions helped to achieve a light gray, matte film as seen in Figure 3-5.

Table 3-4. Deposition conditions for good tin-plating deposition.

Experimentally Determined Targeted Parameters For Tin Film Deposition	
Counter electrode (Traversing arm) speed	34rpm
Working electrode (base stage) speed	0.148 mm/sec
Applied Electrical Current	500-700μA/cm^2

Figure 3-5 Example of a well-plated tin deposition from the utilized conditions.

3.1.3 Substrate Optimization

The ideal substrate for the production of freestanding electrodeposited copper-tin films comprised of a balance between bonding of the film with the surface of the substrate and liftoff capabilities for easy removal. It was important that no true electrochemical bond was formed between the metal substrate and the deposited film. However, it was desirable to fabricate a cohesive film void of cavities [71]. The substrate employed for the fabrication of freestanding deposited films was a smooth titanium plate. Titanium was chosen because of its chemical inertness to the highly acidic plating solutions and its mediocre bonding strength with copper. Copper-titanium alloys do exist according to the phase diagram seen in Figure 3-6.

However, these alloy phases are not stable below 500°C and therefore no chemical transformation takes place between the titanium substrate and copper deposition during plating. The bond between the titanium and copper is strictly superficial and

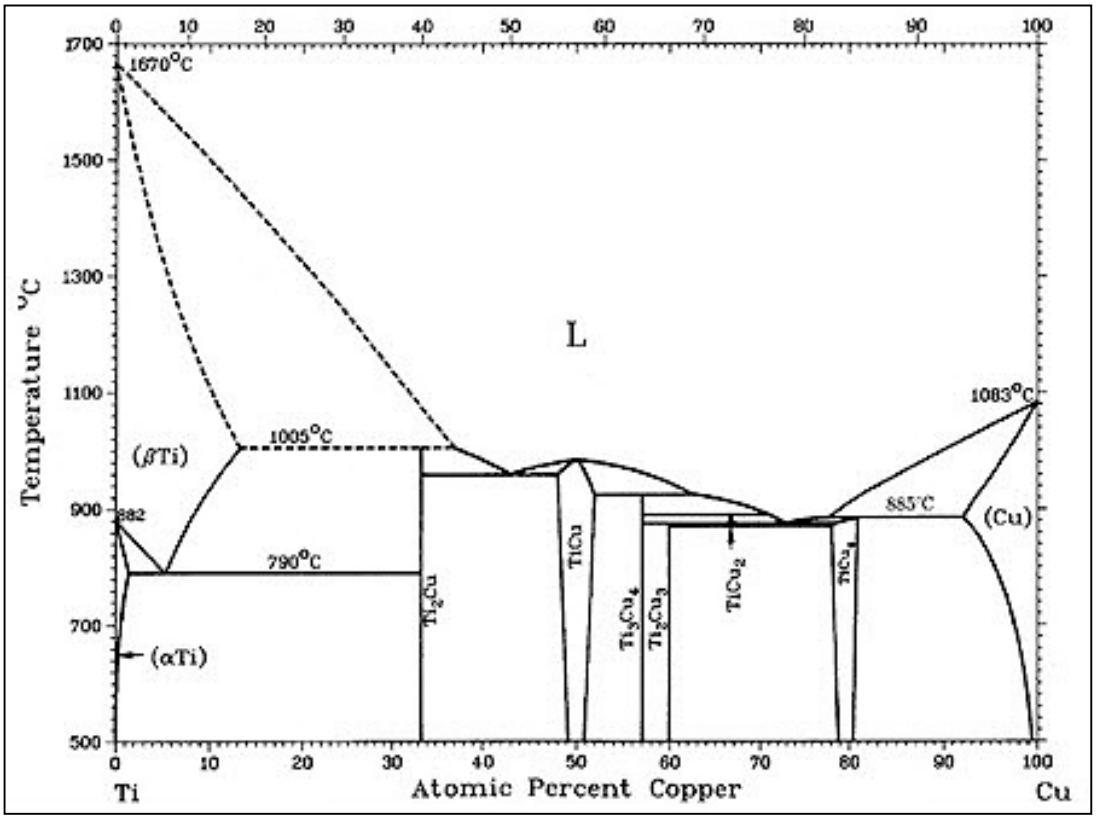

Figure 3-6 Phase diagram for titanium-copper.

controlled by van der Waals forces.

Film adherence was improved by implementing the pretreatment of the titanium surface with sandpaper (grit 180) and a Scotch Brite pad. Table 3-5 provides a comparison of the roughness measurements for the titanium plate determined by profilometry. The fine grit sandpaper was directionally utilized to polish the titanium metal plate surface by application in the same corresponding direction as the counter electrode movement. After sufficiently polishing the surface, the Scotch Brite pad, a scouring material, was employed to provide

roughening of the surface. Initial treatment was applied in small circular motions on the entire surface of the plate to increase the variability of surface roughness. This action was followed by soft-applied directional abrasions in the corresponding direction of the counter electrode movement. These steps are schematically shown in Figure 3-7. Both steps of the surface preparation were found to be necessary to provide a sufficient balance between adherence and detachability of the deposited films from the metal plate surface. The directionality in surface pretreatments was confirmed as significant during removal of the deposited films from the titanium plate. Film depositions that proceeded directional pretreatment perpendicular to the counter electrode movement, showed signs of increased adherence to the metal plate and were unable to be removed easily in one piece. This was not the case for films deposited on the titanium plate with parallel surface pretreatments. Similarly, it was found that the use of the Scotch Brite pad only in the parallel direction during roughening did not provide enough roughness for adhesion and cohesive depositions did not occur as seen in Figure 3-8, which shows an inhomogenous deposition.

Table 3-5 Profilometer measurements of the average roughness affected by additional pretreatment.

Pretreatment Steps	Average Roughness (R_a)
Titanium Plate	228nm
With Sandpaper	287nm
With Scotch Brite	443nm

Strictly utilizing perpendicular polishing/roughening during pretreatment created films with strong adhesion to the titanium substrate with issues during removal.

Therefore the additional circular roughening procedure between parallel directional polishing and roughening was added to increase the surface irregularity to promote a balanced adhesion with the titanium substrate.

Following these pretreatment steps the substrate was thoroughly cleaned and rinsed with acetone and methanol to remove any debris from the surface. The

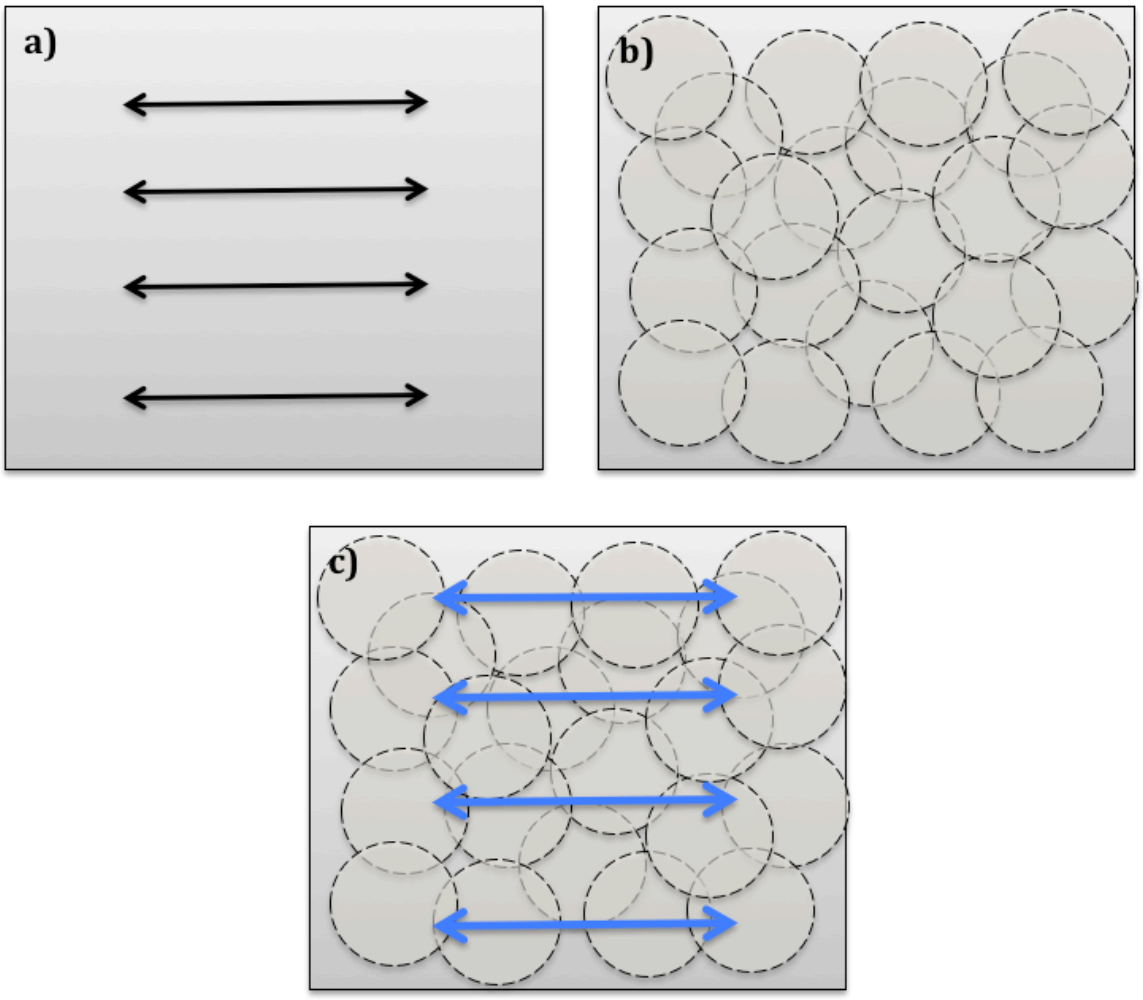

Figure 3-7 Surface polish and abrasion pretreatment description for metal substrate. a) Surface polishing with sandpaper (grit 180) directionally applied to titanium plate. b) Scouring pad (Scotch Brite) roughened surface of substrate in circular motion to increase variations in surface morphology for better adhesion. c) Scouring pad applied directionally (counter electrode movement direction) to slightly decrease the adhesion properties to increase liftoff capabilities.

substrate was dried in a 70°C oven for 5min before beginning film deposition.

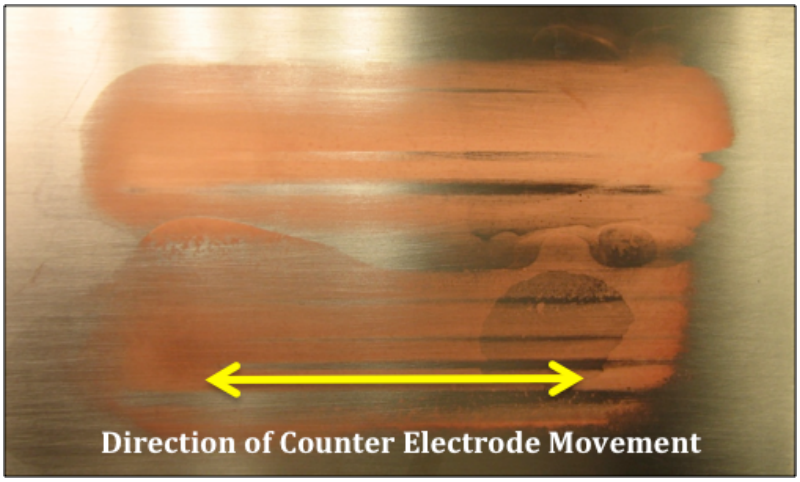

Figure 3-8 Observed inhomogeneous deposition of copper film due to low roughness in surface morphology of titanium substrate. Pretreatment of surface included only parallel directional roughening.

3.1.4 Insulating Pad Optimization

Another aspect that affected the morphology and optimization of the electrodeposited films was the insulating material separating the counter and working electrodes. This layer's responsibilities included allowance of proper flow of the plating solution to form the meniscus and morphological formation of the deposition layers. The goal of our design was the utilization of an insulating membrane that: 1) had minimal effect on the plating solution flow, minimizing the increase in solution concentration polarization 2) fabricated homogeneous surface morphology in deposited films. Several materials were analyzed in the optimization of the meniscus brush plating setup as described in Table 3-6. Each of these materials presented different characteristics due to their variations in texture. The cotton batting, cotton sleeving, and white tuff wrap material were all manufactured

insulating pad materials from SFICO Applied Surface Concepts. The towel and cloth material were simply common absorbent fabrics. Each of the pad materials was fitted in the designed holder (Figure 3-9) and experimentally tested under similar deposition parameters for direct comparison: electrode speeds, applied potentials,

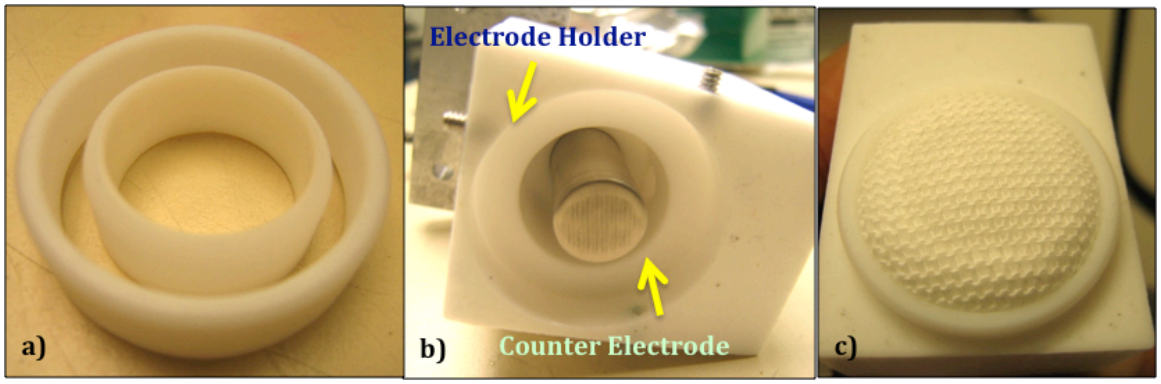

Figure 3-9 Insulating pad material holder design. a) Teflon ring-set designed to hold pad material taut in counter electrode holder. b) Teflon counter electrode holder has cavity to secure ring-set during deposition. c) Example of assembled pad holder with counter electrode holder (cotton batting & sleeving).

amp-hours passed for copper and tin depositions. The visual film results and qualitative FTIR and profilometer scans were utilized to determine the optimal material for producing the freestanding copper-tin films described throughout this thesis. The batting, sleeving, and cloth were identified as cotton materials; while the towel and white tuff wrap materials were a polyester blend. Figures 3-10:13 show the visual observation of the associated 3D profilometer scans depicting the film surface morphology for each of the tested padding materials. From these results, it is seen that the cotton batting and sleeving (Figure 3-10a) as well as the towel material (Figure 3-11a) do not maintain a controlled area of applied current as seen with the residual deposition along the outer edges of the desired electroplating area. This is of concern because the calculated capacity is determined by a targeted area

and thickness and therefore will not be accurate with the obscurities in deposition area. The cloth material is able to preserve the defined deposition area but however, the current densities exceed the requirement for deposition and 'burning' occurs along the edges of the deposited film (Figure 3-12a). Some adjustments in plating parameters were examined but similar results occurred for the cloth material for both copper and tin deposition. It should also be noted that deposition occurred on the cloth insulating material for several attempts. This was attributed to the cotton cloth material readily absorbing and holding the solution rather than freely distributing the solution through its membrane. The white tuff wrap material produced the best results as depicted by the visual observations of Figure 3-13a where deposition was confined to the desire area of interest and the utilized current density fabricated good films of copper and tin.

The surface morphology of the films produced is of importance because of its effects on diffusion and particle size. Of the four materials examined, the cloth material is the only membrane that produces large variations in surface roughness as seen in Figures 3-10b, 3-11b, 3-12b, and 3-13b. Although the white tuff wrap does not produce the smallest variations in surface morphology, overall data shows that the best films were fabricated with this insulating material. It is concluded from this evidence and the visual observations that texture of the padding material is directly responsible for the morphology of the deposited films.

Table 3-6 Comparison of insulating pad materials for electrodeposition optimization.

Pad Material	FTIR Identification	Material Appearance	Film Average Roughness
Cotton Batting & Sleeving	Cotton		487nm
Towel Material	Polyester Blend	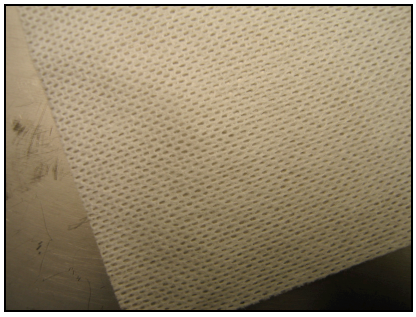	827nm
Cloth Material	Cotton	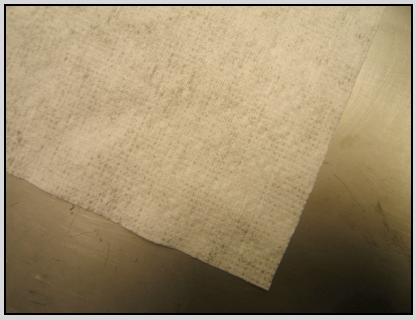	1.24um
White Tuff Wrap	Polyester Blend		548nm

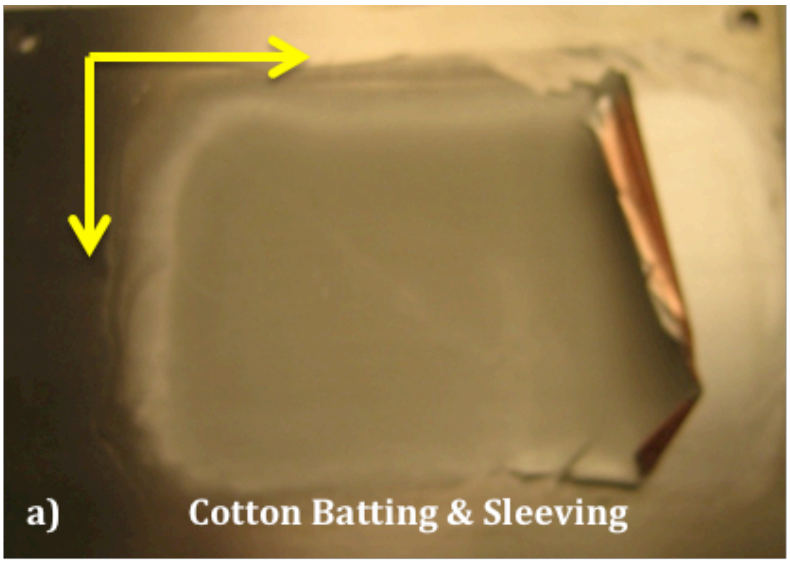

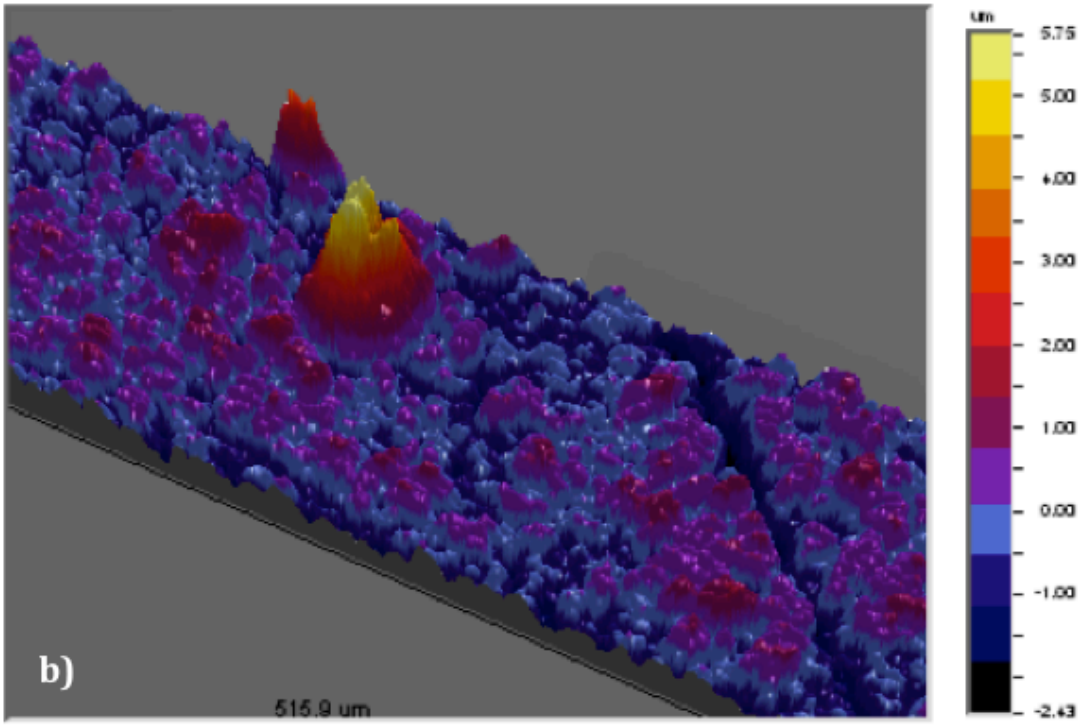

Figure 3-10 Observations for Cotton Batting and Sleeving. a) The arrows highlight the edges of the film, which show residual current density causing deposition outside of the desired area. b) The profilometer scan shows the overall roughness (Average roughness 487nm) of the film being uniform besides the isolated areas.

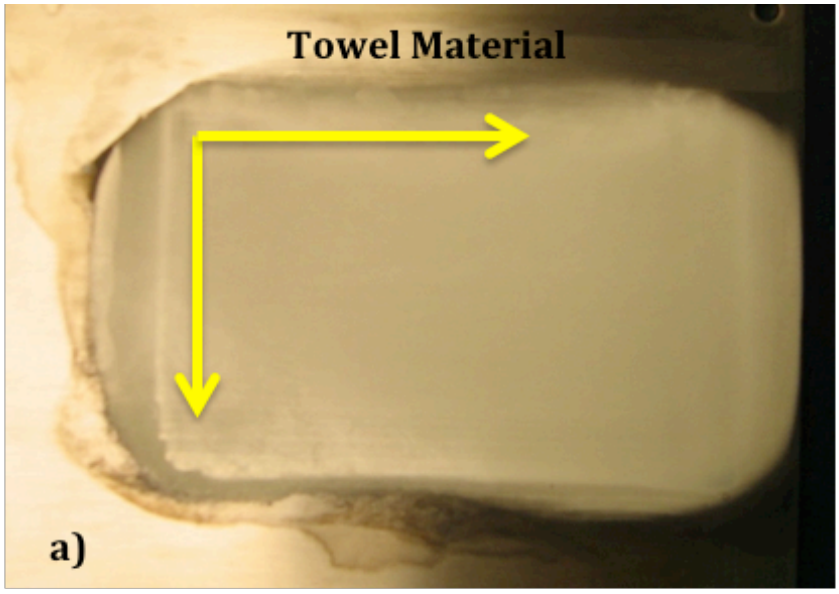

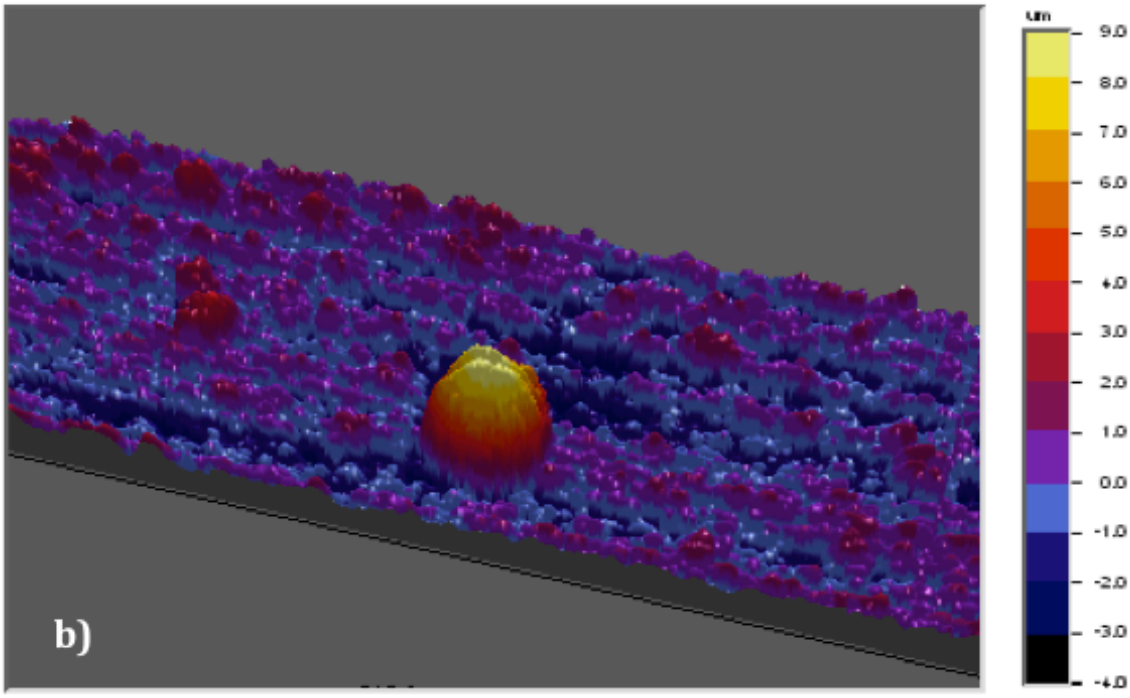

Figure 3-11 Deposition analysis for towel material. a) The arrows highlight the residual areas of deposition caused by the undesirable expanded area of applied current density. b) The profilometer 3D scan shows the roughness (827nm average) of the deposited film.

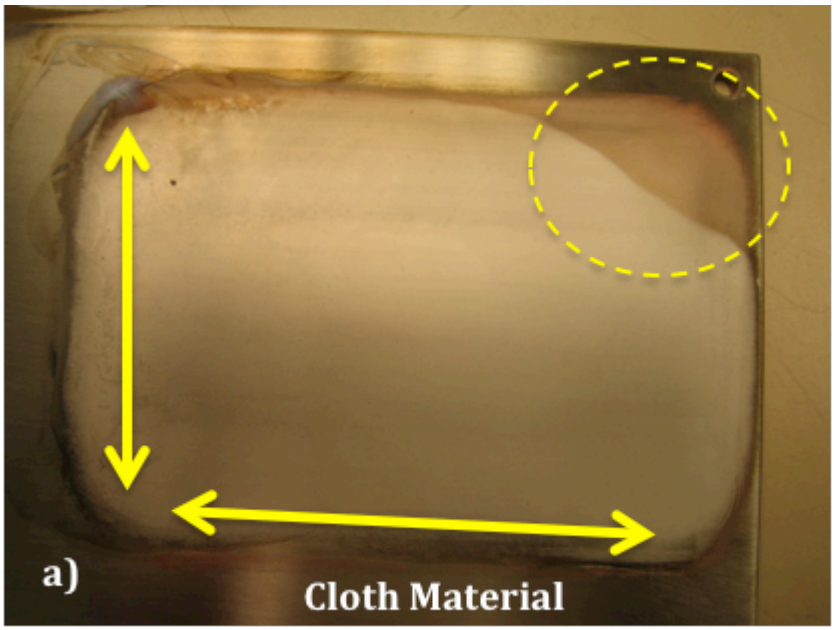

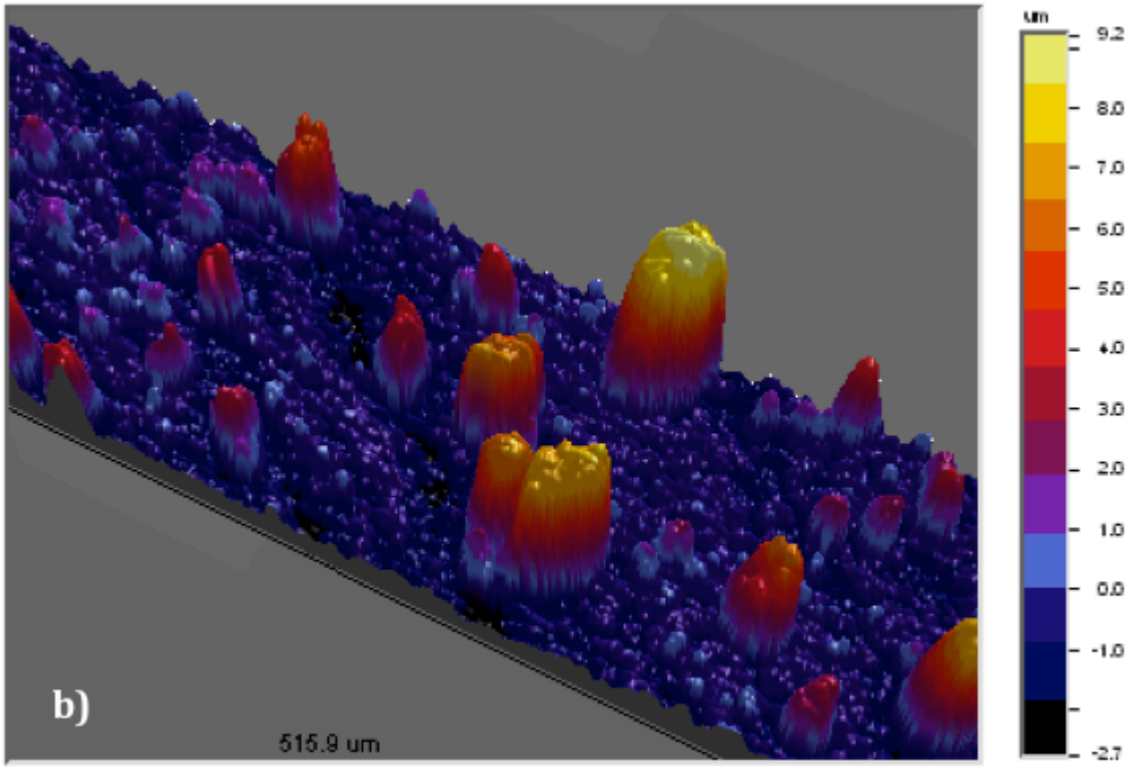

Figure 3-12 Observation for the cloth material. a) The arrows and circled area highlight the burning and discoloration that occurs during plating. b) The 3D profilometer scan shows that the surface morphology contains large variations in roughness (1.24µm average).

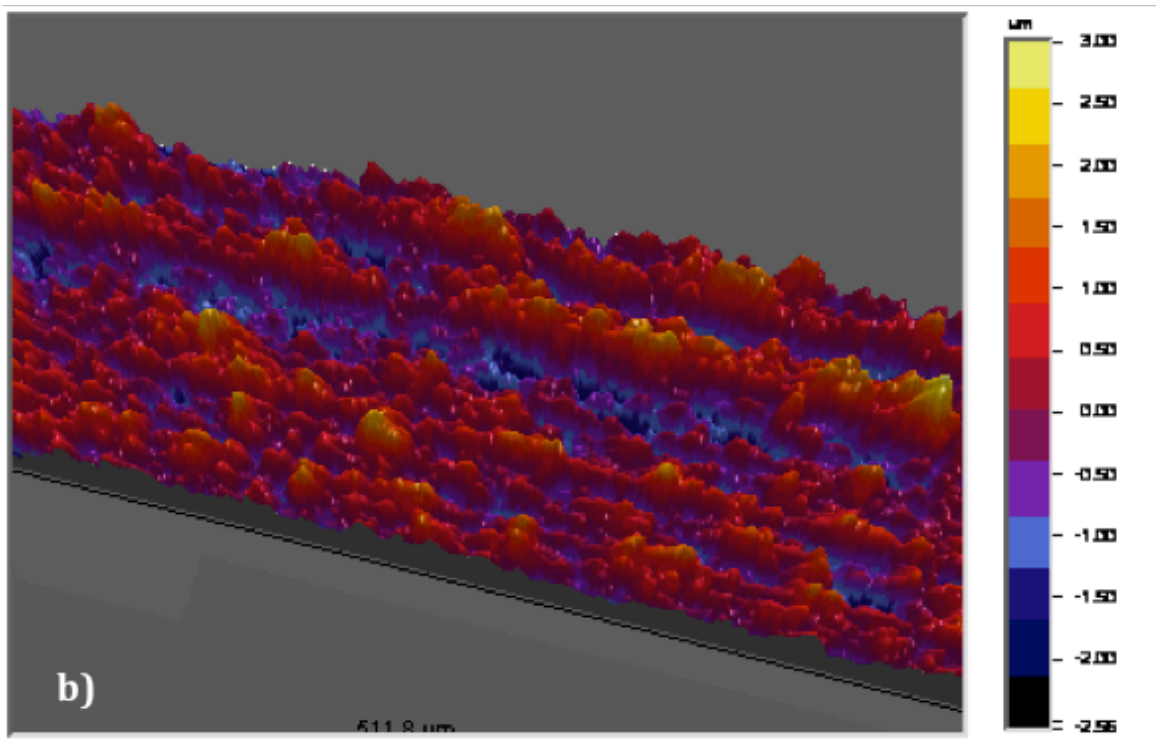

Figure 3-13 Observations for the white tuff wrap material. a) The white tuff wrap had a relatively controlled current density during deposition maintaining deposition in desired area. b) The overall roughness (548nm average) was homogenous throughout the film surface as seen in the 3D profilometer scan.

3.1.5 Pulse Plating Deposition

Table 3-7. Pulsed deposition trials including pulsed potential and pulsed current.

Conditions	1		2		3	
Off Pulse	0V	5sec	0V	0.1sec	0A	0.3sec
On Pulse	5V	5sec	5V	0.1sec	0.1A	0.1sec
Amp-hours Pass	8.0 Ah		7.9 Ah		0.013 Ah	
Tin Thickness Achieved	9μm		12μm		8μm	
Tin Film Average Roughness (R_a)	470nm		420nm		308nm	

Consideration for the utilization of pulse deposition for the tin layer was made to decrease the particle size and improve the electrochemistry of the Cu-Sn alloys. As previously mentioned, the decrease in particle size of lithium alloying materials can increase the strength of the material leading to better retention during cycling [72]. The rectangular pulsing waveforms for three different settings are described in Table 3-7 with variations in time and applied electrical parameter. Recall that a rectangular pulse waveform is described as applying a potential or current for a set time followed by a period of time with no applied potential or current. The pulsed potential trials utilized a 5V potential at varying times (5sec and 0.1sec), while the pulsed current used a 0.1A current for 0.1sec. The off time pulse was originally set for the same amount of time as the on time pulse, however with the short pulse (5V for 0.1sec), the rapid pulsing was determined to be too fast and simulated a constant applied potential deposited film. Therefore for the applied

pulsed current film, the off time was altered to 0.3sec to allow for distinct pulses. The targeted thickness for the tin layer was 8μm. The average surface roughness was determined (profilometer results) for each film to analyze its effects on alloy formation and electrochemistry. From this data it can be seen that the longer pulses of 5V for 5sec produced the film with the highest roughness (470nm). And overall the pulsed current produced the smallest roughness (308nm), which can be associated with smaller particle size.

Table 3-8. XRD analysis for the pulsed films with varying anneal temperatures.

Pulsed Film	Anneal Parameters	SnO	Sn	Cu	Cu_3Sn	Cu_6Sn_5/CuSn
5sec (5V)	Non-Ann	0%	98%	2%	0%	0%
	150°C 8h	0%	54%	0%	15%	31%
	200°C 4h	0%	60%	0%	9%	31%
	275°C 4h	0%	0%	0%	97%	3%
0.1sec (5V)	Non-Ann	0%	99%	1%	0%	0%
	150°C 8h	0%	99%	0%	0%	1%
	200°C 4h	0%	96%	0%	2%	2%
	275°C 4h	11%	8%	0%	51%	30%
0.1sec (0.1A)	Non-Ann	0%	99%	1%	0%	0%
	150°C 8h	0%	99%	1%	0%	0%
	200°C 4h	0%	99%	1%	0%	0%
	275°C 4h	9%	3%	0%	63%	25%

Several heat treatments were examined for each of the pulsed films to determine phase transformation effects as described in Table 3-8. From this data, it can be concluded that the higher temperature (275°C 4h) had the most influence on phase transformations for each of the pulsed films and the smaller pulses of 5V for 0.1sec and 0.1A for 0.1sec produced the most changes in film compositions. The pulsed 5V for 5sec film annealed at 275°C 4h was predominantly composed of Cu_3Sn

(97%). The pulsed 5V for 0.1sec film heat treated at the same temperature achieved a mixture of Cu_3Sn (51%) and Cu_6Sn_5 (30%). Similarly, the pulsed 0.1A for 0.1sec film produced a mixture of Cu_3Sn (63%) and Cu_6Sn_5 (25%).

Table 3-9. Electrochemical analysis of pulsed deposition films. The difference of 1st lithiation and delithiation is described by the irreversible loss.

Pulsed Film	Anneal Parameters	1st Lithiation *mAh/cc*	1st Delithiation *mAh/cc*	2nd Lithiation *mAh/cc*	Irreversible Loss %
5sec (5V)	Non-Ann	3607	791	638	78%
	150°C 8h	3350	12	1481	99%
	200°C 4h	1015	561	107	45%
	275°C 4h	745	580	118	22%
0.1sec (5V)	Non-Ann	4432	0	0	100%
	150°C 8h	1080	0	0	100%
	200°C 4h	5317	529	319	90%
	275°C 4h	1158	966	991	17%
0.1sec (0.1A)	Non-Ann	3859	0	0	100%
	150°C 8h	4647	0	0	100%
	200°C 4h	4331	0	73	100%
	275°C 4h	2178	1958	1472	10%

The electrochemical results for each of the films are described in detail in Table 3-9. From this data it can be seen that as expected, the films with predominantly pure Sn have very high initial lithiation capacities but extreme irreversible loss (45-100%). Each of the films heat-treated at 275°C 4h presented much lower irreversible losses (10-22%) and therefore a closer examination of capacity retentions in Figure 3-14 has been utilized to compare the effects of pulsing overall.

The electrochemical results in Figure 3-14 show that both the shorter pulses of 0.1sec (5V and 0.1A) produce higher capacity films. After removal of initial irreversible loss, the pulsed 5V for 0.1sec film and the 0.1A for 0.1sec film had volumetric lithiation capacities of 860 and 1130mAh/cc respectively. At the same time, the pulsed 5V for 5sec film had a volumetric lithiation capacity of approximately 470mAh/cc. However, the pulsed 5V for 5sec film had better overall capacity retention, maintaining 470mAh/cc for most of the 50 cycles. This was not

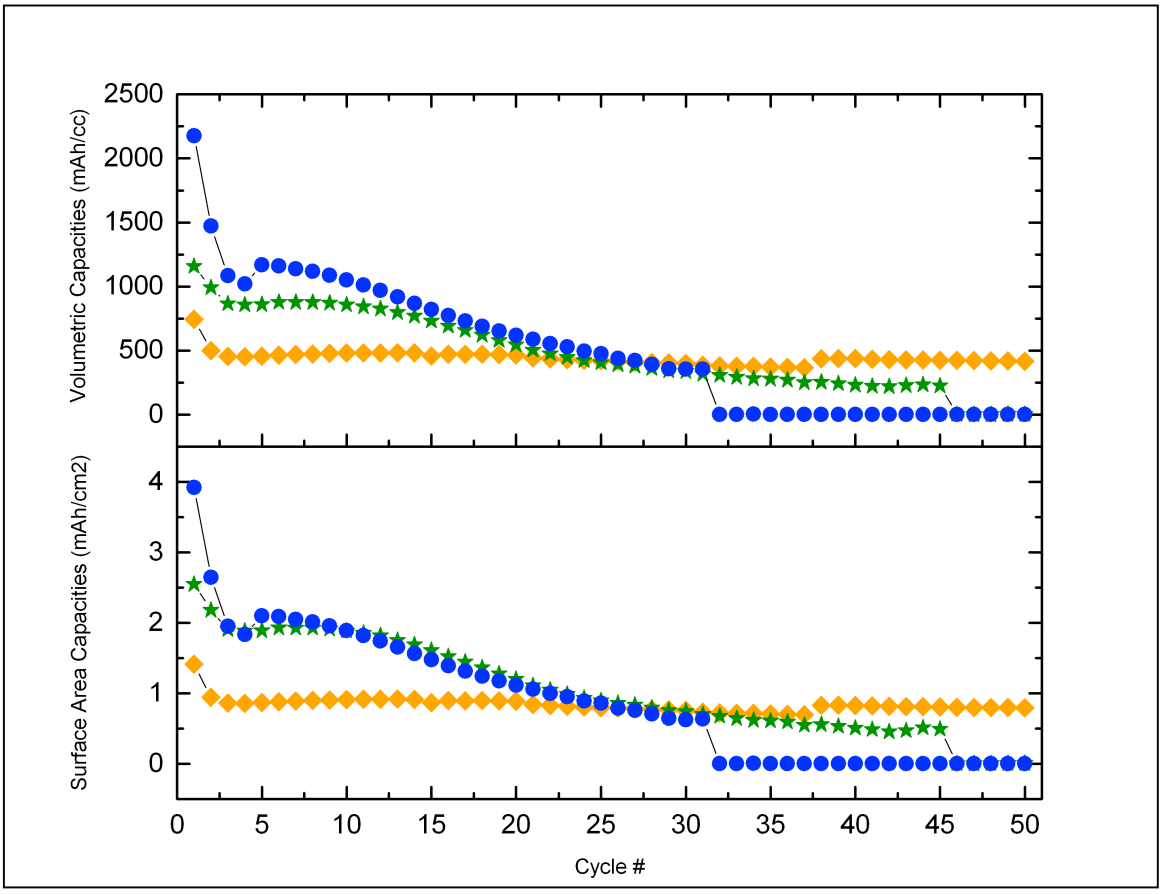

Figure 3-14 Areal lithiation capacity comparisons for pulsed deposited films. ●: pulsed 0.1A for 0.1sec film; ◆: pulsed 5V for 5sec film; ★: pulsed 5V for 0.1sec film.

the case for the shorter pulsed films, which experienced catastrophic failure after 45 (pulsed 5V for 0.1sec) and 31 (pulsed 0.1A for 0.1sec) cycles. These differences in electrochemistry are attributed to the dissimilarities in phase transformations, which have occurred due to the time allowed for nucleation and growth during deposition. The larger particles fabricated from the longer periods of pulses do not undergo the same diffusion characteristics as the smaller particles from the shorter pulsed depositions. Therefore it is concluded that shorter pulsed depositions helped in improving the phase outcome from heat treatment by increased diffusion from smaller particles. But the quicker capacity failure may occur because the smaller particles of the shorter pulsed films have a higher tendency of particle aggregation as discussed in an earlier section of this paper.

The overall comparison of pulsed deposition and constant applied current deposition are compared electrochemically in Figure 3-15. The phase composition of the constant current deposited film is as follows: 23% SnO, 6% Sn, 10% Cu_3Sn, and 61% Cu_6Sn_5/CuSn. The first few cycles of the constant applied current deposited film experienced low capacities, probably due to accessibility and diffusion limitations that will not be discussed in this section. Overall it can be seen that the short-pulsed films (5V for 0.1sec and 0.1A for 0.1sec) have comparable

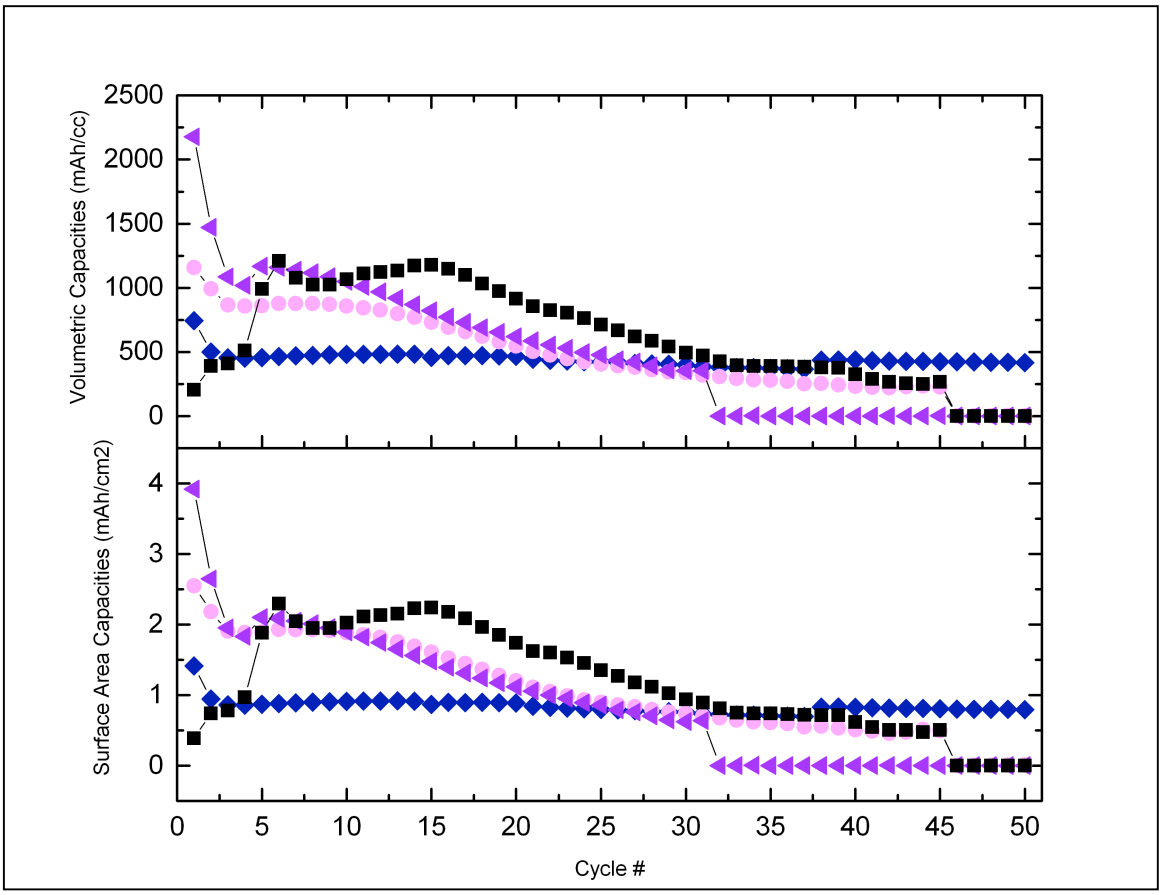

Figure 3-15 Electrochemical comparison of pulsed and constant deposition films (10microns:8microns). ■: deposition by constant applied current; ◆: deposition by pulsed 5V for 5sec; ◀: deposition by pulsed 0.1A for 0.1sec; ●: deposition by pulsed 5V for 0.1sec.

capacities (~1000mAh/cc and 2mAh/cm^2) to the film produced by constant applied current parameters (1200mAh/cc and 2mAh/cm^2). At this time, no large beneficial differences have been seen between the pulsed and constant parameter film depositions for our meniscus brush plating system. Future investigations may be of interest at later stages of electrodeposition research.

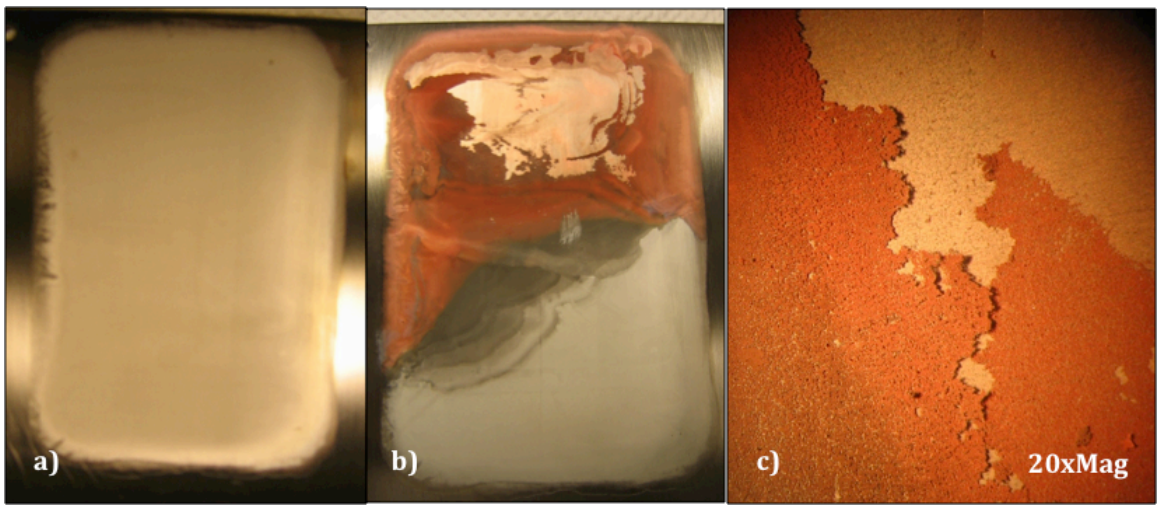

Figure 3-16 Observed electroless plating that occurs when introducing copper sulfate plating solution to surface of tin film. a) Tin film plated on top of existing initial copper layer. b) Areas of contact for the copper solution with the tin film caused discolored copper film to form without any applied potential/current (electroless plating). c) Higher magnification (20x) shows that copper layer does not form a strong bond with surface film as desired from electrodeposition.

3.1.6 Multilayer Deposition

The electrodeposition of several alternating layers of copper and tin were briefly investigated to determine the feasibility of multilayer plating to fabricate complex architectural copper-tin films. The purpose of depositing additional layers beyond initial films of copper and tin was to increase the diffusion capabilities

during heat treatment to create the desired copper-tin alloys for electrochemical testing. The first layers of copper and tin were approximately 5μm in thickness. Immediate contact of the copper solution with the surface of the tin film caused electroless deposition to occur as seen in Figure 3-16. This occurs because the higher redox potential of the Cu^{+} relative to Sn^{2+} and proceeds uncontrollably. Therefore it is concluded that multilayer electrodeposition was not an option for this project.

Plating Solution	Plating Solution Components
Copper Acid Code 2050/5250	Copper (II) Sulfate
	Sulfuric Acid
	Water
Tin Code 2093	Stannous Methane Sulfate
	Methane Sulfonic Acid
	Water

3.1.7 Mixed Plating Solutions For Codeposition

Table 3-10 Description of plating solution components.

The concept of dual electrodeposition of copper and tin was examined with the blending of the two plating solutions provided by SIFCO. This idea was investigated as a possible avenue to improve the Cu-Sn alloys achieved during the anneal stage of our process. Codeposition of copper and tin for Cu-Sn alloys in lithium ion battery research has been studied in the past and requires the use of compatible components for the metal ions to both be stable within the solution [73,74,75,76]. The components of the Copper Acid Code 2050/5250 and Tin Code

2093 are listed in Table 3-10. Determination of mixed solution compatibility was examined with the creation of three mixtures in 20mL glass vials: #1 75% copper solution: 25% tin solution; #2 50% copper solution: 50% tin solution; #3 25% copper solution: 75% tin solution. The three mixtures were monitored over several days to determine if the two solutions could stably be combined for codeposition. Figure 3-17 shows the results of the mixed solutions over a ten-day span. From these results, it is easily seen that the 50%:50% solution and 35%:75% solution (copper:tin) were not compatible and formed opaque solutions immediately after mixing, followed by the precipitation of an additional phase over time. The 75%:25% solution also produced a small visible amount of precipitation by the six day. The formation of precipitations for each of the solution mixtures helps to conclude that the Tin Code 2093 solution is not fully compatible with the Copper Acid 2050/5250 solution and therefore codeposition with these prepared solutions is not feasible.

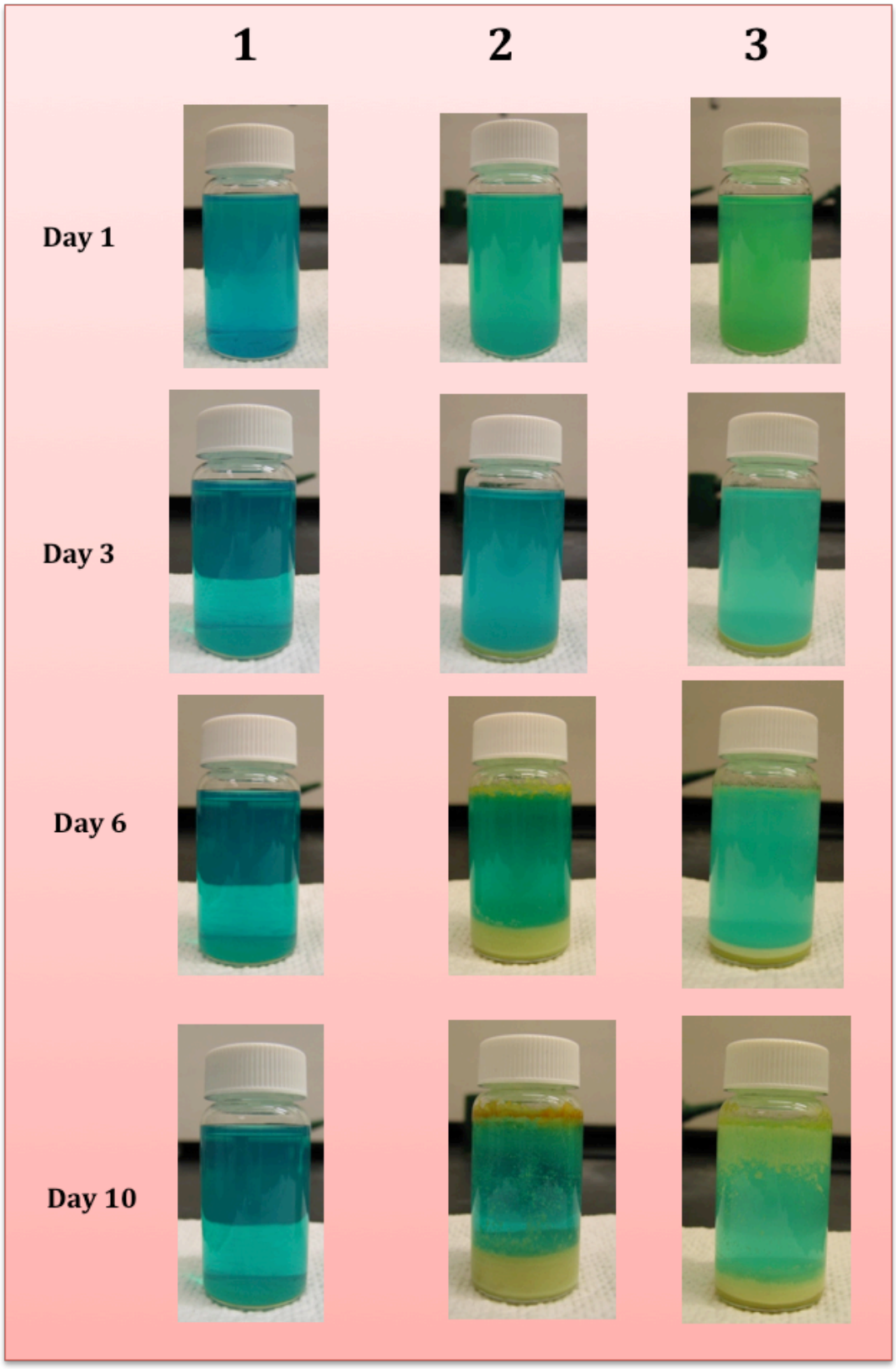

Figure 3-17 Visual observations of mixing copper and tin solutions over a 10-day span.

3.1.8 Conclusions

Many factors played a role in the optimization of the physical properties for the deposited copper and tin films from the meniscus brush plating process. Achievement of a strong well-deposited film was accomplished with fine-tuning the movement of the electrodes with the applied electrical current. Due to the orientation and movement of the electrodes in this setup, the increased current density helped in decreasing the capacity needed for film formation. From collected observations and data, it was also concluded that settings just beyond deposition 'burning' were ideal for good plating. Other factors such as padding material and substrate were also influential factors that required careful choosing for the freestanding films. Overall, it was determined that the white tuff material and titanium plate satisfied the requirements for the copper-tin films. More advanced studies, such as pulsed electrodeposition helped prove the capabilities of pulsed deposition for modifications of the film particle sizes. Currently the best pulse deposition films do not experience superior electrochemical characteristics to the constant applied current deposited films and therefore have not been extensively further researched at this time. Other areas of interest included the creation of more complex systems with multi-layer deposition and codeposition but trials conducted have led to more brainstorming of alternate options for improving the film architecture for better electrochemical results moving forward.

3.2 Heat Treatment Optimization

The heat treatment process following deposition of the freestanding films

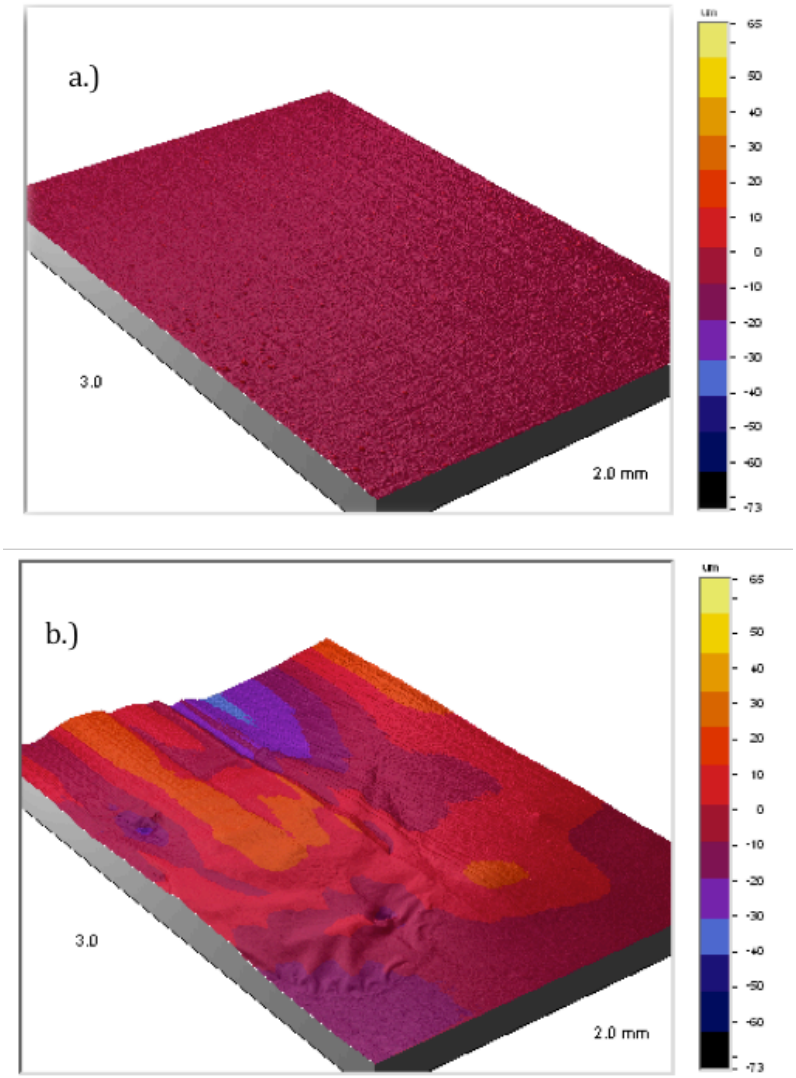

Figure 3-18 Profilometer 3D scans of surface topography. a) The surface of the non-annealed Cu-Sn film appears to be uniform and smooth (average roughnes: 487nm). b) The film annealed at 275°C 4h has formed a "hills and valley" topography (average roughness: 7.76µm).

was utilized to form Cu-Sn alloys to create a composite film for better cycling stability of the lithium alloy, tin. Various temperatures were investigated to analyze the effect on phase transformation and produce different phase percentages for electrochemical studies. Following heat treatment at 275°C 4h when no pressure was applied to the film (uncovered) in the enclosed tube furnace flowing argon, the film surface appeared to be warped as seen in the profilometer scan comparison in

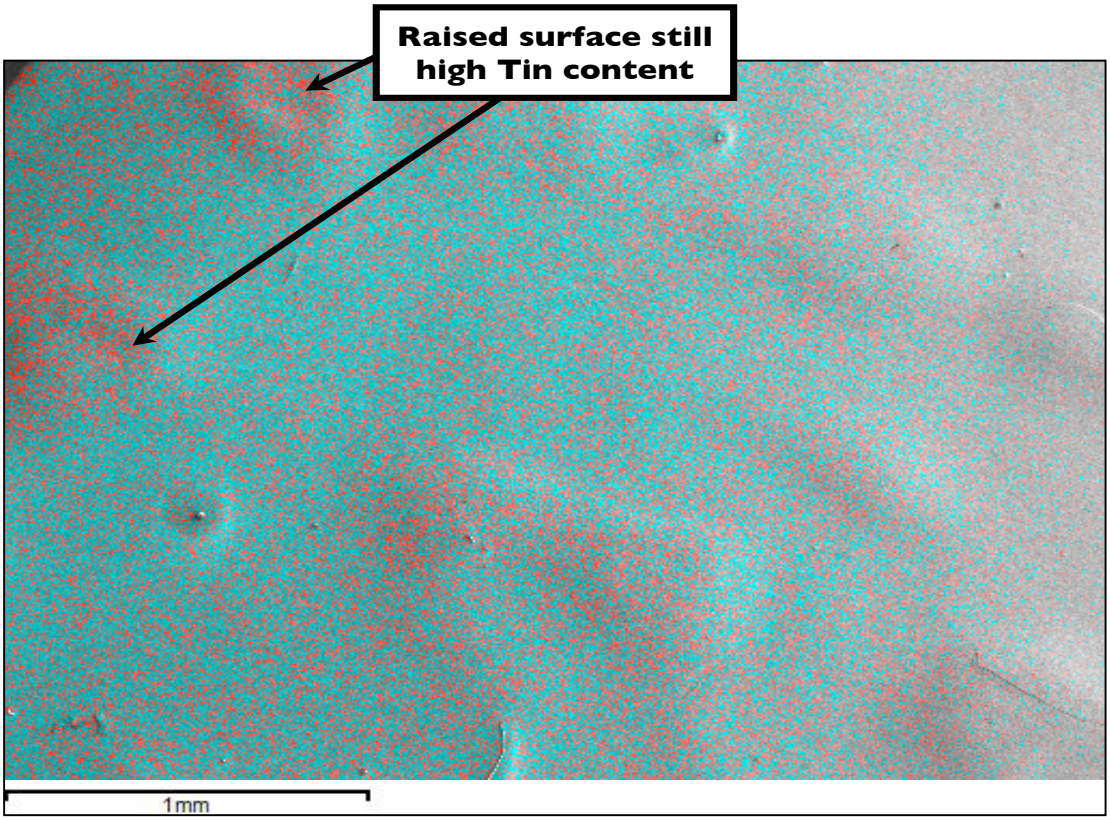

Figure 3-19 FESEM EDS analysis of the Cu-Sn 275°C 4h film. The raised areas were dominant in tin (red) content while the 'valleys' had a higher copper (blue) content.

Figure 3-18. The original deposited non-annealed film (Figure 3-18a) has very little

topography differences as seen in the low roughness measurement of 487nm. However, upon heat treatment at 275°C 4h, the surface of the film (Figure 3-18b) becomes distorted and obtains an average overall roughness of 7.76µm. FESEM imaging and EDS spectrum analysis were examined to determine detailed areal analysis as seen in Figures 3-19 and 3-20. The elemental analysis of Figure 3-19 shows the concentration differences between the topographic areas of the film where tin has been identified in red and copper identified as blue. Continuing with this observation, the elemental spectrum confirms these findings in Figure 3-20a and 3-20b. This phenomenon has been sourced to the tin melting and readily

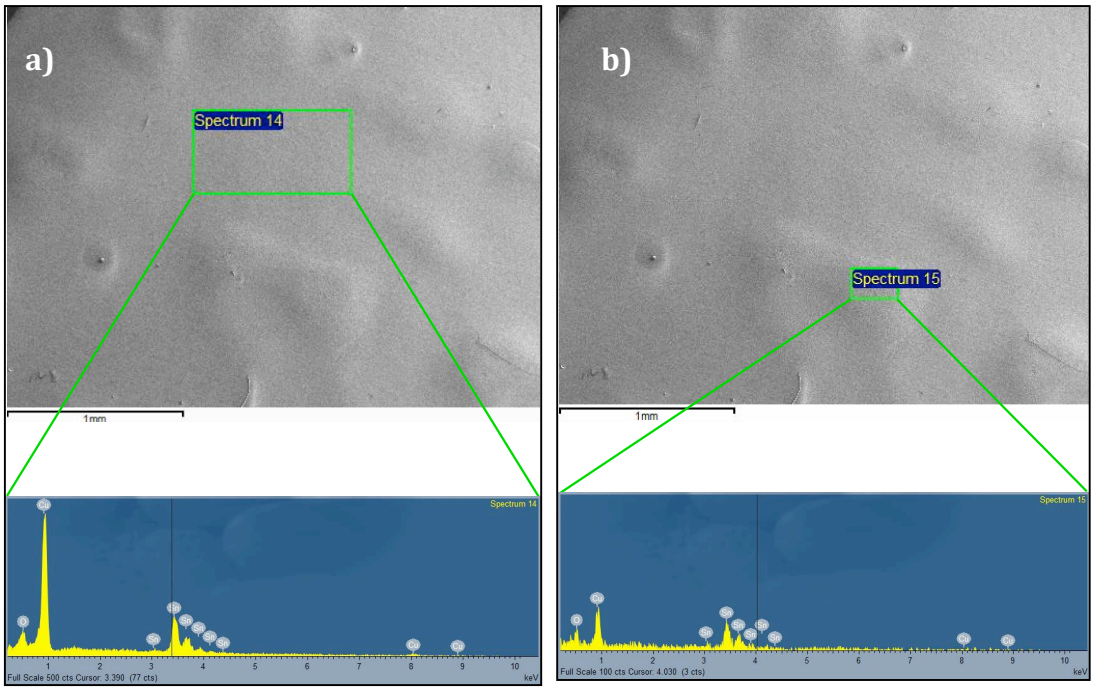

Figure 3-20 FESEM EDS spectrum analysis for the 'hills and valleys' of the 275°C 4h Cu-Sn film. a) Spectrum shows dominance in copper for the valley area of the film. b) Spectrum identifies dominance in tin for the hill area of the Cu-Sn film.

pooling on the surface of the film instead of fully diffusing with the copper. To confirm the melting of the tin, the Cu-Sn films were investigated via DSC analysis. This investigation included heat treatment analysis of 5°C/min to 300°C under Argon. The results are included in Figure 3-21, which clearly identify the endothermic reaction caused by the melting of the tin in the Cu-Sn films. The onset temperature for melting occurs at approximately 226°C.

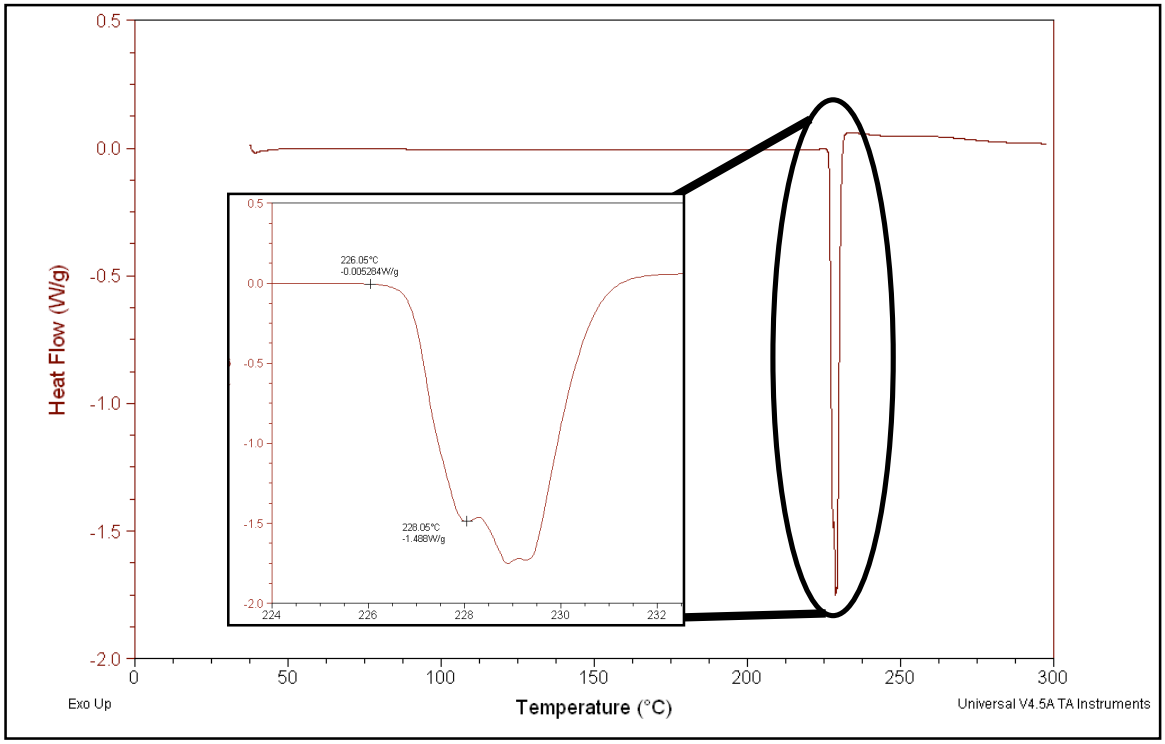

Figure 3-21 DSC analysis of the Cu-Sn film. The identified endothermic peak of the spectrum confirms the melting of the tin at approximately 226°C.

The heat treatment concept for the freestanding films required adjustment to improve the diffusion capabilities to obtain the desired alloy phases and suppression of pure tin. The final decision was made to incorporate the addition of stainless steel plates and Teflon films for applied pressure during heat treatment. This setup sandwiched the Cu-Sn films between Teflon films to assure the films

would not adhere to the smooth flat stainless steel plates during anneal. Uniform pressure was applied via torque wrench to promote diffusion of the copper and tin. Pressure ranges of 6in.lbs-16in.lbs were investigated and it was concluded that the best results were obtained from applying 8in.lbs. Higher amounts caused the tin to be excreted during heat treatment and lower amounts did not promote enough diffusion as seen from excess pure tin during x-ray analysis.

3.2.1 Conclusions

Tin has a lower melting temperature than copper, which causes the tin to aggregate on the surface of the Cu-Sn film when the film is openly heat treated with no applied force. This causes distorting of the film surface with the formation of 'hills and valleys' in the topography of the film. Due to the irregularity in chemistry of the Cu-Sn film from this occurrence, the heat treatment process was redesigned to include uniform applied pressure to promote better diffusion of the tin with the copper layer. Moving forward, all the freestanding Cu-Sn films were heat-treated utilizing this design.

3.3 Single Cu-Sn Bilayer Thickness Optimization

3.3.1 Thin Bilayer Copper-Tin Films: 5.68micron Tin Layer

The initial electrodeposited films of 3μm of copper followed by 5.68μm of tin

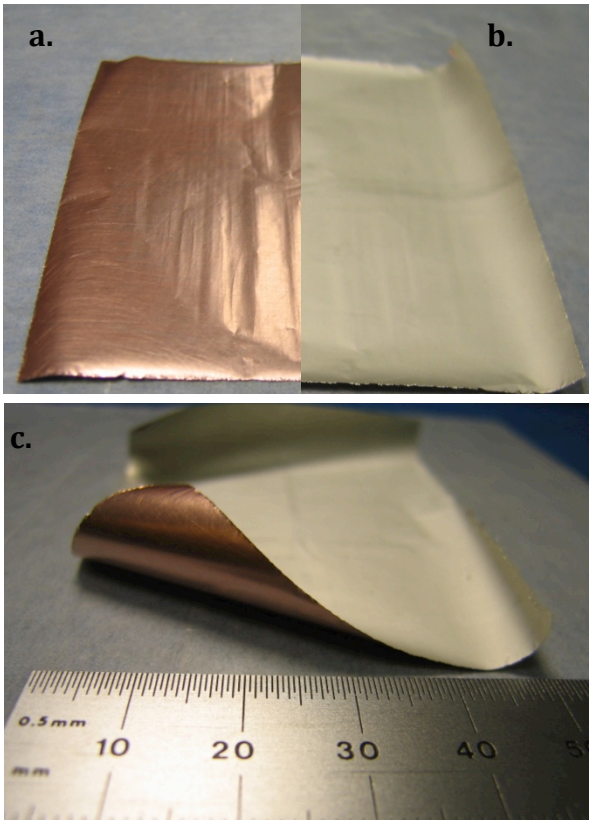

Figure 3-22 Freestanding electrodeposited Cu-Sn film; a) Bottom of film showing copper layer; b) Top view showing tin layer; c) Curled film shows freestanding capabilities.

metal, resulted in a 1.33:1 molar ratio of deposited copper:tin based on thickness of the layers and the pycnometry of the pure layers. Figure 3-22 shows an image of the

freestanding deposited bimetallic film. XRD confirmed the single-phase depositions of Cu (Fm-3m) and Sn (I41/amd) by individual top surface analysis.

Table 3-11. XRD of a 225°C 4h annealed single bilayer 5.68µm Cu-Sn film.

Analysis Direction	Cu	Sn	Cu_3Sn	Cu_6Sn_5/CuSn
Top of Film	0%	10%	67%	22%
Bottom of Film	29%	29%	34%	8%

Heat treatment at 225°C 4h yielded the composite density of 8.077g/cc (targeted intermetallic phase Cu_6Sn_5 has a theoretical density of 7.989g/cc) and the intermetallic phase distribution described in Table 3-11 from XRD analysis. Top and bottom XRD analysis were utilized to compensate for the limitations of the x-ray

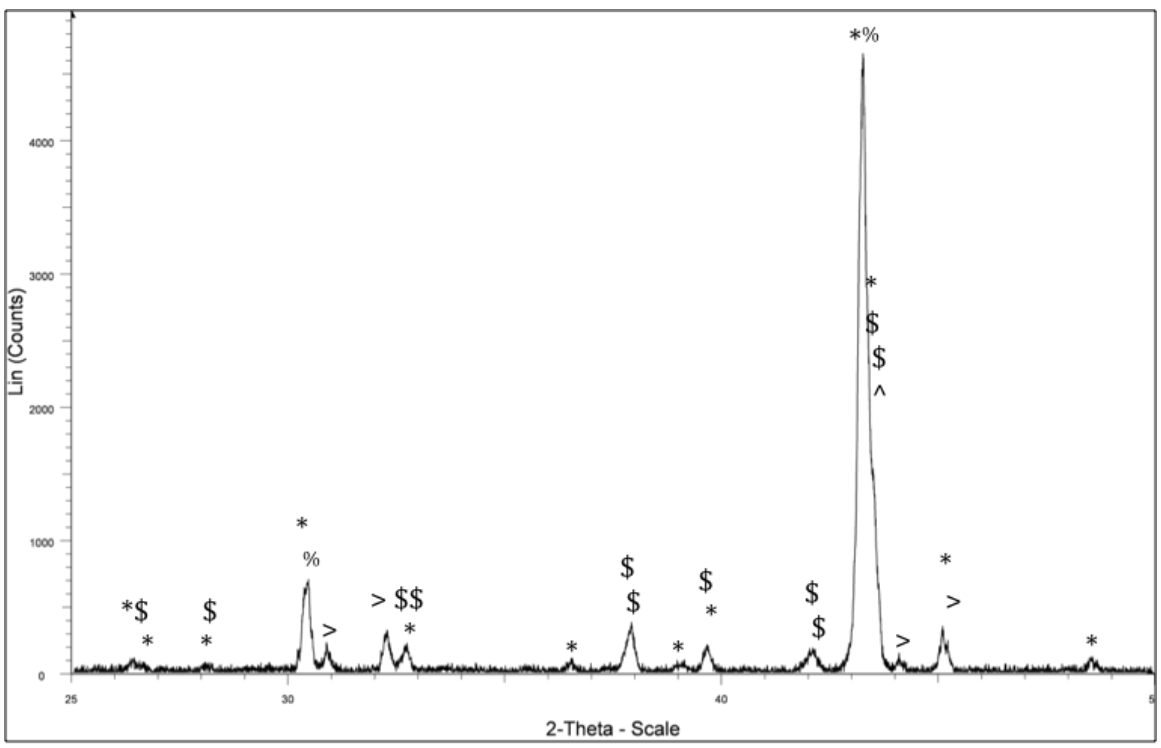

Figure 3-23 XRD top surface analysis for the 1.33:1 molar ratio film with phases identified as: Cu_6Sn_5 (*), Cu_6Sn_5' (^), $Cu_{3.02}Sn_{0.98}$ ($), CuSn (%), Sn (>).

penetration depth (8.5μm) because the total film thickness was 18μm. As expected from visual observations, the bottom surface x-ray confirms pure copper present within the film along with the formation of alloy phases. Although Cu_6Sn_5 (C2/c) and CuSn (P6[3]/mmc) are respectively monoclinic and hexagonal, these structures are similar leading to sets of convoluted Bragg reflections difficult to distinguish from each other as seen in Figure 3-23 of the top surface XRD analysis. These phases will therefore be referred as the single phase Cu_6Sn_5/CuSn. Due to these convolutions, further structural examination with Reitveld analysis has not been successfully executed because of the alloy complexity. Variations in the intermetallic and pure phases for the two directions of XRD analysis reveal the diffusion of the two metals is not uniform throughout the composite. With about 96% of the composite film covered by the two directions of x-ray penetration, the overall distribution suggests that the molar ratio of 1.33:1 is more favorable for producing Cu_3Sn as the dominant intermetallic phase and Cu_6Sn_5/CuSn as the secondary phase.

Figure 3-24 shows the initial voltage profile of the annealed thin single bilayer 1.33:1 copper:tin film. The electrochemical reaction initiated at approximately 0.38V is consistent with the formation of the lithium-tin alloy, $Li_{22}Sn_5$ [77]. Combined with low irreversible losses of 8%, the joint deposited/thermal anneal process we developed successfully allowed for tin lithiation devoid of large irreversible losses associated to SEI formation. Based on the tin weight in the 1.33:1 bilayer film and calculated density from pycnometry, the film experimental volumetric capacity achieved consisted of 5316mAh/cc, equivalent to 74% of the theoretical 7202mAh/cc capacity. As a result, residual tin is inaccessible for

lithiation established by the architectural structuring within the film. Since past research suggests that the Cu_6Sn_5 phase is favorable for high capacity achievement

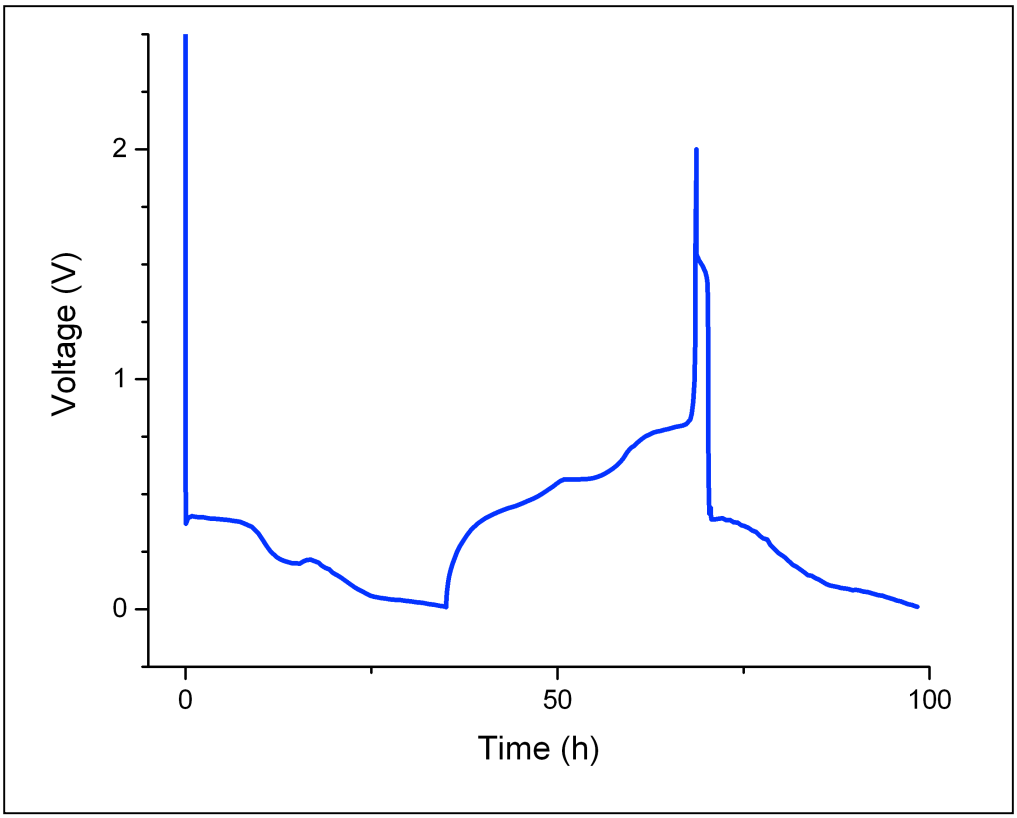

Figure 3-24 Voltage vs. time for the initial 1.5 cycles of the single bilayer 5.68micron Cu-Sn film.

and electrochemical stability, the film Cu:Sn molar ratio was adjusted to preferentially form Cu_6Sn_5/CuSn [77,78].

3.3.2 Thick Bilayer Copper-Tin Films: 17µm & 8µm Tin Layers

Thicker bimetallic films were fabricated in order to achieve higher areal capacities. In addition, impact of the molar ratio was investigated in this thicker bimetallic film format with larger copper excess (2.57:1 Cu:Sn) as well as with tin

excess (1:1.22 Cu:Sn). In both sets of films, the Cu thickness remained constant at 10μm while the Sn varied from 8 to 17 μm respectively.

Table 3-12 XRD analysis (top) for the annealed thick single bilayer Cu-Sn films (10micron:17micron).

Film Anneal	*SnO*	*Sn*	*Cu_3Sn*	*Cu_6Sn_5/CuSn*
Non-Ann	0%	100%	0%	0%
150°C 8h	0%	100%	0%	0%
200°C 4h	0%	100%	0%	0%
275°C 4h	14%	1%	28%	57%

The tin excess bilayer film, 10μm of copper metal and 17μm of tin metal, had a molar ratio of 1:1.22. Due to the large increase in tin content and film thickness, several anneal temperatures and times were investigated as shown in Table 3-12. Sufficient diffusion to develop intermetallic phases was not achieved until 275°C 4h, resulting in the formation of Cu_6Sn_5/CuSn and Cu_3Sn and the addition of a small amount of SnO. Table 3-12 only examines the top surface XRD analysis for these films due to the copper layer thickness resulting in bottom surface analysis of nearly 100% copper phase for each of the films. The poor phase development in these films led to poor electrochemical performance as described in Table 3-13. The non-annealed, 150°C 8h, and 200°C 4h annealed films experienced detrimental initial cycling with approximately 100% irreversible loss. The thick bilayer film annealed 275°C 4h had low irreversible loss (8%) but further examination of the capacity retention in Figure 3-25 showed that both the phase development assessed and undetected by the limitations of the XRD penetration depth were not sufficient to

avoid early decrepitation and additional cycling irreversible loss. This was further supported by the calculated cycle life of the film (6 cycles) based on a 20% decreased capacity after the initial irreversible losses of the first 3 cycles. This helped to conclude that the tin excess bilayer film was not capable of achieving the set goals of this project.

Table 3-13 Electrochemical analysis of the thick single bilayer Cu-Sn (10micron:17micron) films showing the results for the first 1.5 cycles and the initial irreversible loss. The irreversible loss is defined as the difference between the first lithiation and delithiation.

Film Anneal	1st Lithiation		1st Delithiation		2nd Lithiation		Irreversible Loss %
	mAh/cc	mAh/cm²	mAh/cc	mAh/cm²	mAh/cc	mAh/cm²	
Non-Ann	3459	9.34	0	0	6	0.02	100%
150°C 8h	7747	21.0	1	0.01	807	2.18	99.9%
200°C 4h	2709	7.31	0	0	0	0	100%
275°C 4h	2150	5.80	1970	5.32	1547	4.18	8%

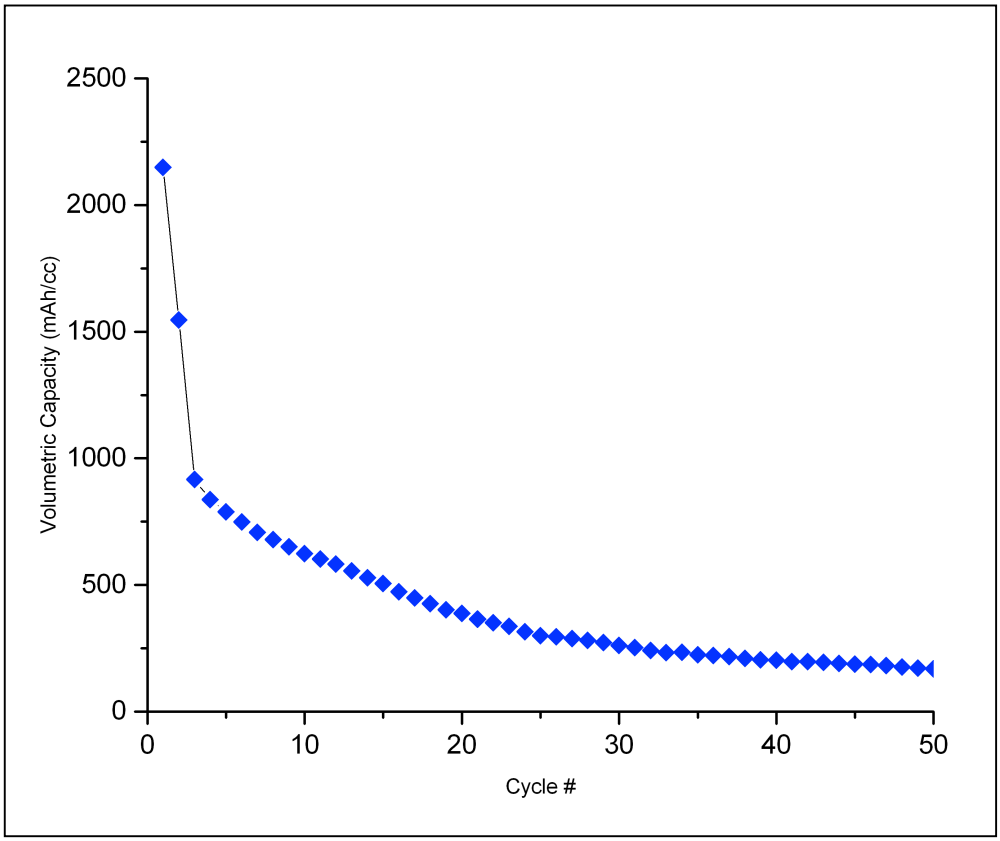

Figure 3-25 Electrochemical analysis of the annealed 275°C 4h thick bilayer (1:1.22 molar ratio) film showing the poor lithiated (◆) volumetric capacity retention over 50 cycles despite low initial irreversible loss

The copper excess thick bilayer film was fabricated from 10μm copper and 8μm tin (molar ratio of 2.57:1). Different anneal temperatures were analyzed for their phase compositional effects in Table 3-14, while Table 3-15 examined the early cycling and irreversible loss for these films. Similar to the tin excess film (1:1.22 molar ratio), the copper thickness (10μm) for the 2.57:1 molar ratio film impeded bottom XRD analysis from showing phase formation other than the pure copper phase and has been omitted from the described XRD results (Table 3-14). The film heat-treated at 275°C 24h, Cu_3Sn phase dominant (58%), had the highest initial

capacities but lower retention (43%). Similarly, the 225°C 8h annealed film had poor retention (60%), most likely attributed to its high content of residual pure tin phase and insufficient alloy formation. The 325°C 4h heat-treated film produced the highest amount of Cu_3Sn (70%) but only 20% Cu_6Sn_5/CuSn, which lead to low accessible tin for lithiation and lower capacities. Finally, the 275°C 4h heat-treated film had the highest irreversible loss (48%) with mediocre capacities, which can be attributed to the high SnO phase. Overall the intended phase distribution (Cu_6Sn_5 dominant film with low pure tin, SnO, and Cu_3Sn phases) from the 2.57:1 molar ratio was not achieved and further characterization was needed to understand the phase development within the films.

Table 3-14 XRD analysis for the annealed thick single bilayer Cu-Sn (10micron:8micron) films.

Film Annealed	*SnO*	*Sn*	*Cu_3Sn*	*Cu_6Sn_5/CuSn*
225°C 8h	2%	26%	41%	31%
275°C 4h	23%	6%	10%	61%
275°C 24h	7%	6%	58%	29%
325°C 4h	6%	4%	70%	20%

Table 3-15 Electrochemical analysis for the first 1.5 cycles of the thick single bilayer Cu-Sn (10micron:8micron) films. The difference in the first lithiation/delithiation is defined as the irreversible loss.

	1st Lithiation		1st Delithiation		2nd Lithiation		Irreversible Loss %
	mAh/cc	mAh/cm²	mAh/cc	mAh/cm²	mAh/cc	mAh/cm²	
225°C 8h	1450	3.48	1253	3.01	861	2.07	14%
275°C 4h	204	0.39	106	0.20	391	0.74	48%
275°C 24h	2302	5.07	1645	3.62	998	2.20	29%
325°C 4h	402	0.68	308	0.52	170	0.29	23%

Microscopy analysis conducted on the cross section of the thick bilayer films (10micron: 8micron) investigated the elemental distribution, morphology, and structural network. Figure 3-26 and Figure 3-27 compare the transformation of the film from the non-annealed state to the thermal anneal transformation at 225°C 8h. This comparison and direct identification of the copper and tin within each film provides

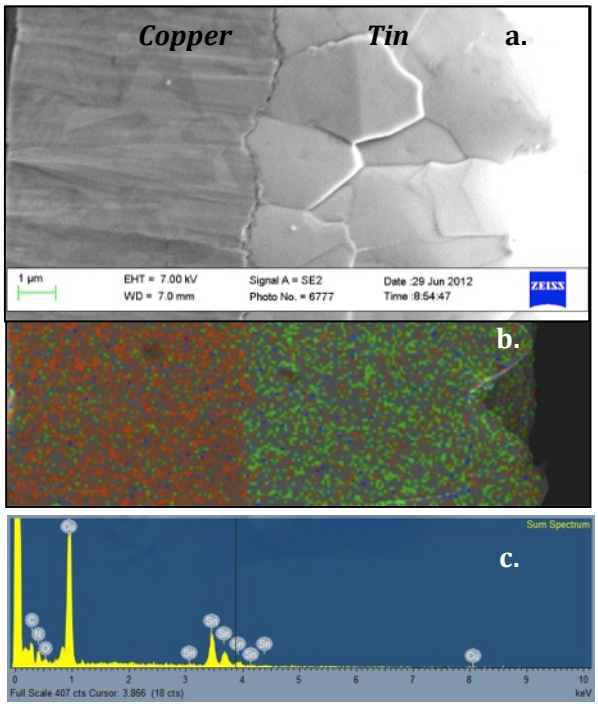

Figure 3-26 FESEM & EDS analysis of non-annealed thick single bilayer film (10micron: 8micron) a.) Secondary electron image of tin plated on plated copper film; b.) EDS elemental mapping of two different metal films; c.) Wide field EDS spectra for identified metal films.

evidence that the copper from the bottom of the film, even with the decrease of the tin, is still restricted from full diffusion to promote the Cu_6Sn_5/CuSn phase. Other annealed 10micron:8micron films similarly confirmed residual pure copper and tin at their respective bottom and top surfaces of the film. This concludes that the reduction of the tin layer from the 1:1.22 molar ratio film to the 2.57:1 film was still unable to achieve full diffusion to form the desired intermetallic phases. Therefore, to maximize phase transformations with Cu_6Sn_5/CuSn as the dominant phase and limit the undesired components of SnO, pure Sn, and Cu_3Sn, an alternative electrodeposited film approach was investigated for increased diffusion capabilities without the sacrifice of electrochemical properties.

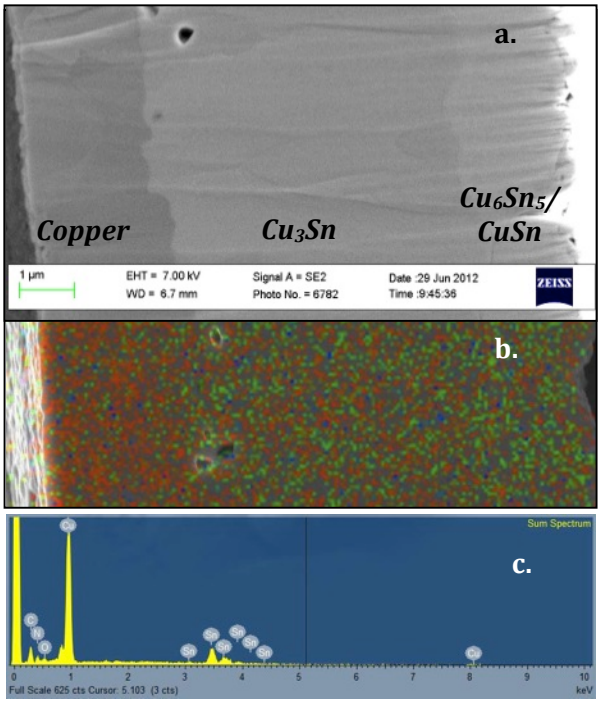

Figure 3-27 FESEM (a) and EDS (b and c) of 225°C 8h single bilayer film (10micron:8micron).

3.3.3 Conclusions

The single bilayer Cu-Sn films deposited via the meniscus brush plating system successfully proved that freestanding films with heat treatment could produce composite Cu-Sn alloys with improvements to issues (irreversible loss and cycling) that typically plague lithium alloys. The different thicknesses observed

attempted to modify the phase transformations to produce films of mostly the Cu_6Sn_5 phase, which is known to be a successful high capacity composite. Both the thin (3microns:5.68microns) and thick (10microns:17microns) or (10microns:8microns) films were not able to achieve full diffusion, which stunted the promotion of phase transformations and hindered capacity retention. This has led to the fabrication of more complex films.

3.4 Triple Stack Thin Copper-Tin Films

3.4.1 Structure Analysis of Triple Stacked Bilayer Films

Three thinner bimetallic Cu-Sn films were stacked and annealed in order to induce more facile diffusion of the Cu-Sn species for the formation of the desired Cu_6Sn_5/CuSn intermetallics and high areal capacities. Aside from potential as a viable current collector, the copper within the film provided support as a buffering matrix layer for tin lithiation, resulting in better distributed stresses and prolonged cycling. Multi-layered alternating electrodeposition of copper and tin was considered as discussed above but impeded by the production of electroless plated copper following deposited tin metal.

3.4.2 225°C 4h Thermal Anneal of Triple Stacked Bilayer Film

The effect of increasing tin content was examined by the fabrication of a 3μm Cu film with increasing thicknesses of Sn; 5.68μm, 6.5μm and 7.5μm. Based on weight, these three films represent a molar ratio of 1.33:1, 1.17:1, and 1:1.04 of Cu:Sn for the 5.68μm, 6.5μm and 7.5μm, respectively. The central portion of each

completed Cu-Sn bilayer film was extracted, divided, and stacked accordingly. Each film was pressed between stainless steel plates and annealed at 225°C under Argon

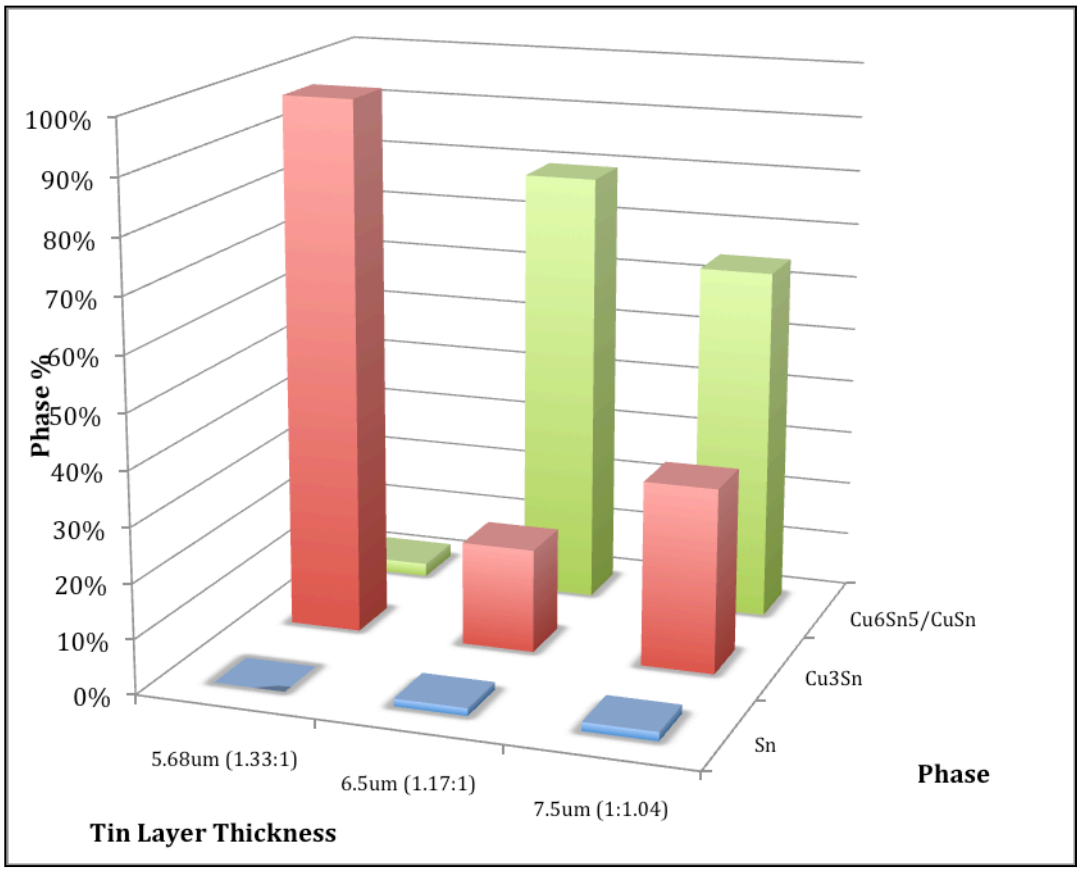

Figure 3-28 Comparison of the XRD phase for the triple stacked bilayer Cu-Sn films annealed at 225°C 4h as a function of Sn content (top surface analysis)

flow for 4h. The final measured densities for the 5.68μm, 6.5μm and 7.5μm stacked films were 8.435 g/cc, 8.231 g/cc, and 8.14 g/cc, respectively.

XRD phase analysis from the top and bottom surfaces of the stacked film revealed pure Sn was present in residual amounts on the order of 1-2% as identified for the 1.17:1 and 1:1.04 molar ratio stacked films and non existent for the 1.33:1 molar ratio as shown in Figure 3-28:29. Diffusion formed the intermetallic phases of

Cu_3Sn and Cu_6Sn_5/CuSn. The 1:1.04 molar ratio films were dominated by the Cu_6Sn_5/CuSn phase ranging from 65-71% and contained 28-34% Cu_3Sn. Similarly, the 1.17:1 molar ratio films had lower amounts of Cu_3Sn (19-43%) and dominance of the Cu_6Sn_5/CuSn phase (57-80%). As expected, the 1.33:1 molar ratio films contained 94-98% Cu_3Sn and small amounts of Cu_6Sn_5/CuSn, 2-6%. The alloy complexity is shown in Figure 3-30 for the 1.17:1 molar ratio stacked film top and bottom investigations. Figure 3-31 shows the results of the XRD analysis for the bottom surface of the films. XRD of the bottom surface of the stacked films reveals the domination by the pure Cu phase for all three ratios at roughly 50%, followed by

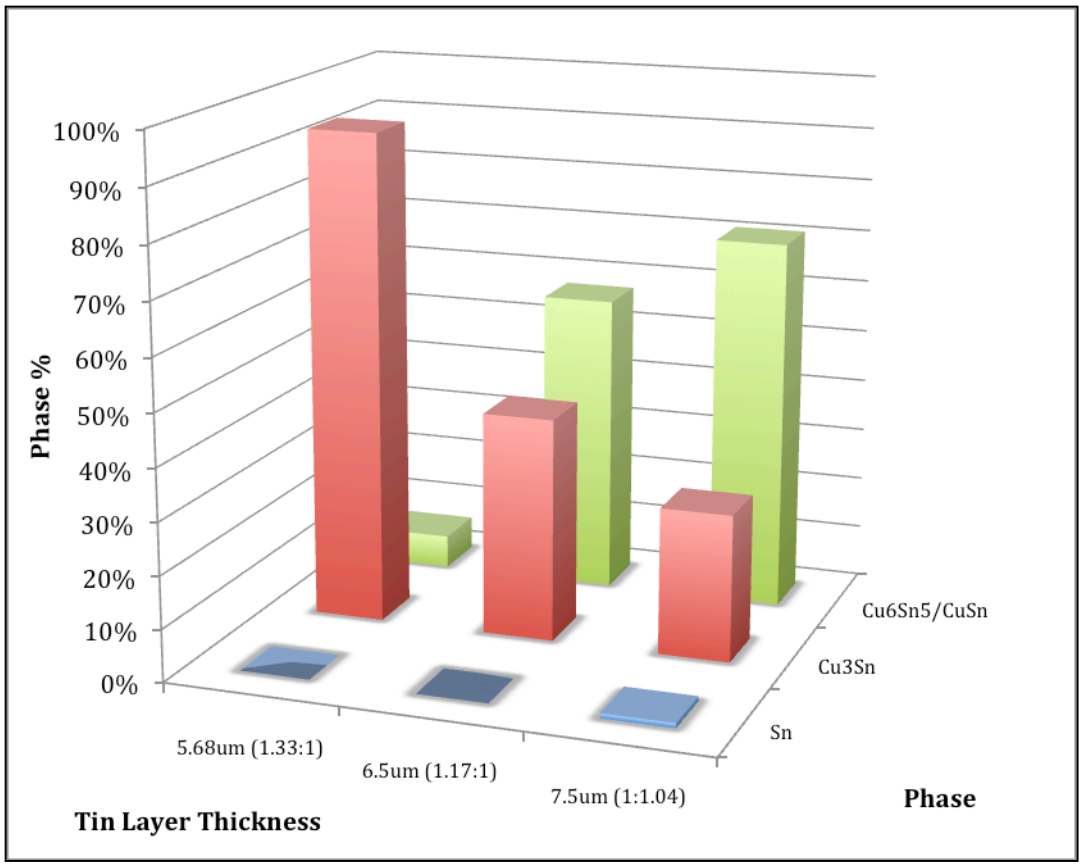

Figure 3-29 Comparison of phases as determined by XRD for the triple stacked bilayer Cu-Sn films annealed at 225°C 4h cycled with 1.3V cutoff (top surface analysis).

the intermetallic phase, Cu_3Sn. In combination with the top surface XRD results, it is

concluded that much improved distribution of Cu is achieved from the alternating bimetal design due to the lack of pure tin. The additional pure copper only present in the bottom of the triple stacked film provides a built-in current collector for the electrode, which from the commercial standpoint, can be beneficial in maximizing cell design space. The Cu is only present on the bottom of the triple stack as it is the only copper layer not bordered on both sides by a corresponding layer of Sn.

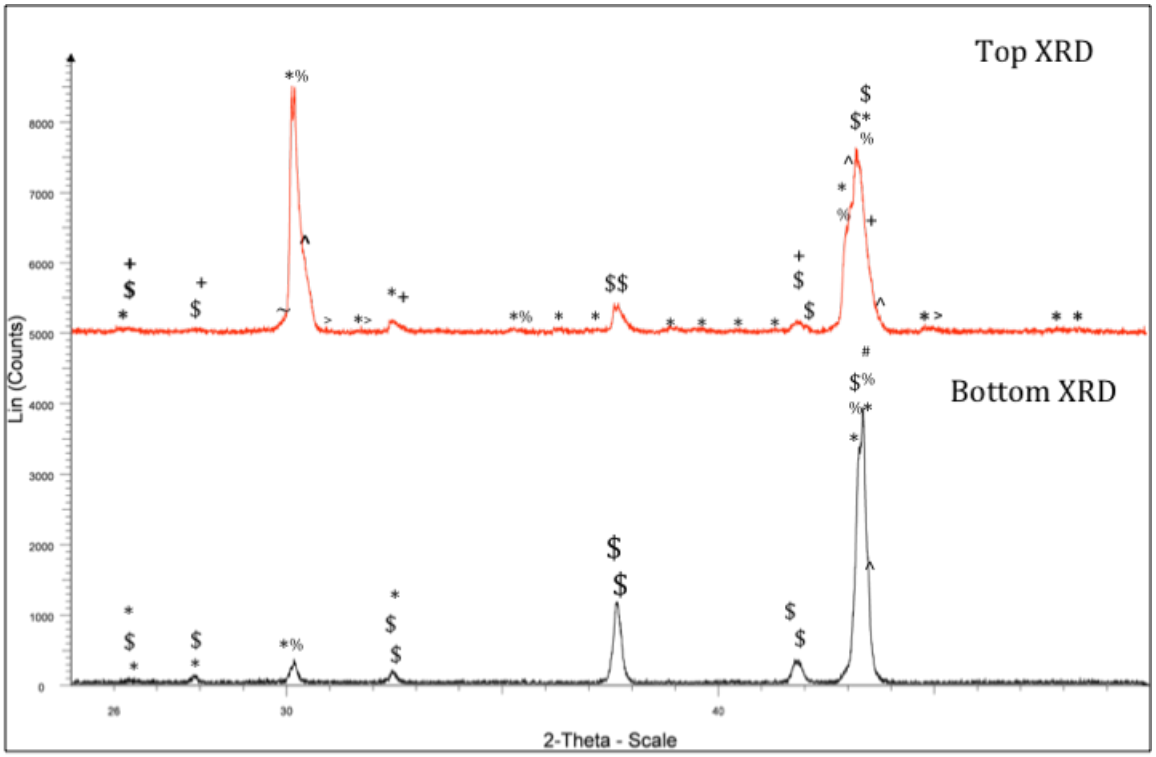

Figure 3-30 The phases of the 6.5µm triple stacked film (top and bottom surface analysis) identified as: Cu_6Sn_5 (*), Cu_6Sn_5' (^), $Cu_{3.02}Sn_{0.98}$ ($), Cu_3Sn (+), CuSn (%), Sn (>), SnO (~), Cu (#).

Figure 3-29 shows a decreasing trend of the Cu_3Sn phase and increase of the Cu_6Sn_5/CuSn phases with the increase of Sn molarity of the triple stacked films. All molar ratios showed the existence of minimal pure tin following the anneal heat

treatment. This confirms the stacking of thinner films successfully combined the pure copper and tin phases to produce the maximum amount of alloy phases for each of the film thicknesses. The theoretical molar ratios for Cu_3Sn, Cu_6Sn_5, and CuSn are 1.63:1, 1:1.56, and 1:1.86, respectively. Their coinciding theoretical densities are 8.348g/cc, 7.989g/cc, and 7.922g/cc, accordingly. When the pycnometer-measured densities of the stacked films were compared to these values

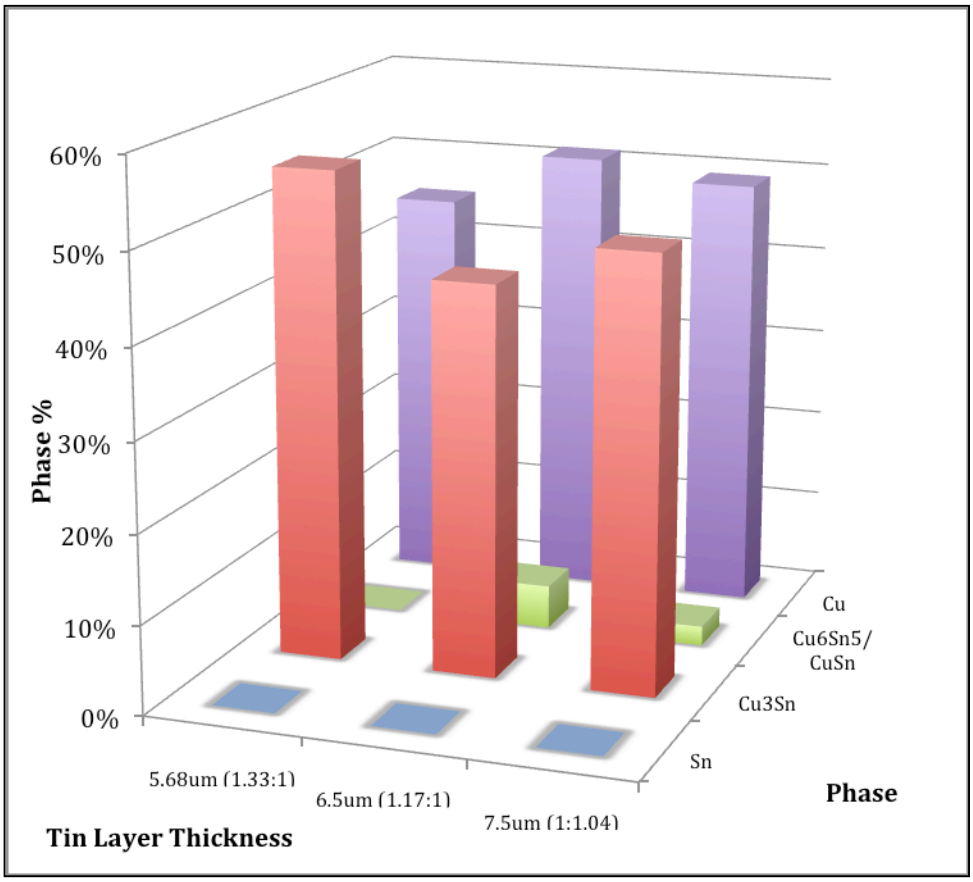

Figure 3-31 XRD phase analysis for the triple stacked Cu-Sn films (bottom surface analysis).

and the XRD compositional analysis, the trending increase of the Cu_6Sn_5/CuSn phase with the increase of deposited tin per layer is supported.

The theoretical x-ray penetration depth as a function of molar ratio was calculated to shed insight on the relevance of the XRD data. Tables 3-16:17 examine the calculated x-ray penetration depth for each film. It is determined that as the tin layer increases, the composite densities and x-ray penetration depth decreases. It was concluded that the x-rays easily penetrate the majority of the top bilayer film in each of the stacks. As Cu diffuses into the Sn layer, our XRD data is well representative of the amount of Sn that has converted to the intermetallic phases.

Table 3-16 X-ray penetration depth based on single direction for triple stacked films utilized with the 2V cycling cutoff.

Film	Molar Ratio (Cu:Sn)	Calculated X-ray Penetration Depth	Film Thickness	Percent Film by XRD
5.68μm	1.33:1	8.44μm	20μm	42%
6.5μm	1.17:1	7.86μm	25μm	31%
7.5μm	1:1.04	7.27μm	30μm	24%

Table 3-17 Single direction x-ray penetration depth analysis for triple stacked Cu-Sn films utilized with the 1.3V cutoff cycling.

Film Tin Layer Thickness	Molar Ratio (Cu:Sn)	Calculated X-ray Penetration Depth	Total Film Thickness	Percent Film by XRD
5.68μm	1.33:1	8.44μm	15 μm	56%
6.5μm	1.17:1	7.86μm	20 μm	39%
7.5μm	1:1.04	7.27μm	30 μm	24%

3.4.3 Cross Section Analysis

Phase and morphological distribution of each stacked bilayer film was provided by the cross-sectional analysis via FESEM microscopy. Figures 3-32:34 details the copper and tin distribution throughout the 7.5μm (1:1.04), 6.5μm (1.17:1), and 5.68μm (1.33:1), respectively. The elemental analysis for each of the films confirms the copper layer of the top two bilayers has been completely

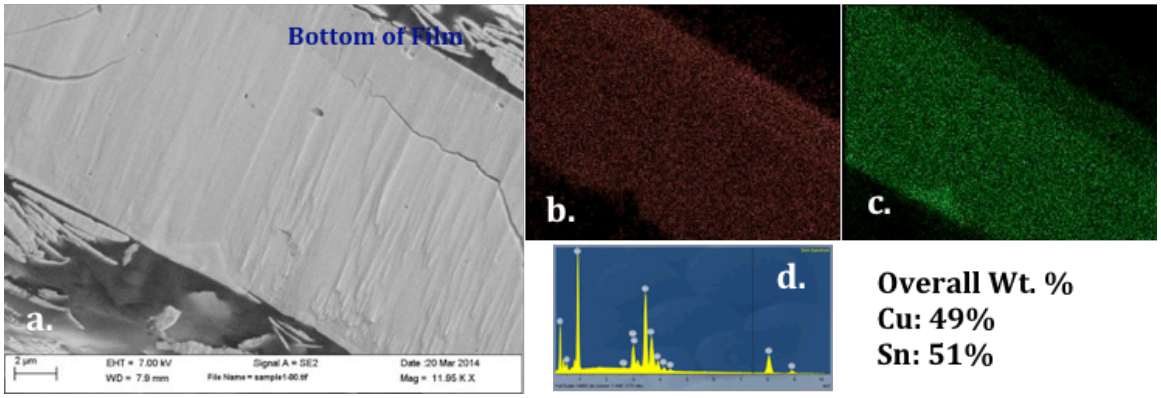

Figure 3-32 FESEM & EDS images and spectrum for the triple stacked 7.5μm bilayer film (1:1.04 molarity). a.) Secondary electron image detailing cross-sectional view of stacked film; b.) EDS of copper content; c.) EDS of tin content; d.) Spectra results for 7.5μm triple stacked bilayer film.

transformed so the only copper dominant area remaining for the annealed film is a small portion of the underside bottom bilayer. This is consistent with the aforementioned fact that the bottom Cu is not bordered on both sides by Sn to diffuse into. A distinct boundary for each of the intermetallic phases was not observable in comparison to the FESEM and EDS images of the thick single bilayer films seen in Figure 3-27. Further investigations of the spectra collected during EDS helped determine the overall copper and tin content for each film. The measured molar ratio for each film was 1:1.04, 1:1.17, and 1.86:1 for the 7.5μm, 6.5μm, and 5.68μm, respectively. These values were slightly different from the derived values

from the pycnometer analysis of 1:1.04, 1.17:1, and 1.33:1 for 7.5µm, 6.5µm, and 5.68µm, respectively, and the targeted theoretical molar ratio for Cu_6Sn_5, 1:1.56. Differences in the values are attributed to variations within the film from inhomogeneities of the electrodeposition process 'y' direction and phase distribution.

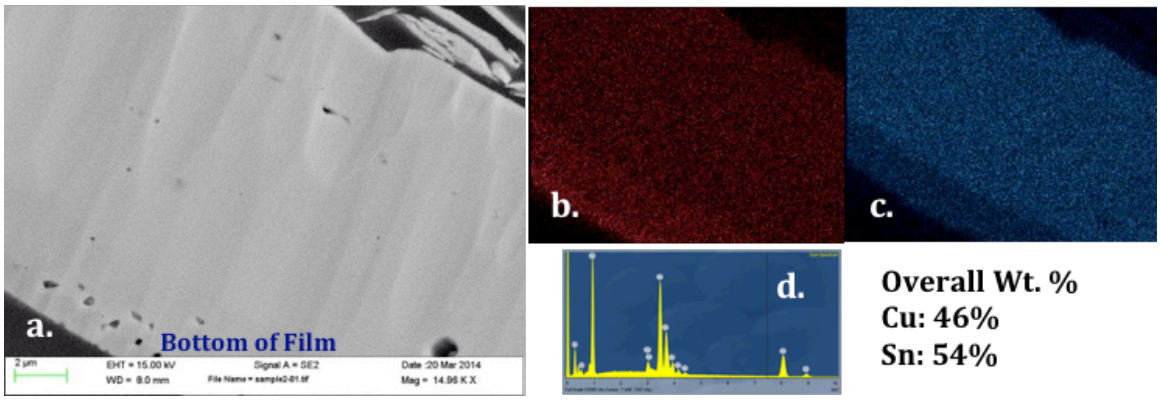

Figure 3-34 FESEM & EDS images and spectrum for the triple stacked 6.5µm bilayer film (1.17:1 molarity). a.) Secondary electron image detailing cross-sectional view of stacked film; b.) EDS of copper content; c.) EDS of tin content; d.) Spectra results for 6.5µm triple stacked bilayer film.

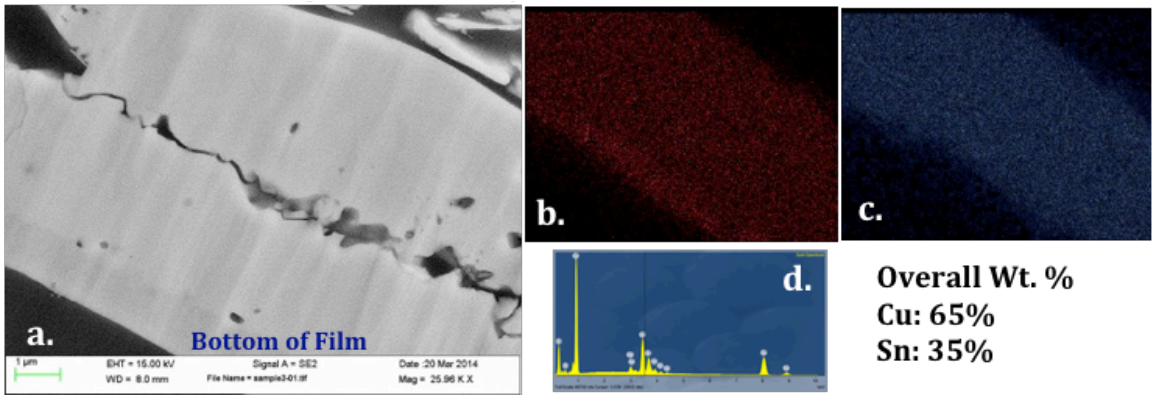

Figure 3-33 FESEM & EDS images and spectrum for the triple stacked 5.68µm bilayer film (1.33:1 molarity). a.) Secondary electron image detailing cross-sectional view of stacked film; b.) EDS of copper content; c.) EDS of tin content; d.) Spectra results for 5.68µm triple stacked bilayer film.

3.4.4 Electrochemical Investigations For Triple Stacked Bilayer Films

The fabricated films were tested for their electrochemical activity utilizing the two protocols described in Table 3-18. Protocol 1 examines the cycling stability with a delithiation cutoff of 2V while protocol 2 utilizes a lower cutoff of 1.3V. Figure 3-35 and 3-36 show the capacity as a function of cycle number for the 2V and 1.3V cutoffs, respectively. Two capacity plots are shown for each protocol based on the volumetric capacity of the entire composite film inclusive of the copper metal and also the electrodes' areal capacities. For the 2V cutoff, the molar ratio of 1.17:1 had the best cycling with good retention to approximately 40 cycles. The volumetric capacity approaches 1400mAh/cc even at a relatively high areal capacity in the range of 2-3mAh/cm^2.

Table 3-18 Cycling protocols utilized for the electrochemical evaluation of the copper-tin deposited films.

Protocol	Voltage	Applied Current
1	0.01-2V	15mA/g (First 1.5 Cycles) 30mA/g (Remaining Cycles)
2	0.01-1.3V	15mA/g (First 1.5 Cycles) 30mA/g (Remaining Cycles)

In general, the 1.3V cutoff (Fig. 3-36) resulted in improved cycling stability for all compositions, consistent with findings by Beattie and Dahn [74]. More specifically, there was a marked improvement in the larger Sn molar ratio film of 1:1.04. The Cu:Sn molarity and electrochemical protocol impact on the electrochemical performance was further analyzed as shown in Table 3-19 and

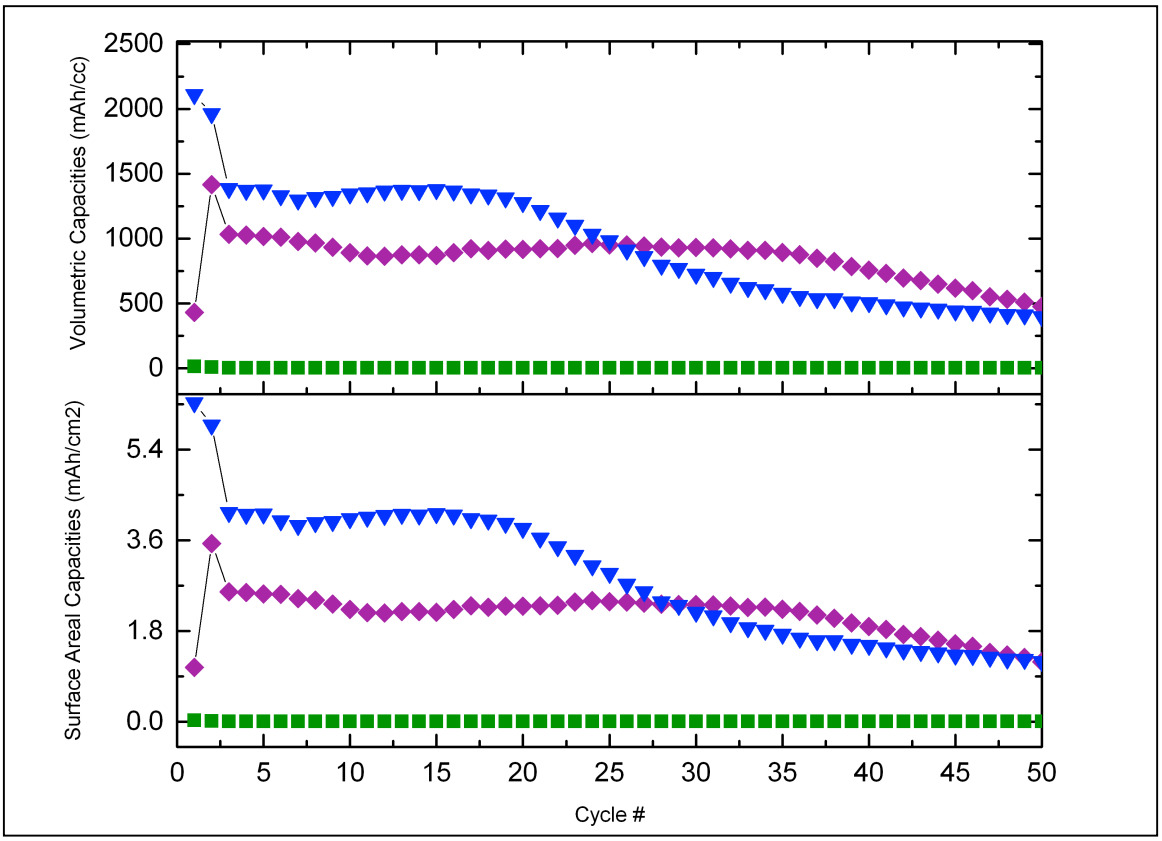

Figure 3-35 Electrochemical analysis of triple stacked bilayer films for the first 50 cycles utilizing 2V cutoff cycling. ■ -(1.33:1) molar ratio; ◆ - (1.17:1) molar ratio; ▼ - (1:1.04) molar ratio.

Table 3-20. From this data, it can be concluded that the compositional makeup of the 5.68μm bilayer stacked film (Cu:Sn molar ratio of 1.33:1) was unfavorable and produced the highest irreversible losses during the first cycle of 67% and 58% for Protocol 1 and 2, respectively. The best composition for producing the lowest

irreversible losses (21%) and highest capacity (1525 mAh/cc and very high 4.57 mAh/cm^2) was generated from the 7.5μm triple stacked bilayer films (1:1.04) cycled with the lower cutoff voltage of 1.3V. This is supported by low onset reactivity during the early voltage profiles seen in Figure 3-37. Figure 3-38 provides the direct comparison of the lithiation and delithiation capacities for the 1:1.04 molar ratio

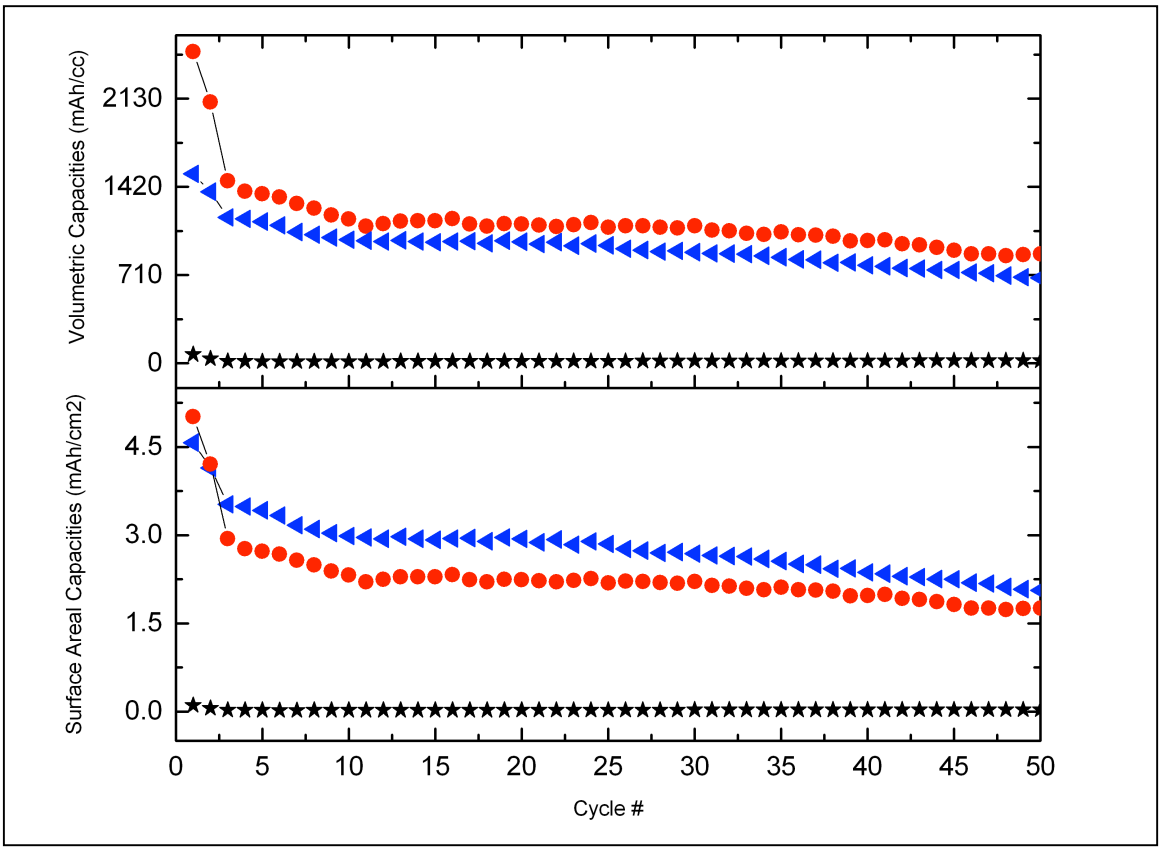

Figure 3-36 Electrochemical analysis of triple stacked bilayer films first 50 cycles utilizing 1.3V cycling cutoff. ★ – (1.33:1) molar ratio; ● - (1.17:1) molar ratio; ◀ - (1:1.04) molar ratio.

stacked film cycled with this cutoff showing good efficiencies after the first two cycles. It should be noted that the analysis was carried out using a standard electrolyte composition of $LiPF_6$ EC:DMC and much improvement in efficiencies can

be brought about by the select use of additives. However, this was not the focus of the present communication.

Table 3-19 Electrochemical analysis of the first 1.5 cycles for the triple stacked Cu-Sn films cycled utilizing the 2V cutoff. Included is the comparison are the initial irreversible loss defined as first lithiation/delithiation difference

Films (Cu:Sn)	1st Lithiation		1st Delithiation		2nd Lithiation		Irreversible Loss %
	mAh/cc	mAh/cm²	mAh/cc	mAh/cm²	mAh/cc	mAh/cm²	
5.68 µm (1.33:1)	16	0.03	5	0.01	10	0.02	67%
6.5 µm (1.17:1)	431	1.08	412	1.03	1415	3.54	4%
7.5 µm (1:1.04)	2109	6.33	1085	3.26	1962	5.89	49%

Table 3-20 Electrochemical results for the first 1.5 cycles of the triple stacked Cu-Sn films cycled with the 1.3V cycling cutoff. Irreversible loss is defined as difference in first lithiation/delithiation.

Films (Cu:Sn)	1st Lithiation		1st Delithiation		2nd Lithiation		Irreversible Losses %
	mAh/cc	mAh/cm²	mAh/cc	mAh/cm²	mAh/cc	mAh/cm²	
5.68 µm (1.33:1)	71	0.11	29	0.04	38	0.06	58%
6.5 µm (1.17:1)	2508	5.02	1503	3.01	2102	4.20	40%
7.5 µm (1:1.04)	1525	4.57	1196	3.59	1381	4.14	21%

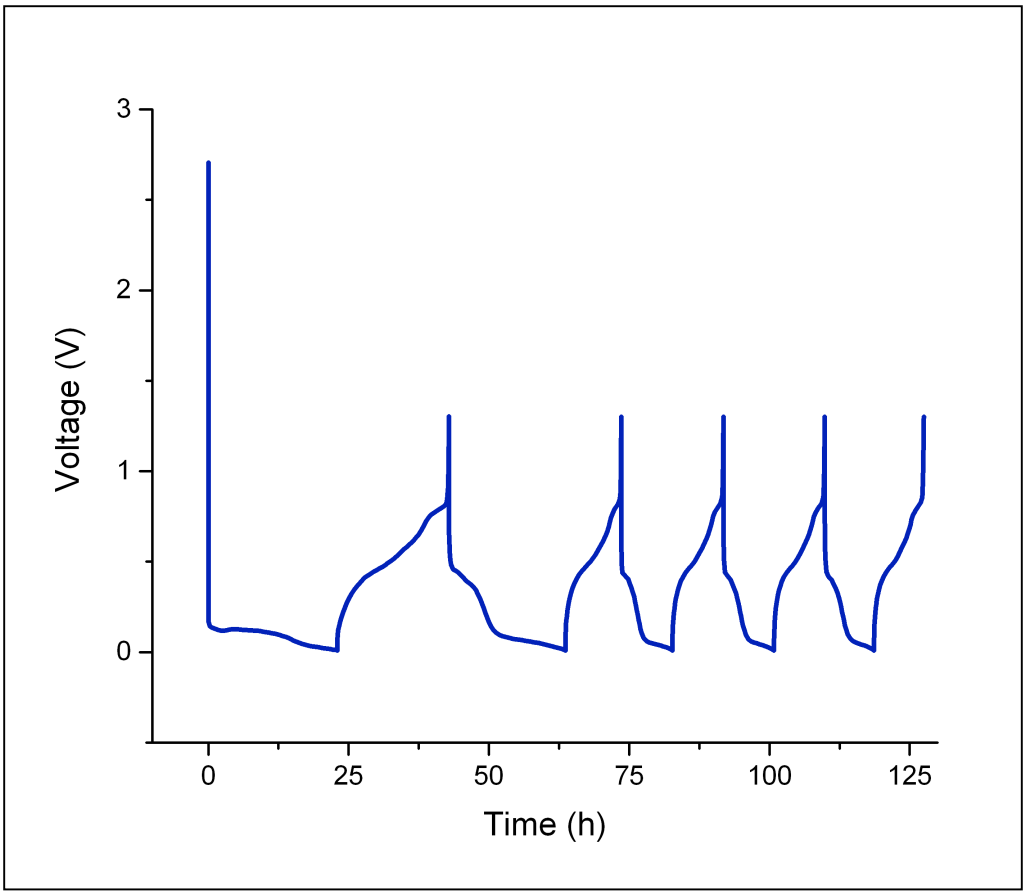

Figure 3-37 Voltage vs. time profiles for the first 5 cycles of the 1:1.04 molar ratio (7.5μm) stacked film with 1.3V cutoff.

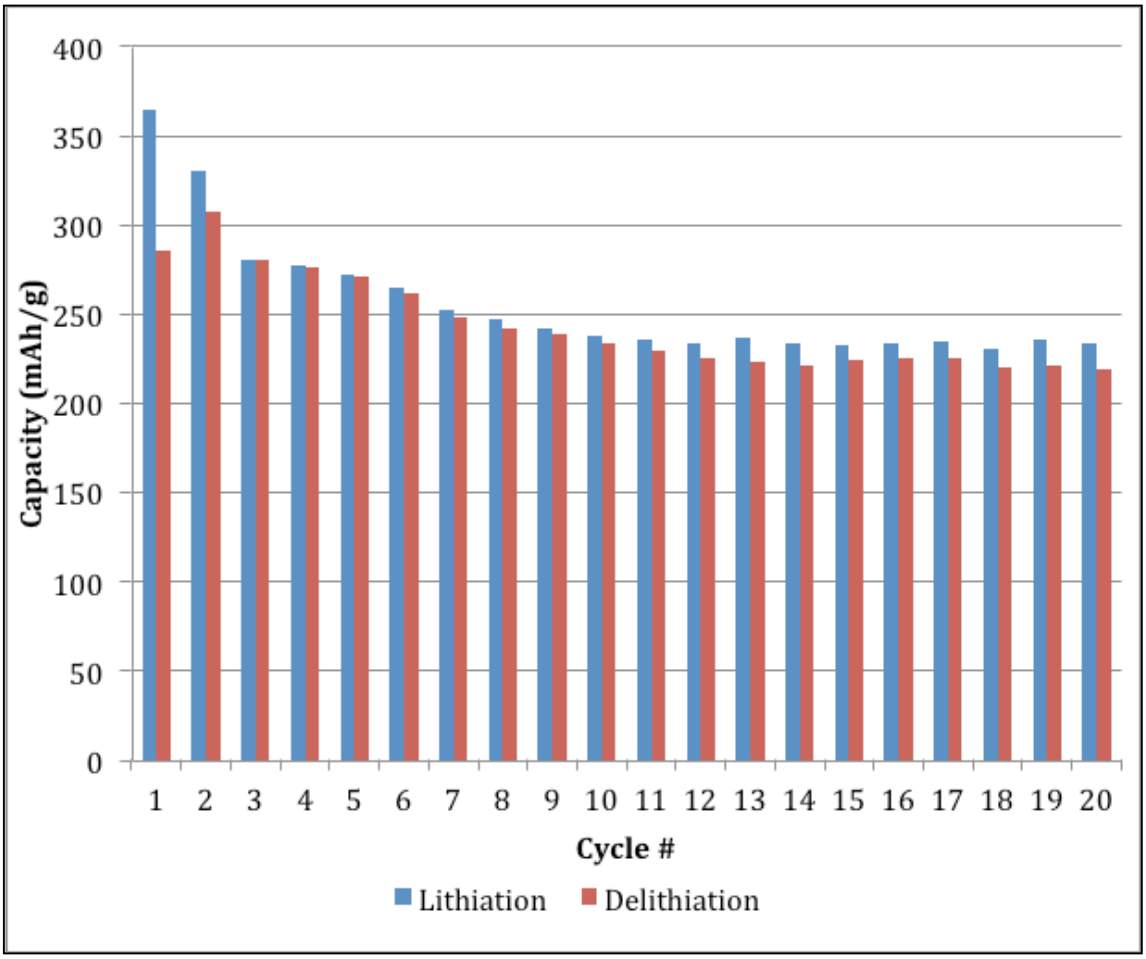

Figure 3-38 Charge-discharge efficiencies for the 7.5µm (1:1.04 molarity) triple stacked film depicted by the comparison of lithiation and delithiation capacities for the 1.3V cycling cutoff.

The relationship of film Cu:Sn molarity to electrochemistry for the 6.5µm (1.17:1) and 7.5µm (1:1.04) films are slightly unclear with similar capacity retention, volumetric and surface areal capacities. Comparisons of electrochemistry and compositions do not show a direct trend leading to an overall better film, but it should be noted that phase analysis revealed similar distributions. As such, the combined data suggests that the creation of a composition with the dominant phase of Cu_6Sn_5/CuSn and limitations to the pure Sn phase and intermetallic, Cu_3Sn,

produces the best results. This is confirmed by the results of 6.5μm (1.17:1 Cu:Sn ratio) for delithiation cutoff of 2V and 7.5μm (1:1.04 Cu:Sn ratio) for delithiation cutoff 1.3V.

3.4.5 Conclusions

The triple stacked heat treatment design for the freestanding films successfully increased the phase transformations for superior cycling capabilities comparable and/or better than past research. The described films obtained volumetric and surface areal capacities above 1000mAh/cc and 2.5mAh/cm^2, respectively. In addition, this fabrication process subsequently produced a unique freestanding film with a combined current collector and electrode, eliminating the requirement for additives and fillers typically used in commercial production.

3.5 Surface Coatings For Electrochemical Enhancement

3.5.1 ALD coatings

Atomic layer deposition (ALD) has been utilized to improve the stability during the formation of the SEI layer for decreased irreversible loss during initial cycling and prolonged retention for electrode materials such as graphite, and $Li_4Ti_5O_{12}$ [79,80,81,82]. The film chosen for the Cu-Sn films was alumina coating of 15nm and 5nm thicknesses. These deposited surface coatings were applied to the triple stacked 7.5μm films heat treated at 225°C 4h. Due to the small amount of alumina on the surface of the films, x-ray analysis did not show any alterations in the film composition due to this addition. The general composition of the 7.5μm film

was approximately: 1-2% Sn; 22-28% Cu_3Sn; 65-76% Cu_6Sn_5/CuSn. Figure 3-39 compares the electrochemistry of the standard film with the films with alumina surface coatings. From this data it can be seen that the ALD coatings did not have the projected beneficial characteristics as proposed. The 15nm ALD film was determined to be too thick due to its poor cycling characteristics and extremely low capacities. This is caused by the surface coating completely insulating the electrode due to the thickness of the coating exceeding the allowable diffusion distance of the

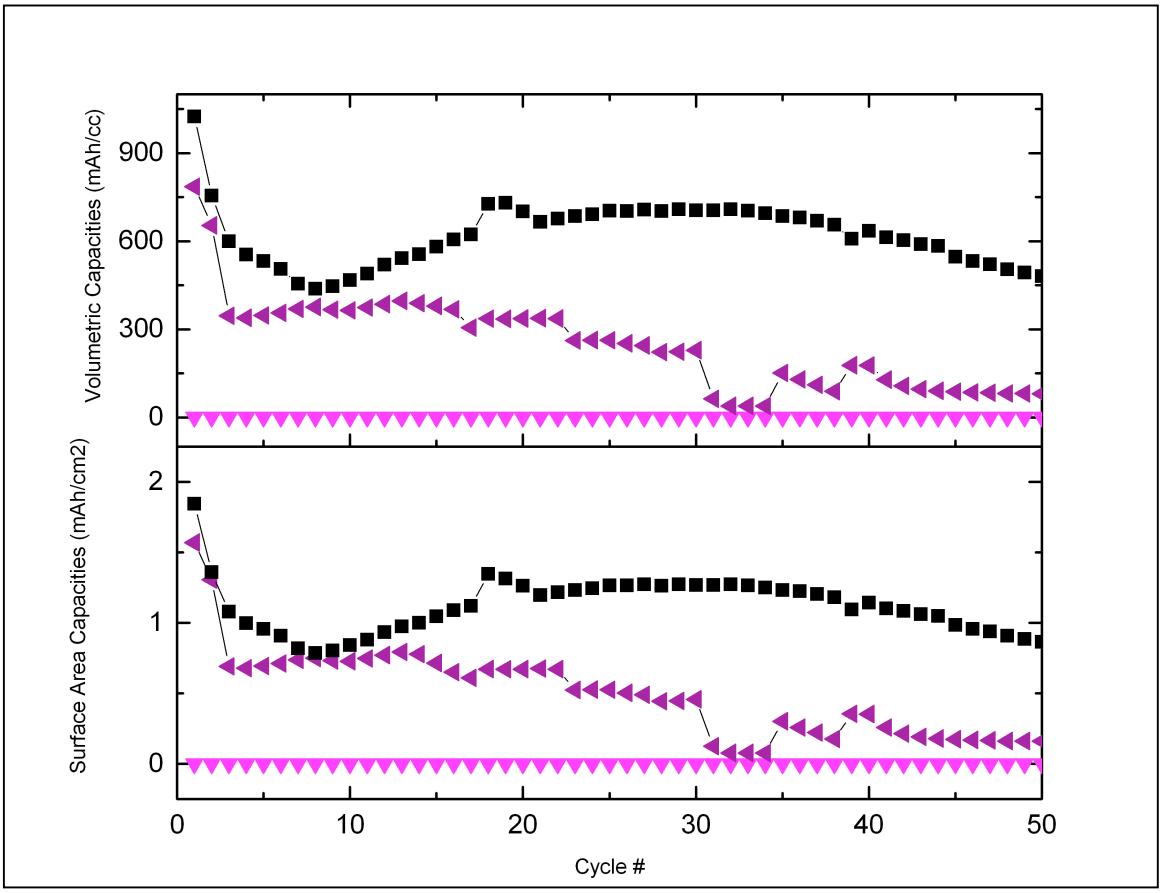

Figure 3-39 Areal lithiated capacities comparison for films with ALD alumina surface coatings. ■: standard triple stacked 7.5micron film; ◀: 7.5micron triple stacked film with 5nm ALD coating; ▼: 7.5micron triple stacked film with 15nm ALD coating.

lithium ions. The 5nm ALD coating allowed for improvements in the initial irreversible loss but however further cycling of the material presented increased failure by the 20th cycle. Overall, the standard material without the ALD coatings had superior cycling capabilities. At this time, it is not completely certain if the ALD coatings chemically or physically caused earlier failure within the 7.5micron triple stacked films. Visual observations of all the films with ALD coatings showed increased fragility, which could of played a role in films cycling retention.

3.5.2 LiPON coatings

Solid electrolyte surface coatings such as LiPON have been added to electrode materials to improve their cycling stability. The surface coating assists in reducing the interaction of the electrolyte with the electrode material, leading to reduced production of the solid electrolyte interface (SEI layer). Two thicknesses were investigated with the triple stacked 7.5micron film annealed at 225°C 5h: 250nm and 20nm. The general composition of the 7.5micron triple stacked film annealed at 275°C 5h was: 3-6% Sn; 0% Cu_3Sn; 94-97% Cu_6Sn_5/CuSn. The extreme thickness differences were used to examine if the surface coating could cause the electrode material to become completely insulated from lithiation. Figure 3-40 reviews the electrochemical results for the LiPON coated films with a standard 7.5micron triple stacked film.

As expected the thickness of the LiPON coating played a crucial role in the cycling capabilities of the triple stacked 7.5micron film. The 250nm LiPON coating thickness exceeded the allowable diffusion capabilities of the lithium ions and

therefore was unsuccessful in providing electrochemical enhancement of the Cu-Sn film. This resulted in low areal capacities just above 0mAh/cc and 0mAh/cm^2.

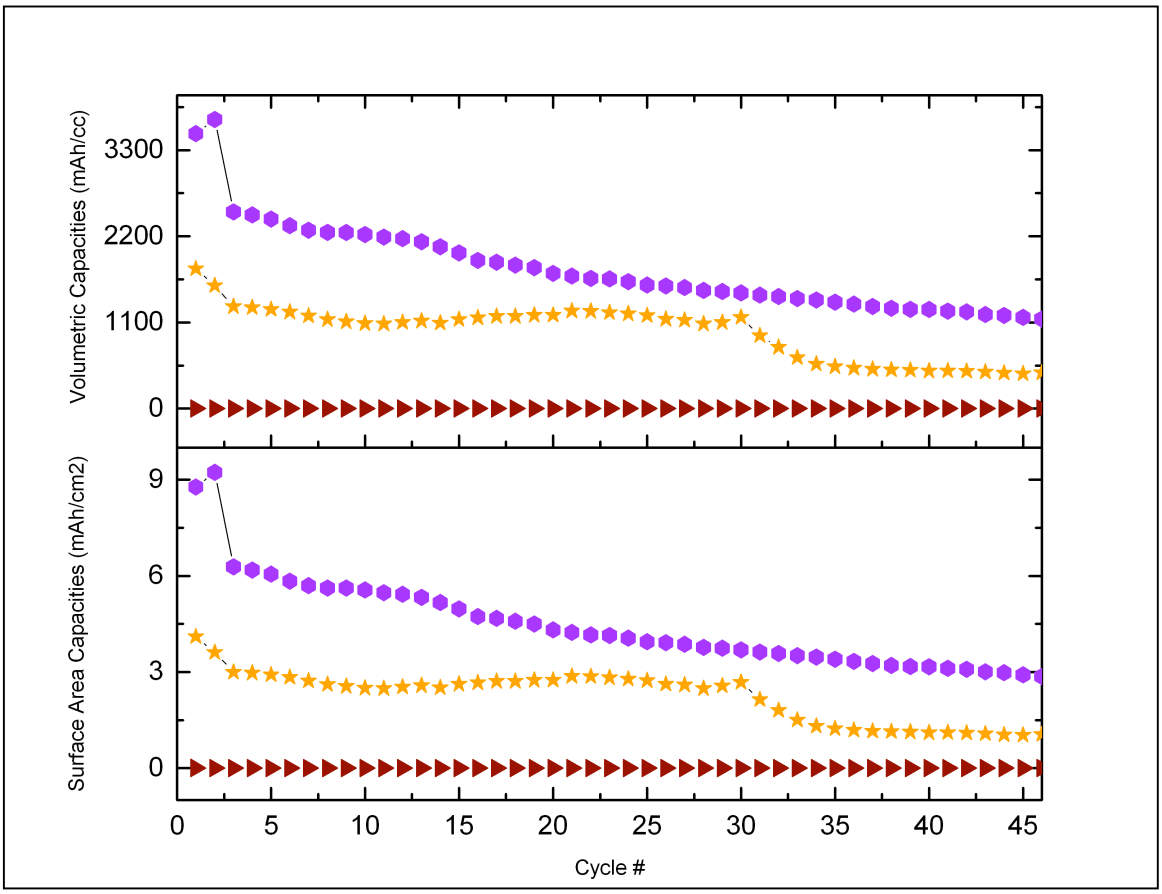

Figure 3-40 Electrochemical comparison of the LiPON coated triple stacked 7.5micron films with a standrad 7.5micron triple stacked film. ⬢: 20nm LiPON coated triple stacked 7.5micron film; ★: standard triple stacked 7.5micron film; ▶: 250nm LiPON coated triple stacked 7.5micron film.

However, the 20nm LiPON coating showed much improvement in the volumetric and areal capacities (approximately 2200mAh/cc and 6mAh/cm^2) and capacity retention in comparison to the standard 7.5micron triple stacked film (1100mAh/cc and 3mAh/cm^2). Further analysis is seen in the electrochemical comparisons in Table 3-21. For these results it can be seen that the 20nm LiPON experienced large irreversible losses (initial 58%) with each ensuing cycle, leading to the deterioration of the film over time. The subsequent lithiation cycles for the 20nm LiPON film

continually proceed with high capacities, which are attributed to new exposed active material.

Table 3-21 Electrochemical comparison of the 20nm LiPON coated and standard triple stacked 7.5micron film 225°C 4h. The irreversible loss is the difference in 1st lithiation and delithiation.

Films (Cu:Sn)	1st Lithiation		1st Delithiation		2nd Lithiation		Irreversible Losses %
	mAh/cc	mAh/cm²	mAh/cc	mAh/cm²	mAh/cc	mAh/cm²	
Standard 7.5µm film	1786	4.11	1489	3.43	1570	3.61	17%
20nm LiPON	3511	8.78	1465	3.66	3692	9.23	58%

3.5.3 Conclusions

Surface coatings can be added to electrode materials to help improve upon the interaction of the active material with the electrolyte. From the data collected thus far, it has been determined that the ALD alumina coatings are not beneficial for electrochemical enhancement of the Cu-Sn freestanding films. At this time, the ALD process is believed to weaken the structural integrity of the films and therefore inhibiting the true effects of the coatings. The LiPON coatings (20nm) were found to have some improvements on the capacity retention of the triple stacked Cu-Sn films. But however, the increased irreversible losses incurred with each cycle are undesirable and may need further investigations for improvements in the future. Therefore, it has been concluded that both the LiPON and ALD coatings have not been successful moving forward in this research.

3.6 Electrochemical Modifications with Electrolyte Additives

Additives to the electrolyte have been utilized to manipulate the chemistry of the SEI formation during lithiation to produce a more stable layer during cycling. As discussed previously in an earlier chapter, vinyl carbonate (VC) and fluoroethylene carbonate (FEC) are commonly used additives [83,84]. Other modifications that can alter the electrolyte include the substitution of Dimethyl Carbonate (DMC) with Ethyl Methyl Carbonate (EMC).

3.6.1 FEC & VC Additives

Electrochemical investigations for the Cu-Sn triple stacked films included the testing of FEC and VC additives (5vol% and 10vol%). The additives were added to the standard electrolyte, 1M $LiPF_6$ EC:DMC (50vol%:50vol%). These additives were examined for the Cu-Sn triple stacked 7.5μm film heat-treated at 225°C 5h. The general phase composition for this film was: 3-6% Sn; 0% Cu_3Sn; 94-97% Cu_6Sn_5/CuSn. The electrochemical results for the FEC additives are seen in Figure 3-41. From this data it can be determined that the addition of 5vol% FEC actually had negative effects on the cycling of the Cu-Sn film as seen in its poor cycling (500mAh/cc and (1mAh/cm^2). The addition of 10vol% FEC showed some increase in capacity in the early stages of cycling but by the 10th cycle had equal or less capacity than the standard cycling Cu-Sn film. A more detailed description of the early electrochemical characteristics of the 10vol% FEC and standard Cu-Sn film are

seen in Table 3-22. From these results it can be concluded that although the Cu-Sn film cycled with the FEC 10vol% additive had higher capacities, ultimately the associated irreversible loss (51%) was also higher leading to lower cycle life.

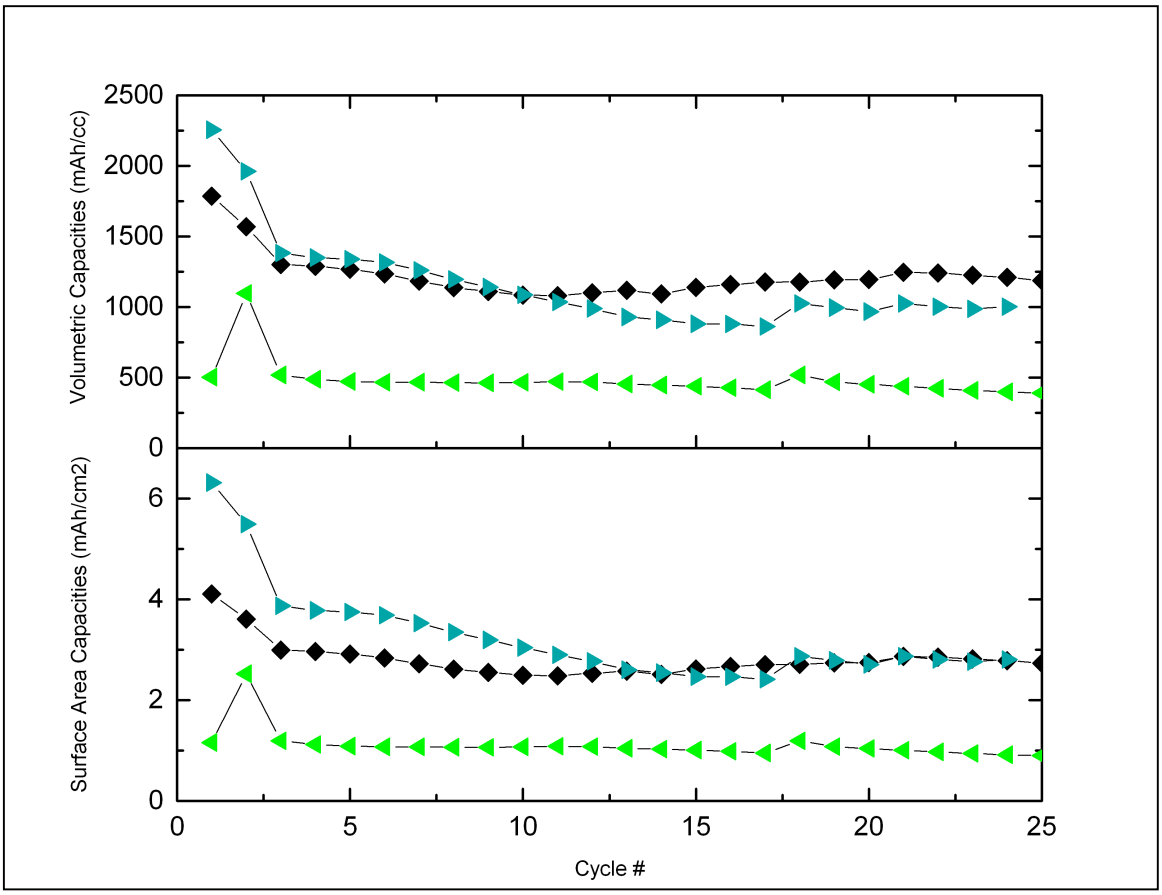

Figure 3-41 Electrochemical analysis of the areal lithiated capacities for FEC additives (5vol% & 10vol%). ◆: standard 1M $LiPF_6$ EC:DMC (50vol%:50vol%); ◀: 5vol% FEC additive; ▶: 10vol% FEC additive.

Table 3-22 Electrochemical data for the initial 1.5 cycles including irreversible loss for the 10vol% and standard cycled Cu-Sn films.

Films (Cu:Sn)	1st Lithiation		1st Delithiation		2nd Lithiation		Irreversible Losses %
	mAh/cc	mAh/cm²	mAh/cc	mAh/cm²	mAh/cc	mAh/cm²	
Standard 7.5µm film	1786	4.11	1489	3.43	1570	3.61	17%
10vol% FEC	2257	6.32	1100	3.08	1961	5.49	51%

Similar investigations were also carried out for the Cu-Sn triple stacked

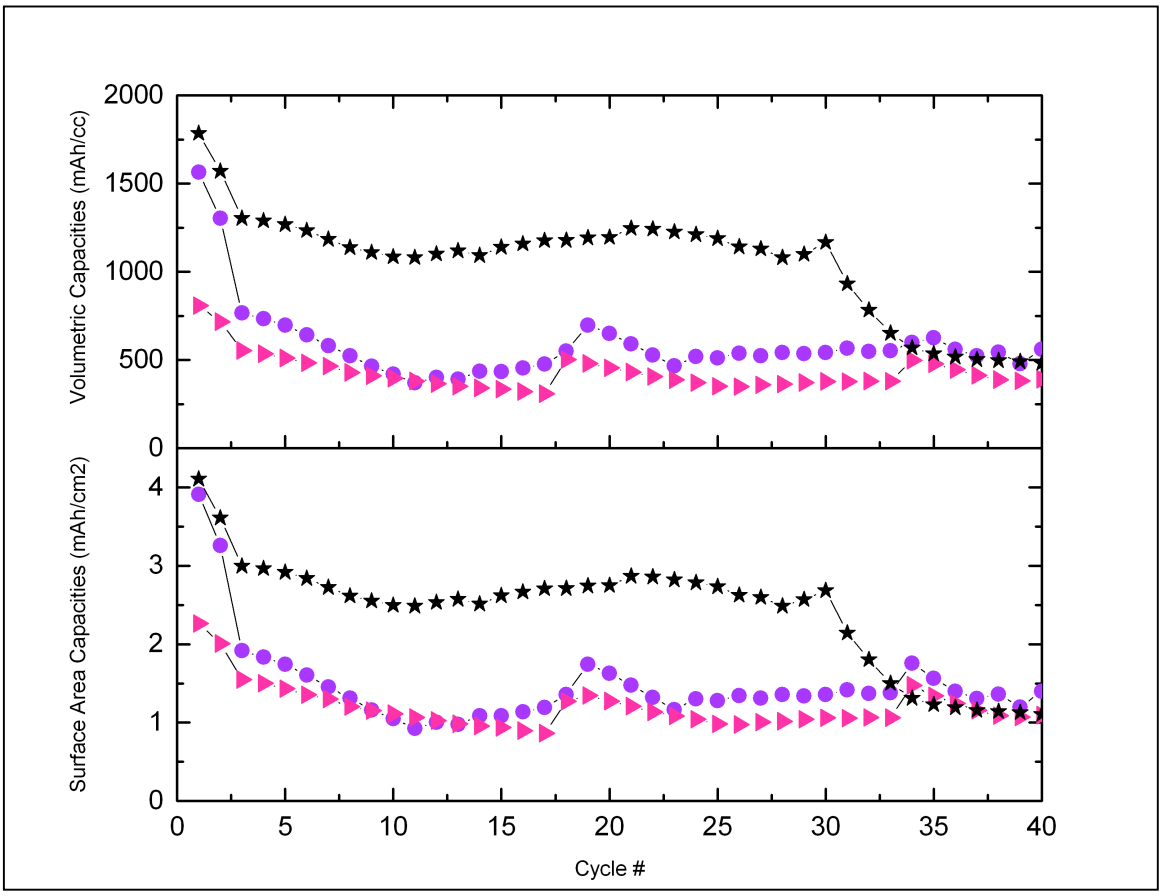

Figure 3-42 Electrochemical analysis of the VC additives 5vol% and 10vol% compared to the standard LiPF6 ED:DMC electrolyte. ★: standard cycling with 1M $LiPF_6$ EC:DMC; ●: 10vol% VC additive; ▶: 5vol% VC additive.

7.5μm film heat-treated at 225°C 5h with the cycling of 5vol% and 10vol% VC additives. The areal lithiated capacities are examined in Figure 3-42. From this data it has been determined that the VC additives have negative effects on the cycling stability of the Cu-Sn triple stacked films due to their lower values (10vol% VC approximately 500mAh/cc and 5vol% VC was approximately 300mAh/cc). The standard electrolyte with the same Cu-Sn triple stacked films maintained a steady 1250mAh/cc during the same cycles. The initial irreversible losses for the 5vol% VC cycled Cu-Sn film and 10vol% VC cycled Cu-Sn film were 29% and 63% respectively. The initial irreversible loss for the standard electrolyte cycled Cu-Sn film was 17%. These results have helped to conclude that the VC additives do not beneficially affect the cycling properties of the triple stacked Cu-Sn films.

3.6.2 EMC Electrolyte Modification

Investigations of electrolyte modification were also examined for $LiPF_6$ EC:EMC (30vol%:70vol%). Testing was completed for the Cu-Sn triple stacked 7.5μm film annealed at 225°C 4h. The general composition of the 7.5μm film was approximately: 1-2% Sn; 22-28% Cu_3Sn; 65-76% Cu_6Sn_5/CuSn. The electrochemical comparison with the standard electrolyte 1M LiPF6 EM:DMC is described in Figure 3-43. It is seen from this data that the lithiated capacities for the Cu-Sn film cycled with the $LiPF_6$ EC:EMC (30vol%:70vol%) had slightly higher volumetric capacities (1600mAh/cc) for the same amount of cycles. The standard electrolyte cycled Cu-Sn film maintained a steady 1375mAh/cc for the same cycles. The capacity retention from cycles 3-30 for the $LiPF_6$ EC:EMC data was 59% while the $LiPF_6$ EC:DMC data

was 52%. The first 1.5 cycles are examined in Table 3-23. The irreversible loss for

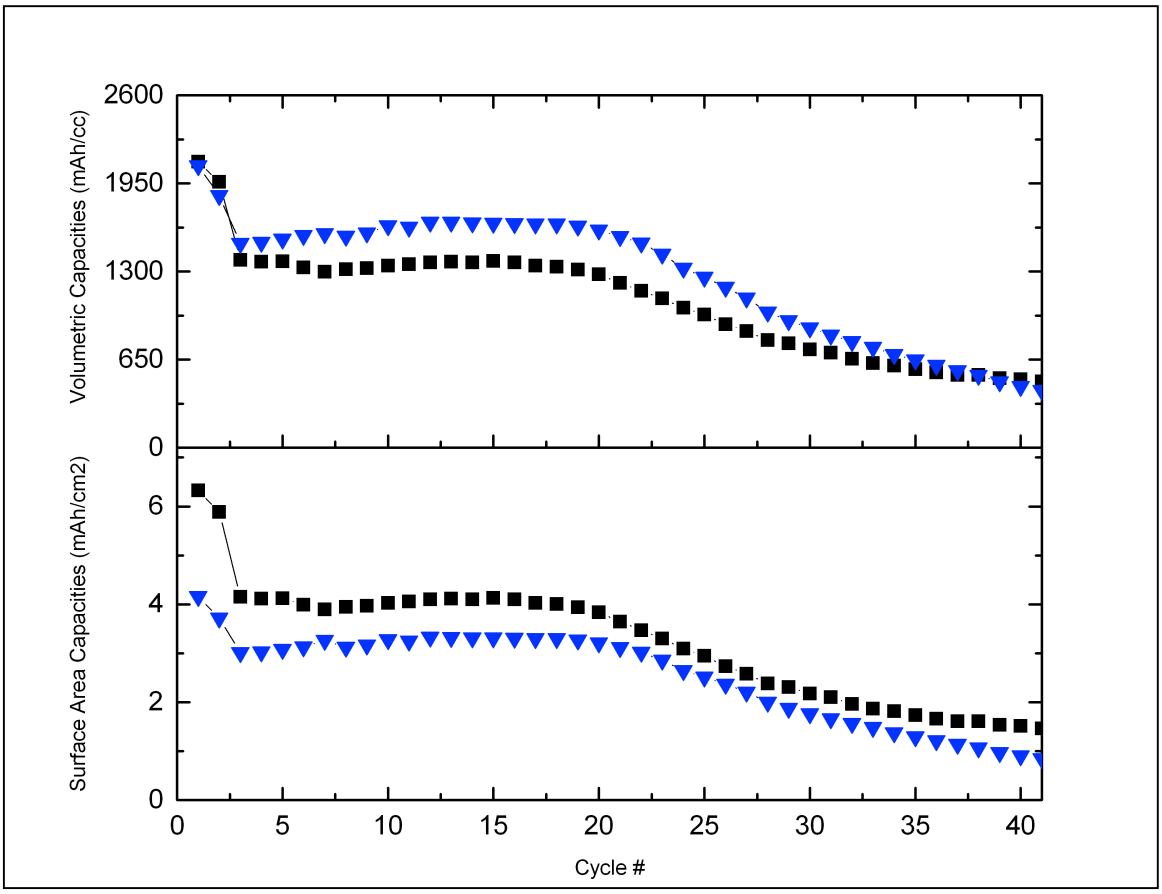

Figure 3-43 Electrochemical analysis of the lithiated areal capacities for the standard electrolyte $LiPF_6$ EC:DMC and modified electrolyte $LiPF_6$ EC:EMC. ■: standard 1M $LiPF_6$ EC:DMC (50vol%:50vol%); ▼: modified 1M $LiPF_6$ EC:EMC (30vol%:70vol%).

the $LiPF_6$ EC:EMC data was -6% due to the increase in capacity during delithiation. This could be caused by the dissolution of lithium ions back into the electrolyte that were trapped during the formation of the SEI layer but have been freed by the volume change stresses fracturing the active material. The standard electrolyte caused the Cu-Sn triple stacked film to undergo high irreversible loss (49%) during the initial cycling of the film. Overall the electrolyte LiPF6 EC:EMC (30vol%:70vol%) was proven to improve the cycling stability of the triple stacked Cu-Sn freestanding

films. This may be attributed to the Ethyl Methyl Carbonate forming more stable SEI components.

Table 3-23 Electrochemical investigation of the first 1.5 cycles comparing the standard electrolyte 1M $LiPF_6$ EC:DMC to the 1M $LiPF_6$ EC:EMC cycling for the triple stacked Cu-Sn films.

Films (Cu:Sn)	1st Lithiation		1st Delithiation		2nd Lithiation		Irreversible Losses %
	mAh/cc	mAh/cm²	mAh/cc	mAh/cm²	mAh/cc	mAh/cm²	
Standard $LiPF_6$ EC:DMC (50%:50%)	2109	6.33	1085	3.56	1962	5.89	49%
$LiPF_6$ EC:EMC (30%:70%)	2079	4.16	2200	4.49	1861	3.72	-6%

3.6.3 Conclusions

The electrolyte additives and modifications were investigated for improvements of the electrochemical properties of the triple stacked Cu-Sn freestanding films. From the data collected it was determined that the FEC and VC additives did not improve the capacity capabilities for the cycling of the Cu-Sn films discussed in this paper. Although some of the additives (10vol% FEC) appeared to increase the early lithiated capacities, further examination proved that the irreversible losses for each of the additives were higher than the described standard electrolyte, 1M $LiPF_6$ EC:DMC. However, the modified electrolyte, $LiPF_6$ EC:EMC (30vol%:70vol%) did have lower irreversible loss and higher retained capacities than the standard electrolyte, which can be caused by the different chemical components of the SEI layer.

3.7 Overall Electrochemical Analysis of Cu-Sn Films

3.7.1 Lithium Uptake & Capacity Analysis For Cu-Sn Films

To determine if the triple stacked Cu-Sn films were reaching their full electrochemical potential a potentiostatic hold test and a capacity cutoff test were implemented. The potentiostatic hold was held at 0.01V to ensure that maximum lithiation was occurring for the films. This examination helped to rule out that deterioration in the capacity retention was not occurring because of the insufficient allowed time for lithium ions to diffuse into the active material. The triple stacked 7.5μm films annealed at 225°C 4h were utilized for this examination. Figure 3-44

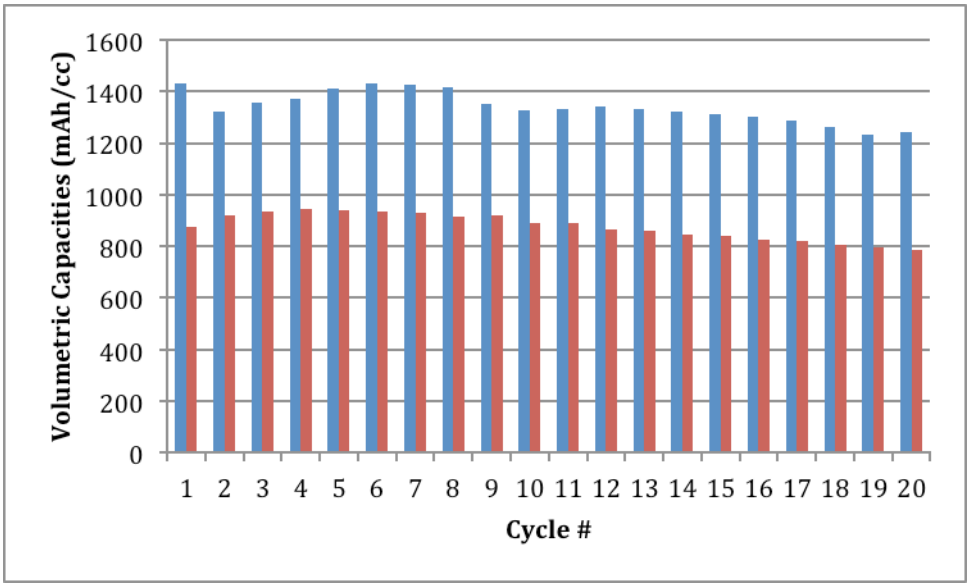

Figure 3-44 Volumetric capacities for the triple stacked Cu-Sn film cycled with a potentiostatic hold. ■: lithiated capacity (mAh/g); ■: delithiated capacity (mAh/g).

shows the volumetric results of cycling during this investigation. The difference in the lithiated and delithiated capacities is the incurred irreversible loss for each cycle. From this data it can be seen that the maximum lithiation capabilities achievable were approximately 1400mAh/cc based on the composite volume of the film. The lithiation and delithiation capacities were not the same however, because of the entrapment of lithium and/or loss of active material during cycling, typically seen for lithium alloying materials. Based on tin volume, the achieved maximum volumetric capacity was 4400mAh/cc (theoretical value: 7316mAh/cc). This helped in determining that the Cu-Sn triple stacked 7.5μm films heat-treated at 225°C 4h were able to lithiate 60% of their total tin content.

The cycle life of the Cu-Sn triple stacked 7.5μm films (225°C 5h) were tested with a capacity cutoff to simulate controlled commercial cycling of the negative electrode material. The established cutoff was 3mAh/cm^2, which are the desired capabilities of commercial negative electrode materials. The lithiated and delithiated surface area capacities are compared in Figure 3-45. From these results it can be seen that the cycle life is maintained for approximately 58 cycles before deterioration occurs. The initial low capacities are attributed to the fast cycling rate (30mAh/g) causing lithium ion diffusion to take longer to penetrate the active

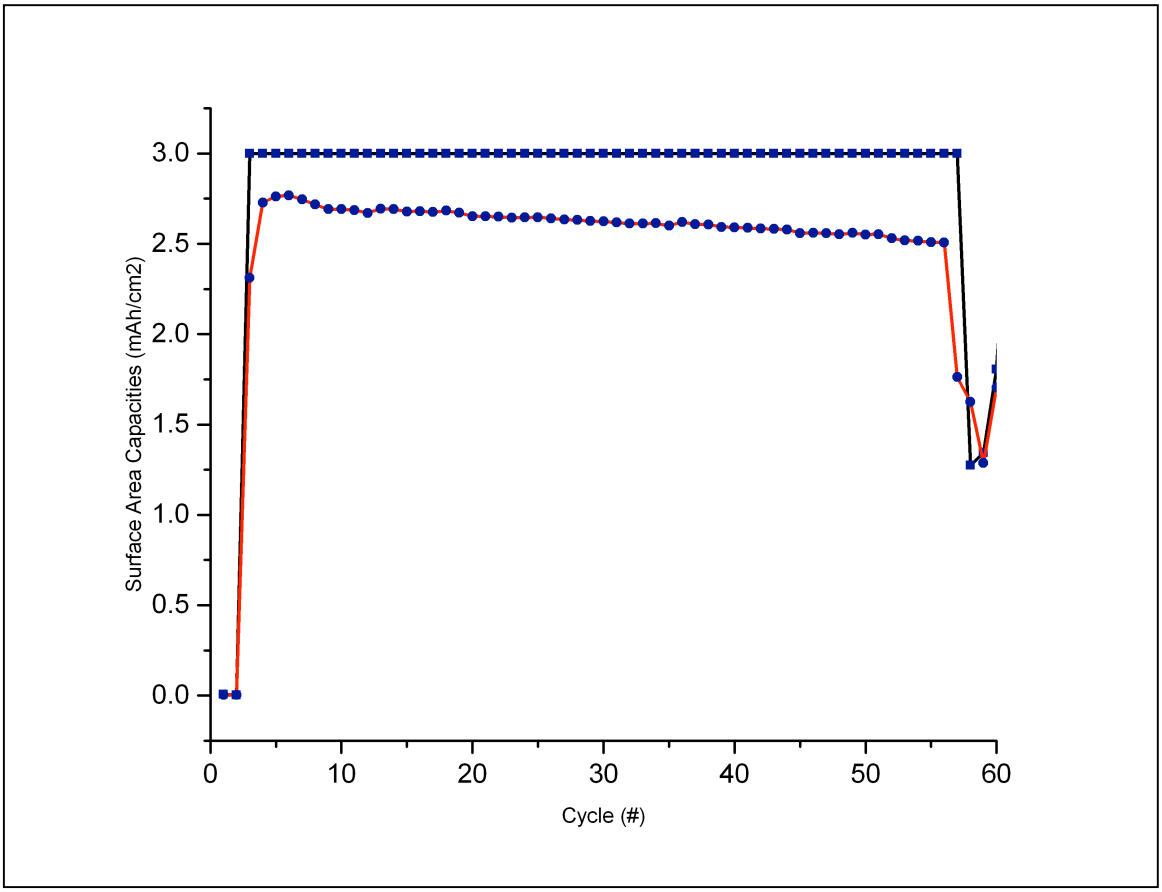

Figure 3-45 Comparison of the lithiated and delithiated surface area capacities (mAh/cm^2) to observe cycle retention with a fixed capacity cutoff. —: lithated capacities; —: delithiated capacities

material to form lithium alloys. The difference between the lithiated and delithiated capacities are due to incurred irreversible losses and/or loss of active material during cycling. It can be concluded that the early investigations of our triple stacked Cu-Sn films show promising cycling results, which hopefully can be further improved with more advancements in technology.

3.7.2 Cycling Rates

Cycling rates play a major role in the capacity retention of the active material due to the allowance of phase transformations and full lithiation over time. Three different cycling protocols were investigated for the triple stacked Cu-Sn 7.5μm film annealed 225°C 5h. The protocols are listed in Table 3-24. The general composition for the triple stacked Cu-Sn 7.5μm films heat treated at 225°C 5h was as follows: 3-6% Sn; 0% Cu_3Sn; 94-97% Cu_6Sn_5/CuSn. The volumetric and areal capacities are examined in Figure 3-46.

Table 3-24 Investigated cycling rates for optimal electrochemical properties of the triple stacked Cu-Sn films

Protocol	Cycling Range	Applied Current
1	0.01-2V	15mA/g (First 1.5 Cycles) 30mA/g (All Other Cycles)
2	0.01-2V	30mA/g (All Cycles)
3	0.01-2V	[A] 15mA/g (first 1.5Cycles) [B] 30mA/g (15 Cycles) [C]15mA/g (1Cycle) Repeat B & C For 1000 Cycles

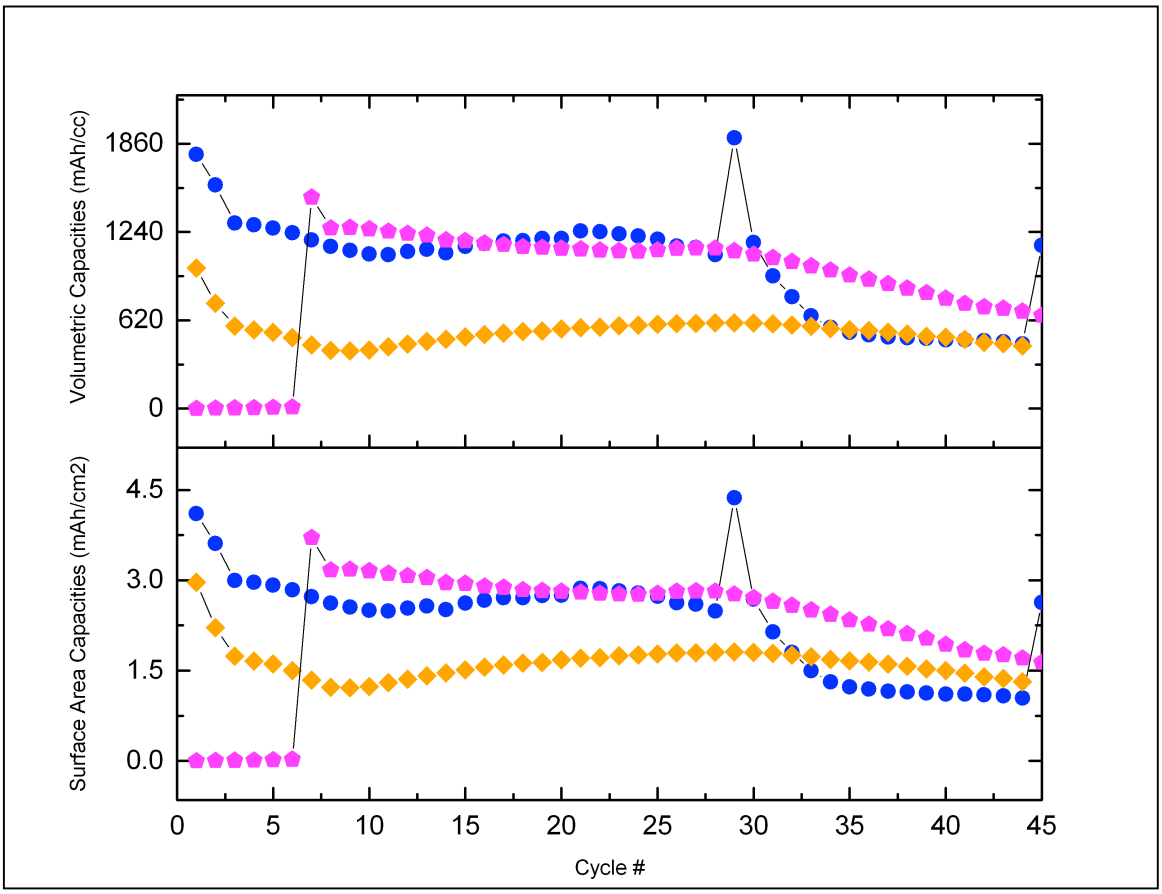

Figure 3-46 The electrochemical comparison of cycling speeds for triple stacked 7.5µm Cu-Sn films annealed 225°C 5h. ●: cycled protocol 3; ◆: cycled protocol 1; ⬟: cycled protocol 2.

This data confirms different obtained capacities with different cycling rates. Protocol 3 (intermittent slow rate 15mA/g in middle of cycling) introduces spikes

Table 3-25 Capacity retention for varying cycling rates for triple stacked Cu-Sn films.

Protocol	Capacity Retention 10-20th Cycle	Capacity Retention 10-30th Cycle	Capacity Retention 10-40th Cycles
1	136%	146%	122%
2	89%	86%	61%
3	110%	107%	44%

in the obtained capacity for the Cu-Sn films due to the slower rate allowing for more time for phase transformation to occur. However, this process also increases the obtained volume expansion stresses, which ultimately pulverize the active material and drop the capacity (cycles 30-45). The faster cycling rate (Protocol 2) initially has poor cycling capacities due to the minimal time allowed for phase transformations into the higher lithium alloys. Once the active material reaches a point where the lithium ions can diffuse more easily into the structure (structure relaxation with repetitive cycles), full phase transformations will occur to reach the high capacities inherent for lithium-tin alloys. This protocol begins to have decreased capacity retention at approximately 28 cycles. Protocol 1 commences cycling with a slower rate (15mA/g) and continues cycling at a higher rate (30mA/g). The obtained capacities for this protocol maintain a steady value of about 600mAh/cc and 1.5mAh/cm^2. Table 3-25 examines the capacity retention for these

protocols in greater detail. From this data it can be determined that the protocol with initial slow rate followed only by a faster cycling rate (Protocol 1) has the best retention probably due to the slower rate causing structure relaxation in the earlier stages of cycling (more active tin accessible for lithiation with deeper phase penetration of phase transformation in composite), however the remaining cycles at a faster rate minimize volume expansion stress damage with further lithiation.

3.7.3 Cu-Sn Films Incorporated Into Li-Ion Cells

The practicality of the electrodeposited triple stacked bilayer films were tested in full lithium ion cells assembled utilizing $LiCoO_2$ with approximately 3mAh/cm^2 versus the Cu-Sn 6.5μm (1.17:1) stacked films. Due to variability in the deposition process, several cells were produced and their compositional analysis observed. Figure 3-47 shows the electrochemical plots for the lithiated volumetric and surface areal capacities for the early cycles. The volumetric and areal capacities on the 5th cycle are 1380mAh/cc and 3.17mAh/cm^2 for cell D627 and 1246mAh/cc and 2.49mAh/cm^2 for cell D632. These cells maintained high cycling retention of 91% between cycles 3-13. Obviously, improvement for balanced Li-ion cells are needed, but further optimization needs to be performed with respect to matching ratios, electrode and electrolyte compositions. Overall our electrodeposited films and triple stacked thermal anneal process have thus far proved to produce freestanding negative electrodes for lithium ion cells unlike any other previously mentioned Cu-Sn research. The combined data shows that our technique has the

ability to fabricate lithium-alloying electrodes with both high volumetric and surface areal capacities. Although not perfected, this technique may be a viable approach

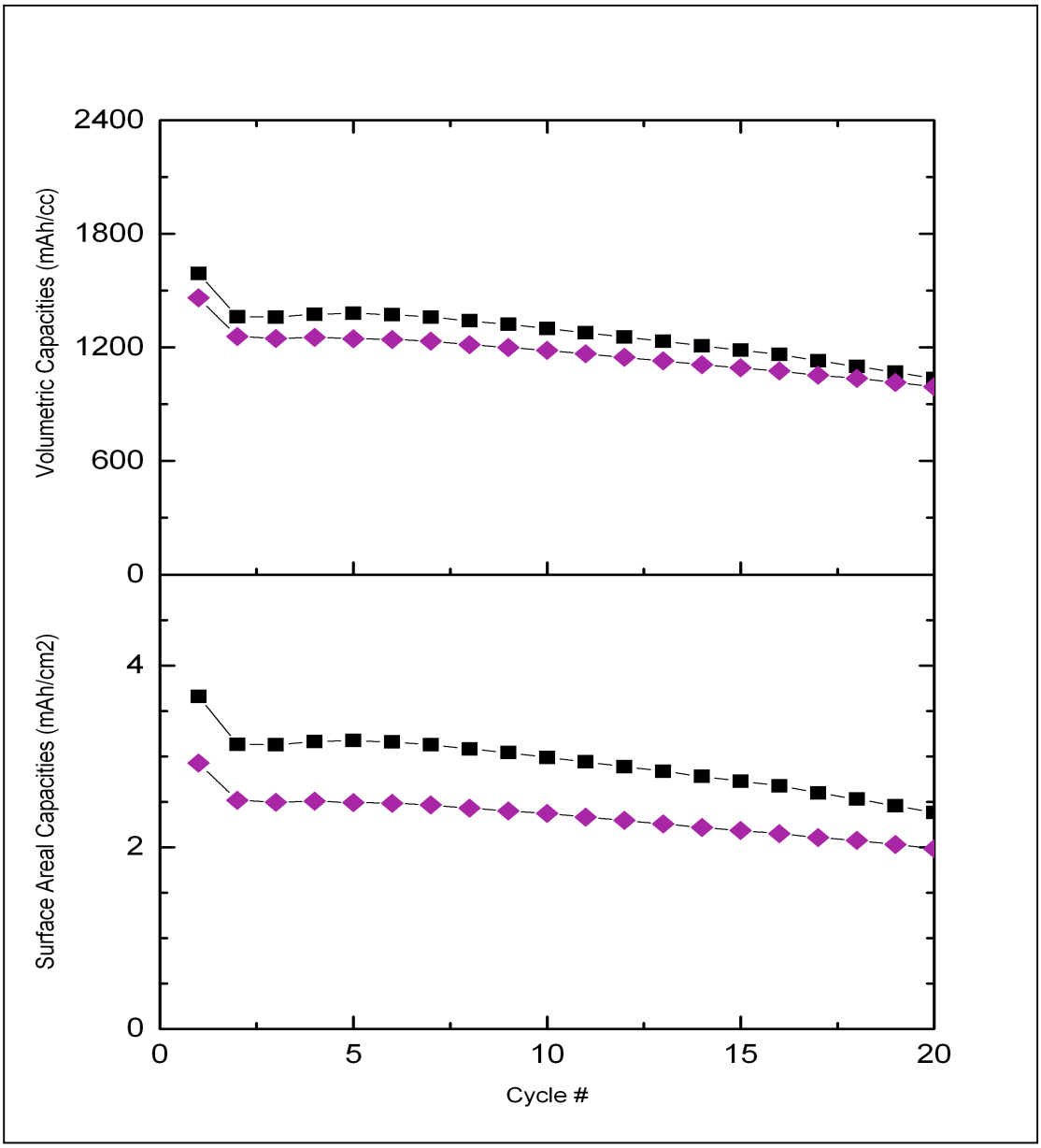

Figure 3-47 Electrochemical analysis for the first 20 cycles of the triple stacked 6.5µm (1.17:1 molarity) films in Li-ion cells. ■:D627; ◆:D632.

for rapid fabrication of various alloys for Li-ion batteries.

3.7.4 Conclusions

The triple stacked Cu-Sn films fabricated from the joint meniscus brush plating and stacked heat treatment process obtained superior electrochemical capabilities for cycling as negative electrode materials in lithium ion batteries. It was determined that observed capacities were the maximum achievable by cycling the Cu-Sn films with potentiostatic hold tests. The capacity retention (~60 cycles) for the Cu-Sn triple stacked films was also determined with application of a capacity cutoff of 3mAh/cm^2 (ideal cycling parameters). Initial investigations of these films as negative electrodes versus $LiCO_2$ were also successful in proving that the freestanding Cu-Sn films have potential in one day being competitive negative electrode materials with further research.

3.7.5 References

70 SIFCO Industries Incorporated, SIFCO Process Instruction Manual. 2010. 1-438.
71 M. Paunovic, M. Schlesinger, D.D. Snyder, Modern Electroplating. 5 (2010) 1-32.
72 W.J. Zhang. Journal of Power Sources. 196 (2011) 13-24.
73 C.T.J. Low, F.C. Walsh, Surface & Coatings Technology. 202 (2008) 1339-1349.
74 S.D. Beattie, J.R. Dahn, Journal of the Electrochemical Society. 150 (2003) A894-A898
75 L. Trahey, J.T. Vaughey, H.H. Kung, M.M. Thackeray, Journal of the Electrochemical Society. 156 (2009) A385-A389.
76 F-S. Ke, L. Huang, J-S. Cai, S-G. Sun, Electrochimica Acta. 52 (2007) 6741-6747.
77 R.A. Huggins, Journal of Power Sources. 81-82. (1999) 13-19.
78 S. Wang, W. Zhao, Y. Wang, X. Liu, L.Li, Electrochimica Acta. 109 (2013) 46-51.
79 L. Baggetto, J.F.M. Oudenhoven, T. van Dongen, J.H. Klootwijk, M. Mulder, R.A.H. Niessen, M.H.J.M. de Croon, P.H.L. Notten, Journal of Power Sources. 198 (2009) 402-410.

80 J. Liu, X. Li, M. Cai, R. Li, X. Sun, Electrochimica Acta. 93 (2013) 195-201.
81 H-Y. Wang, F-M. Wang, Journal of Power Sources. 233 (2013) 1-5.
82 M-L. Lee, C-Y. Su, Y-H. Lin, S-C. Liao, J-M. Chen, T-P. Perng, J-W. Yeh, H.C. Shih, Journal of Power Sources. (2012) 1-7
83 L. Chen, K. Wang, X. Xie, J. Xie, Journal of Power Sources. 174 (2007) 538-543.
84 H.A. Wilhelm, C. Marino, A. Darwiche, L. Monconduit, B. Lestriez, Electrochemistry Communications. 24 (2012) 89-92.

4 Future Work

This section will focus on the awareness to improvement ideas and research areas that will further enhance the designed copper-tin films discussed for use as negative electrodes. Aforementioned areas of interest are concepts that were not investigated due to time and resource restrictions for this project.

4.1 Hardware Alterations For the Meniscus Plating System

Improvements in the uniformity of the films could be reached by the manipulation of the counter electrode movement and geometry. As seen from the thickness mapping for the copper film or the variations of the XRD analysis for the triple stacked bilayer films, the consistency of the deposited layers is variable. One of the main reasons is the sinusoidal oscillation setup, which moves the counter electrode at the set speed for an average time, but as the movement changes direction, the speed slows down. This creates the excess thickness on the edges of the film. To avoid this occurrence, an instantaneous replacement motor would be necessary to drive the counter electrode at the desired speed. Upon reaching the points of directional change, the motor would instantly reverse direction, eliminating waste area from the deposited films and creating larger viable areas for electrochemical testing.

Another approach to fine-tuning the uniformity of the films would be the use of a larger counter electrode of rectangular geometry. This concept would eliminate

the full mechanical pulse produced by the movement of both our counter and working electrodes but might further improve the deposition homogeneity. Figure

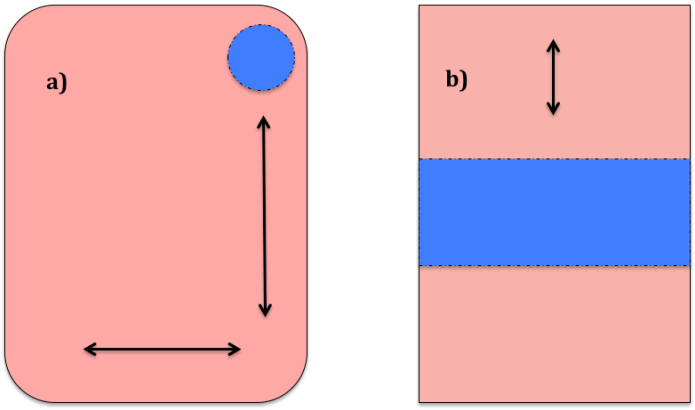

Figure 4-1 Counter electrode geometry proposition. a) The current geometry of the electrode creates areas not uniformly deposited due to mismatch in overlap. b) The rectangular configuration covers the entire width of the film, eliminating the one directional mismatch overlap.

4-1 shows examples of the current and proposed geometry changes. Similar to the previous concept, the enlarged counter electrode would magnify the viable deposited film and expand the possible sizes of producible negative electrodes.

4.2 Ternary System: Cu-Sn-Sb

As mentioned, in Chapter 1 of this thesis, active matrix materials are another option for expanding the capacity retention of lithium alloys. One system that was mentioned was the Sn-Sb composite, in which the active material alternates between reactive and supportive roles according to potential. Several investigations have seen improvements with this addition. The work of Simonin et al has found that this mixed system had improved capacity retention (20 cycles 475mAh/g)

compared to pure tin (4-5 cycles 400mAh/g) [85]. The work of Winter et al found that a mixed Sn/SnSb composite maintained charge recovery (95%) for over 100 cycles in comparison to pure tin, which had significant drop-off after 25 cycles [86]. Although these developments have somewhat increased retention capabilities, extreme volumetric stresses still effect both lithium alloying materials, therefore eventually leading to failure. The addition of the copper from our joint deposition and anneal heat treatment process could create a more complex system with added support and higher capacity.

Copper, tin, and antimony are known to form a complex ternary system, which may be beneficial for use as negative electrodes fabricated with our brush plating process. The binary phase diagrams are presented in Figure 4-2, which can be utilized for temperature analysis for the ternary formations [87]. These diagrams confirm multiple alloy formations at varying temperatures, which can be utilized when moving forward with investigations with our triple stacked system. More specifically, alloy formations for the Cu-Sb and Sb-Sn systems occur at our current optimal heat treatment temperature of 225°C. Antimony is also a great prospect for our system due to the availability of Tin-Antimony Code 5930 plating solution from SIFCO Applied Surface Concepts, the manufacturer of our Copper and Tin plating solutions.

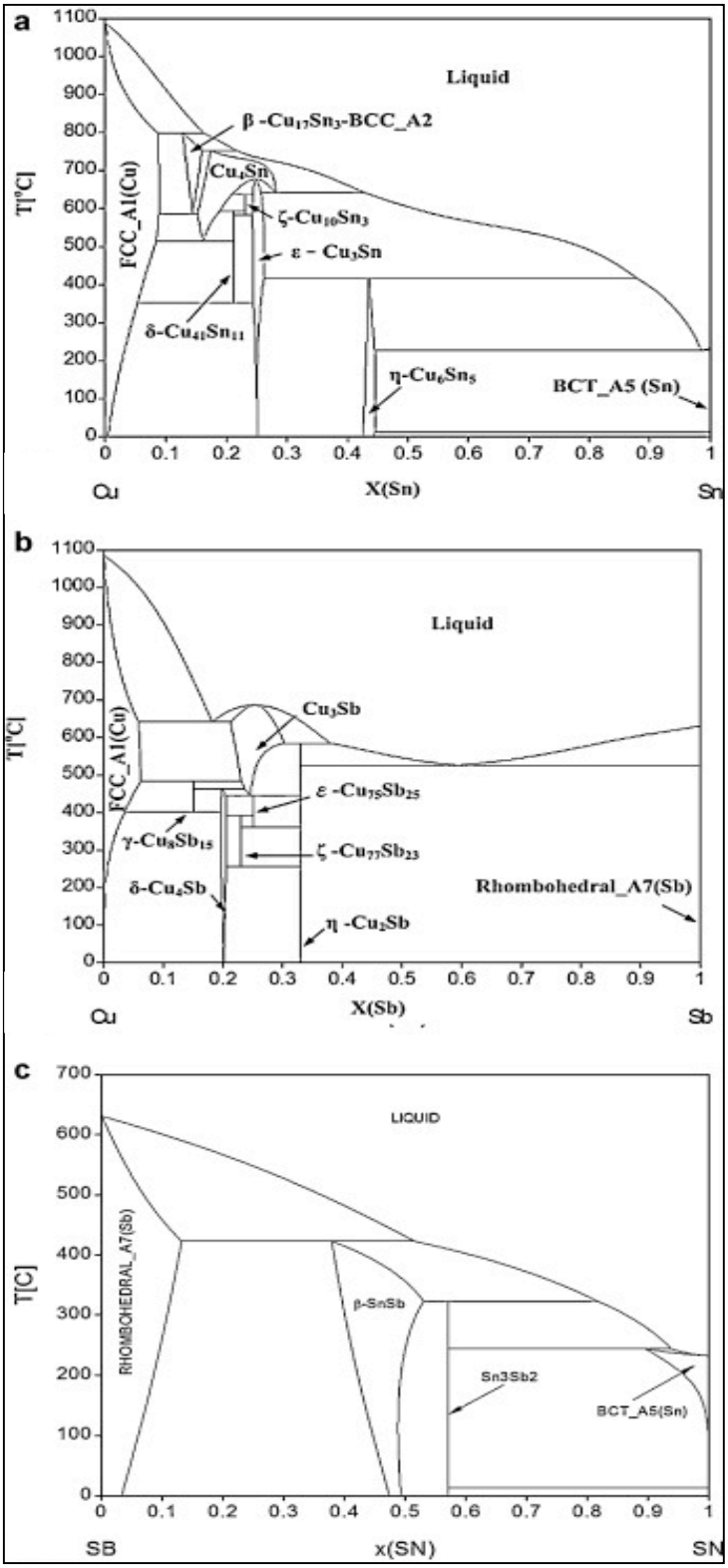

Figure 4-2 Binary phase diagrams for Cu-Sn (a) Cu-Sb (b) and Sb-Sn (c).

4.3 Additional Surface Coatings via ALD

Surface coatings have been utilized in past research to decrease the reactivity of the active material with the electrolyte leading to decreased large irreversible losses. In Chapter 3, alumina thin films (5nm and 15nm) were examined for the triple stacked Cu-Sn films. Unfortunately, in these investigations, the standard Cu-Sn films cycled better than films inclusive of these surface coatings. Poor cycling for these films could have occurred for a few reasons: 1) the alumina thin film thicknesses could have prohibited optimal cycling due to its insulating properties; 2) the alumina chemistry interferes negatively with the electrochemistry of the Cu-Sn causing increase in SEI or 3) the prolonged heating temperatures of the ALD process could have mechanically weakened the films due to increased brittleness. The exact reason for poor cycling has not been determined but could be of interest for future work.

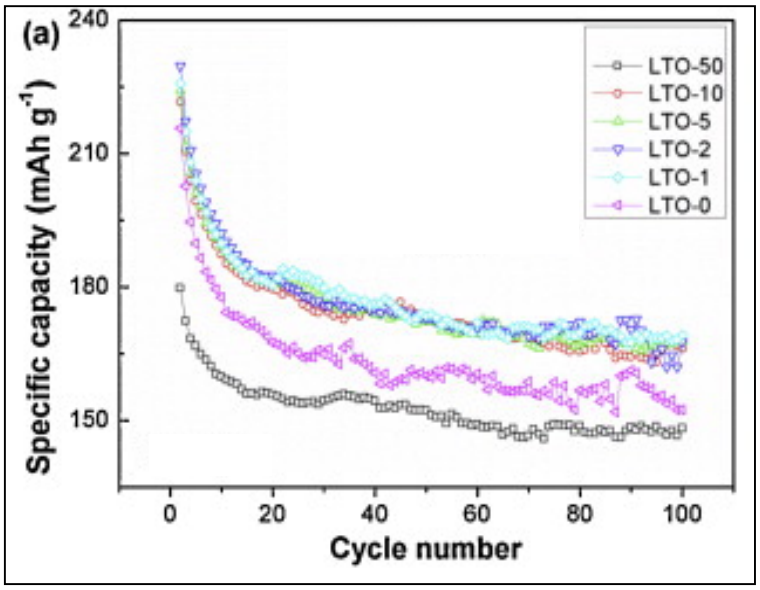

Figure 4-3 Cycling stability for ZrO_2 coated $Li_4Ti_5O_{12}$ electrodes. LTO-50 represents the thickest ZrO_2 coating and LTO-0 represents the thinnest coating.

Moving forward some other ALD thin film coatings that may be of interest for use to improve negative electrodes for lithium ion batteries include: ZrO_2, and TiO_2 [88,89]. ZrO_2 has been investigated using ALD with the negative electrode material $Li_4Ti_5O_{12}$ (LTO). In these studies, thickness ranges of 0.5-35nm thin film coatings were tested with the best electrochemical performances resulting from lower thicknesses (approximately 2-5nm). Figure 4-3 shows the resultant cycling stability for these surface coatings [89]. The best results were achieved from LTO-1 (170mAh/g), which was the second to lowest experimental thickness. TiO_2 thin films via ALD have also been examined for use with graphite electrodes. In these trials, thicknesses of 20-40nm coatings were investigated. The best results were seen from the 40nm film (400 ALD reaction cycles) as depicted in the comparative cycling results in Figure 4-4 [88]. In these results it can be seen that the thicker coating had superior cycling stability and capacity (225mAh/g) compared to the electrode with the thinner coating or standard. For both cases, ZrO_2 and TiO_2, enhanced cycling stability and capacities were attributed to the

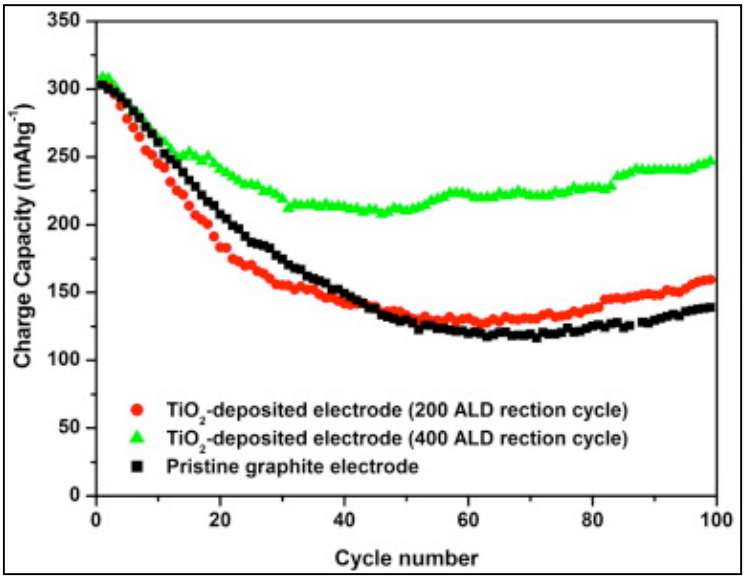

Figure 4-4 Electrochemical cycling stability comparison of TiO_2 ALD coatings with graphite electrodes. The 400 ALD reaction cycle film had a thickness of approximately 40nm. The 200 ALD reaction cycle film had a thickness about half that amount.

suppression of SEI formation. These are just two examples of the possible potentials in other surface thin films that could improve the cycling capabilities of our triple stacked Cu-Sn films.

4.4 References

85 L. Simonin, U. Lafont, E.M. Kelder, Journal of Power Sources. 180 (2008) 859-863.
86 M. Winter, J.O. Besenhard, Electrochimica Acta. 45 (1999) 31-50.
87 S-W. Chen, A-R. Zi, W. Gierlotka, C-F. Yang, C-H. Wang, S-K. Lin, C-M. Hsu, Materials Chemistry and Physics. 132 (2012) 703-715.
88 M-L. Lee, C-Y. Su, Y-H. Lin, S-C. Liao, J-M. Chen, T-P. Perng, J-W. Yeh, H.C. Shih, Journal of Power Sources. (2012) 1-7.
89 J.Liu, X. Li, M. Cai, R. Li, X. Sun, Electrochimica Atca. 93 (2013) 195-201.

5 Summary

The investigations of this thesis have outlined the manipulation of tin via the alloy composite, copper-tin, and the utilization of electrodeposition in a novel fabrication process to produce viable high capacity negative electrodes for lithium-ion batteries. The incorporation of copper as an inactive matrix material allows for the redistribution of the large volumetric expansion stresses inherent to lithium alloys that are detrimental to the capacity retention. The cycling of these intermetallic phases also dramatically lowers accumulated irreversible losses in comparison to the cycling of the pure tin phase.

In this research, we have successfully developed architecturally complex Cu-Sn films with a joint electrodeposition and heat treatment process. The technique of electrodeposition was implemented due to its control in morphological properties of its films, availability and ease of process, and commercial scalability. Our meniscus brush plating design is the first of its kind to create reproducible cohesive freestanding films. The innovative mechanical pulse from the simultaneous movement of the counter and working electrodes and continuous flow of plating solution to the meniscus working area has optimized electrodeposition conditions for improved current densities and limited particle size growth.

The goal of this project was to produce composite Cu-Sn negative electrodes with superior volumetric and areal capacities for use in lithium-ion batteries. This was achieved with maximum diffusivity of the deposited copper and tin layers to

form the copper-tin alloy, Cu_6Sn_5. Due to deposition issues for co-deposition and multi-layered deposition, the fabricated films were limited to single bilayer films of copper and tin with variable thicknesses. Analysis of all heat-treated single Cu-Sn bilayer films determined that the diffusion capabilities were not sufficient to accomplish the targeted capacities with good obtainable capacity retention. Therefore the single bilayer films were stacked in alternating layer order and pressed during heat treatment to maximize diffusion with the introduction of copper from both the top and bottom sides of the interior layers of a triple stacked bilayer film. This process created complex alloy compositions but with the domination of the Cu_6Sn_5 phase and elimination of the pure tin phase for film (Cu:Sn) molarities of (1.17:1) and (1:1.04). In addition, the triple stacked Cu-Sn bilayer films introduced a built-in copper current collector with the excess copper from the bottom bilayer film. From the commercial design perspective, this increased cell design efficiency, decreased fabrication cost with the elimination of additives and fillers from typical electrode tape design, and increased electrical and chemical stability with the intertwined electrode and current collector.

The presented electrochemical results for the triple stacked bilayer films obtained higher capacities (volumetric and areal) than all other previously published research in copper-tin electrodes. These early competitive capacity capabilities and retention offer promising advancements of lithium alloys as future high capacity negative electrodes for lithium ion batteries.

6 Publication Acknowledgement

Portions of Chapter 2 and Chapter 3 have been submitted for publication in September, 2014. The data from Chapter 3.3, 3.4, and 3.7.2 are directly derived from this publication submitted to *Journal of New Materials for Electrochemical Systems* as "The Fabrication of Freestanding Heterogeneous Copper-Tin Films with Meniscus Brush Plating Electrodeposition." The authors include K. Scott, A. Halajko, and G.G. Amatucci.